



University
of Glasgow

Restuccia, Sara (2020) *Entanglement enhanced communication and sensing*. PhD thesis.

<http://theses.gla.ac.uk/79023/>

Copyright and moral rights for this work are retained by the author

A copy can be downloaded for personal non-commercial research or study, without prior permission or charge

This work cannot be reproduced or quoted extensively from without first obtaining permission in writing from the author

The content must not be changed in any way or sold commercially in any format or medium without the formal permission of the author

When referring to this work, full bibliographic details including the author, title, awarding institution and date of the thesis must be given

Enlighten: Theses

<https://theses.gla.ac.uk/>
research-enlighten@glasgow.ac.uk

Entanglement Enhanced Communication and Sensing

Sara Restuccia

A thesis submitted in fulfilment of the requirements for the degree of
Doctor of Philosophy

School of Physics and Astronomy
College of Science and Engineering
University of Glasgow

February 2020

Abstract

Entanglement has been an extremely active field of research both from a theoretical and an experimental point of view. As the understanding of the phenomena grows, so does the interest in using it to advance different technological fields: communication, computing and sensing being just some examples. It is now well known that entangled photon pairs can be generated through a process known as spontaneous parametric down-conversion (SPDC). In this thesis I therefore integrate the SPDC generated photons in a variety of experiments each exploiting a different characteristic of this quantum effect. In particular, both chapter 3 and chapter 4 utilise the spatial degree of freedom of SPDC generated entangled photons to enhance the quantity of information that can be transmitted in quantum communication systems. In particular, in chapter 3 the information capacity of two of the best known spatial modal sets is analysed in the context of real life finite-aperture communication systems, while chapter 4 proposed a new approach for imparting information onto photons. On the other hand, both chapters 5, and 6 rely on the ability of SPDC to generate completely indistinguishable photon pairs, which, when made to interfere, bunch together in what is known as N00N state. In particular, chapter 5 demonstrates that the recently discovered “Coherent Perfect Absorption” process (CPA) can be used to coherently control and absorb two-photon N00N states and therefore can be employed in the generation of quantum gates, while in chapter 6, the quantum interference process that produces the N00N states is used to test the role of relativity in quantum mechanics through the construction of a “quantum gyroscope”.

Contents

Abstract	i
Contents	ii
List of Figures	iv
List of Tables	vi
Acknowledgements	vii
Declaration of Authorship	ix
Publications	x
1 Prelude	1
1.1 The quantum nature of light	1
1.2 Walkthrough	3
2 Background	5
2.1 Introduction	5
2.1.1 Generating Photons: Spontaneous Parametric Down-Conversion (SPDC)	5
2.1.2 Experimental apparatus	11
2.1.3 Klyshko advanced wave model	13
3 Encoding information in Aperture Limited Systems	16
3.1 Introduction to Quantum Communication	16
3.1.1 Contributions	19
3.2 Encoding Information With Spatial Modal Sets	19
3.3 LG vs HG in a Finite-Aperture System	21
3.4 Conclusion	35
4 OAM in a Communication System	36
4.1 Introduction	36
4.1.1 Contributions	38
4.2 Generation of Continuous OAM beams	38

4.3	Experimental Set-Up and Data Analysis	41
4.4	Conclusion	50
5	Coherent Absorption of N00N States	51
5.1	Introduction	51
5.1.1	Contributions	55
5.2	The Hong-Ou-Mandel experiment	56
5.3	Graphene as a lossy beam splitter	59
5.4	Coherent Absorption of N00N states	65
5.5	Data Collection	68
5.6	Analysis of the results	71
5.7	Conclusions	74
6	Quantum Gyroscope	75
6.1	Introduction	75
6.1.1	Contributions	79
6.2	Sagnac effect	79
6.3	HOM as a Sagnac interferometer	83
6.4	Classical counterpart to the Quantum Gyroscope	89
6.5	Conclusion	91
7	Conclusions and Future Work	93

List of Figures

2.1	Spontaneous parametric down conversion.	8
2.2	Phase-matching scenarios.	9
2.3	Klyshko picture.	14
3.1	Comparison between a classical and a quantum system.	24
3.2	Experimental set-up for the experiment: “Encoding information in Aperture Limited Systems”	25
3.3	An example of the SLM phase pattern.	25
3.4	Results from the simulation of the experiment [18].	29
3.5	Experimental results of the modal base [18].	30
3.6	Example of the phase fronts for LG modes $l = -1, p = 0$ and $l = -1, p = 1$ at different waist ratios.	31
3.7	Simulated correlation matrix for the HG modal set with a non optimal aperture ratio.	33
3.8	Example of the phase fronts for HG modes $m = 1, n = 0$ and $m = 2, n = 1$ at different waist ratios.	34
3.9	Bpp for different N calculated using the modelling system.	34
4.1	Experimental set-up for the experiment: “OAM in a Communication System” [19]	42
4.2	Vortex beam generator	43
4.3	Comparison between classical and quantum hologram generation	44
4.4	Spiral spectrum calculated for different aperture sizes.	45
4.5	Quantum spiral spectrum of the spiniform phase [19].	46
4.6	Simulated quantum spiral spectrum of the spiniform phase.	47
4.7	Quantum correlation matrix for the proposed vortex generator [19].	48
5.1	CNOT Gate	53
5.2	HOM interferometer	56
5.3	Outputs of a HOM interferometer	57
5.4	Schematic representations of beam splitters [108]	60
5.5	Schematic representation of a thin layer CPA	61
5.6	HOM Dips at different bandwidth.	66
5.7	Experimental set-up for the experiment Coherent Absorption of N00N states [15].	67
5.8	Experimental data from a lossy beamsplitter	69
5.9	Fourier transfer of RAW data.	70

5.10	Lossless 50:50 beamsplitter	71
5.11	Total measured two photon states	73
6.1	Dynamic range and sensitivity of the different types of gyroscope currently presented in the market (original image can be found in [110]).	76
6.2	Classical design of a fibre Sagnac interferometer	80
6.3	Principle of the Sagnac effect	81
6.4	3D representation of the quantum gyroscope	83
6.5	Schematic representation of the HOM interferometer on the rotating system [122]	84
6.6	Results of the quantum experiment.	87
6.7	Set-up and results of the classical experiment	89

List of Tables

3.1	Intensity profile for LG and HG modes with mode order $N \leq 3$	28
5.1	Quantum states for a lossless beam splitter	62
5.2	Quantum states for a lossy beam splitter	63

Acknowledgements

I would firstly like to thank my supervisor Miles for his expertise, enthusiasm and passion for this research, and for giving me the opportunity to participate in such an exciting research field, meet new people and be part of this amazing research group. This thesis would not have been possible without his guidance and support throughout my PhD.

I would also like to extend a thank you to Graham, for his invaluable support and guidance, as well as our daily lunch/coffee breaks. His lab expertise and advice were essential and I would not have been able to achieve as much as I did in my years in the Optics group without his help and friendship.

I would like to thank Sonja, for introducing me to the Optics group and for always being available for advice. I would also like to thank Jacqui Romero for showing me the ropes at the beginning of my PhD and for introducing me to this field of research, as well as giving me invaluable advice. Not only was she a great teacher, she was also a great example for me. I would also like to thank Johannes for being my second supervisor at the beginning and for being great company during our much needed coffee breaks.

I would like to thank the current and previous members of the optics group for the many interesting lunch time conversations and laughs. Each and every one of you contributed in making the group feel like a big family and a place I enjoyed going to every day. In these years in Glasgow I have made many friends, Valentina, Daniela, Gianluca, Steve O., Rebecca, Laura, Thom Clark, Gergely being some but not all! They were there when I needed help and I am glad for their friendship.

I would like to also thank Prof Robert Boyd for giving me the opportunity to visit his research group in Ottawa in 2017 and the University of Glasgow College of Science and Engineering for the funds that supported this experience. The visit to Ottawa gave me the opportunity to work with wonderful people and widely expand my Physics knowledge.

I would like to thank both my families: my parents, my grandfather, my grandmother, and my brothers Francesco, Davide and Domenico, for being so encouraging and supporting me throughout this journey. I know that, if I ever needed help or simply a good holiday all I had to do is pick-up the phone and there would always be someone on the other side ready to help.

During my time in Glasgow I have also become a member of a new family: the Saundersons. I would therefore like to thank my husband's family for welcoming me into their home, and especially for listening to my many "cool" experiment descriptions.

Most importantly, I would like to thank my husband Nick. This thesis would not have existed if not for his help and love during these years. During my PhD was not always the best for keeping "normal" working hours, but he has always been there with encouragement and dinner.

Finally, I would like to thank the European Union's Seventh Framework Programme (TWISTS), for funding my PhD.

Declaration of Authorship

I hereby declare that this thesis is the result of my own work, except where explicit reference is made to the work of others, and has not been presented in any previous application for a degree at this or any other institution.

Sara Restuccia

Publications

What follows is a list of papers published during my PhD.

1. T. Roger, S. Restuccia, A. Lyons, D. Giovannini, J. Romero, J. Jeffers, M. Padgett and D. Faccio, “Coherent absorption of NOON states”. *Physical Review Letters* **117**, 023601, 2016
2. S. Restuccia, D. Giovannini, G. Gibson and M. Padgett, “Comparing the information capacity of Laguerre-Gaussian and Hermite-Gaussian modal sets in a finite-aperture system”. *Optics Express* **24**, 27127-27136, 2016
3. K. Huang*, H. Liu*, S. Restuccia*, M. Q. Mehmood, S. Mei, D. Giovannini, A. Danner, M. J. Padgett, J. Teng and C. Qiu, “Spiniform phase-encoded metagratings entangling arbitrary rational-order orbital angular momentum”. *Light: Science & Applications* **7**, 17156, 2018
4. S. Restuccia*, M. Toroš*, G. M. Gibson, H. Ulbricht, D. Faccio and M. J. Padgett, “Photon bunching in a rotating reference frame”, *Physical Review Letters* **123**, 110401, 2019

*These authors contributed equally.

Abbreviations

BBO	β - B arium B orate
BPP	B its P er P hoton
BS	B eam S plitter
CPA	C oherent P erfect A bsorption
CU	C ontrolled U nitary gate
CW	C ontinuous W ave
DFG	D ifferent- F requency G eneration
EPR	E instein P odolsky R osen
FOG	F ibre O ptical G yroscopic
HG	H ermite G aussian
HOM	H ong- O u- M andel
KEP	K nife- E dge P rism
LG	L aguerre G aussian
MZI	M ach- Z ehnder I nterferometer
OAM	O rbital A ngular M omentum
QC	Q uantum C ontrast
QE	Q uantum E fficiency
QKD	Q uantum K ey D istribution
RLG	R ing L aser G yroscopic
SAM	S pin A ngular M omentum
SFG	S um- F requency G eneration

SHG	S econd- H armonic G eneration
SLM	S patial L ight M odulator
SPAD	S ingle P hoton A valanche D etector
SPDC	S pontaneous P arametric D own C onversion

To the person who gave me my love of Physics,

Nonno Franco

Chapter 1

Prelude

1.1 The quantum nature of light

Entanglement has been an extremely active field of research attracting great interest both for its theoretical implications and for the many applications that it can produce. This physical phenomena is unique to quantum mechanics as it does not have any classical equivalent. In particular, entanglement is a property of correlation between two or more quantum systems i.e. two or more particles are said to be entangled if the state of one of the particles cannot be described without also describing the state of the other particles [1].

Entanglement was first described by Albert Einstein together with B. Podolsky and N. Rosen (EPR) in their seminal 1935 paper, which questioned the completeness of the quantum-mechanical model due to the existence of these non-factorizable two-particle states [2]. In particular, they proposed an EPR state composed of two subsystems that had been made to interact before being spatially separated, while still individually maintaining correlated properties (such as position and momentum). They sustained that quantum mechanics was a locally causal theory and in order to

allow for correlations between the two systems, and recover the prediction of standard quantum mechanics, an introduction of hidden variables was necessary. Shortly after the publication of the EPR paper, Erwin Schrödinger addressed the paradoxical nature of the EPR experiment with a three-part letter in which he introduced, for the first time, the term entanglement to describe the non-local correlations between the two states [3]. In his letter he suggested that what should be questioned is not the completeness of quantum mechanics but the assumption that quantum mechanics is a locally causal theory and described entanglement as a characteristic trait of quantum mechanics. It wasn't until the publication of John Bell's paper in 1964, that the validity of the EPR arguments, was formally challenged. In this paper, Bell demonstrated that the principle of locality, an underlying assumption of the EPR argument, was mathematically inconsistent with the interpretation of quantum theory made in the EPR paper [4]. Specifically, he demonstrated the existence of an upper bound for systems exhibiting locality, and showed that quantum theory predicts violations of this limit for certain non-local systems, which include quantum states, thus ruling out the possibility of hidden variable theories. Bell's theorem was then extended by Clauser, Horne, Shimony, and Holt to cover actual systems and therefore proposing an inequality to test for all local hidden-variable theories, making it experimentally possible to prove the validity or not of quantum mechanics and therefore the necessity of a hidden variable theory [5].

In recent years, a number of novel experiments have been carried out using parametric down converted photons for the realisation of ideas concerning quantum entanglement ([6–15]). In particular, they have focused on demonstrating the uniqueness of this effect to the quantum mechanics, and therefore it's non replicability by means of a classical formalism. These experiments attracted great interest seeing that they play an important role in the creation of future quantum applications as well as the development of new areas of physics, for example quantum information theory [1]. In

particular, within the UK, new quantum technology hubs have been formed with the intention of creating new technologies, in the fields of quantum computing devices, quantum enhanced imaging, quantum secure communications, quantum acceleration and navigation devices, quantum gravity sensing devices, and quantum timing devices [16]. With the current improvement of our knowledge in the field of quantum optics coupled with the growing sophistication and sensitivity of optical equipment, testing theoretical ideas in connection with the foundations of quantum mechanics is now becoming a reality; some example being the recent demonstration that the invariance of the speed of light only applies to plane waves and the recent experiment testing the effect of a uniform acceleration on photon entanglement [12, 17]. However, quantum optics is still a very open field of research and the scope of my PhD is to conduct new experiments in this field, in the hope of gaining a better understanding of entangled photons and therefore make it more accessible for future applications.

1.2 Walkthrough

While this chapter stands as a general introduction to the thesis, and quantum entanglement, in the following sections I will give a brief introduction to the topics discussed in the remaining chapters.

Chapter two: As the generation of entangled photons is central to all the experiments I conducted during my PhD, in this chapter a general background to the spontaneous parametric down conversion process is given.

Chapter three: In this chapter the work of my published paper “Comparing the information capacity of Laguerre-Gaussian and Hermite-Gaussian modal sets in a finite-aperture system” is discussed. This work was performed both numerically and experimentally by me and is now published in *Optics Express* [18].

Chapter four: In this chapter the work of my published paper “Spiniform phase-encoded metagratings entangling arbitrary rational-order orbital angular momentum” is discussed. The work in this chapter was carried out as part of a collaboration with the *National University of Singapore* of which I was solely responsible for designing and implementing the experiment for a quantum communication system. This work is now published in *Light: Science & Applications* in a research paper of which I am one of the joint first authors [19].

Chapter five: In this chapter the work of my published paper ‘Coherent absorption of NOON states’ is discussed. This work was carried out as part of a collaborative effort between members of multiple universities (i.e. *University of Glasgow, Heriot-Watt University, University of Strathclyde*). As part of the collaboration, I was responsible for the design and setting up of the experiment, in addition to running the experiment and collecting the data. The output of this work is now published in *Physical Review Letters* of which I am second author [15].

Chapter six: In this chapter the work currently submitted in the paper “Photon bunching in a rotating reference frame” is discussed. This work was also carried out as part of a collaborative effort between my university and the *University of Southampton*. This project was proposed by my supervisor, and I was responsible for the experimental design, the running of the experiment, the collection of data and the analysis of the results. The theoretical background for the paper was provided by our collaborators in Southampton. This work is currently under review in *Physical Review Letters*.

Chapter seven: In this chapter a summary is given of each of the projects discussed in the thesis along with a discussion of future work and applications.

Chapter 2

Background

2.1 Introduction

Before proceeding to the main chapters of this thesis, I will first introduce relevant background theory for the generation of the entangled photons which will be used in all the subsequent chapters.

2.1.1 Generating Photons: Spontaneous Parametric Down-Conversion (SPDC)

As previously stated, entangled systems are completely described in quantum mechanics and exhibit non-locality, therefore in order to be able to run a quantum experiment it is necessary that the experiment violates Bell's inequality. Consequently it is necessary that the photons used in the experiment be entangled and that during the experiment it must be possible to choose to measure quantities among at least two non-commuting observables. Nowadays, the most common method of generating entangled photon pairs is by the use of a nonlinear crystal through a process called

spontaneous parametric-down-conversion (SPDC). This is a quantum-mechanical decay process, in which a pump photon, entering an optically nonlinear medium, decays into two lower-energy photons, which are commonly known as the signal and idler photons (fig. 2.1) [20].

The parametric process at the base of SPDC is not a new concept as it was initially developed as a low noise amplifier for radio waves and microwaves and was first demonstrated in the optical wave-range in 1965 by Giordmaine and Miller [21]. In particular, in the optical range there are two basic processes that can lead to parametric gain: three-wave mixing (which occurs when a second order non-linear process takes place), and four-wave mixing (which occurs through a third order non-linear process) [20]. As the photon pairs in this thesis are generated through SPDC, a second order non-linear process, only this case will be discussed.

Second Order Nonlinear Process

A second order nonlinear process occurs in a medium in which the second-order susceptibility tensor $\chi^{(2)}$ is nonzero hence the nonlinear polarisation induced inside the crystal by an applied electric field can be written as: $\mathbf{P}(t) = \epsilon_0 \chi^{(2)} \mathbf{E}^2(t)$ where \mathbf{E} is the electric field at time, t , and ϵ_0 is the permittivity of free space [22]. This process is the lowest order nonlinear process that can occur in a nonlinear medium and is restricted to crystals that are non-centrosymmetric (a more detailed explanation can be found in Boyd's book "*Nonlinear Optics*" [22]). When the electric field incident upon a crystal with a substantial $\chi^{(2)}$ is composed of two distinct frequencies, the frequency components of the optical field mix to produce a third component in what is known as three-wave mixing. In particular, the two frequency components can induce an oscillation in the polarisation that is the sum of the two frequencies in a nonlinear process called sum-frequency generation (SFG) or the two frequency

components can induce an oscillation that is the difference in energy between the two, in what is known as different-frequency generation (DFG). It is important to note that, the specific nonlinear process SFG in which the two input field have the same frequency has its own name: Second Harmonic Generation (SHG). This process, often also known as frequency doubling, has been found to be very useful in modern optical laboratories as it takes two input fields and outputs a new field with twice the energy of the initial ones. This can therefore be used to convert fixed wavelength lasers to different spectral regions. More importantly for the scope of this thesis, SHG is the time reversal equivalent of the Parametric Down Conversion Process used in our experiment to generate the entangled photon pair. As for SHG this nonlinear process is also a three wave process with the major difference being that, instead of having two input fields produce a single output field, a single input field produces a pair of correlated output fields. As previously stated, in the Parametric Down Conversion Process photons from a high energy pump field propagating through a crystal possessing a $\chi^{(2)}$ nonlinearity will decay into a pair of lower energy photons (fig. 2.1). It is important to note that in a low-gain regime signal and idler fields can still be generated without an input in what is known as Spontaneous Parametric Down Conversion (SPDC) [20]. In this case the process is stimulated by fluctuations in the quantum vacuum hence any field that is coupled in the process may radiate. It therefore follows that the photon pairs generated through SPDC are time independent of each other and generated with any combinations of energy and momentum allowed by the restrictions imposed by the nonlinear crystal and pump field employed [23].

Phase Matching

Being a parametric process, SPDC leaves the quantum state of the medium unchanged and therefore the angular frequencies of the pump (w_p), signal (w_s) and

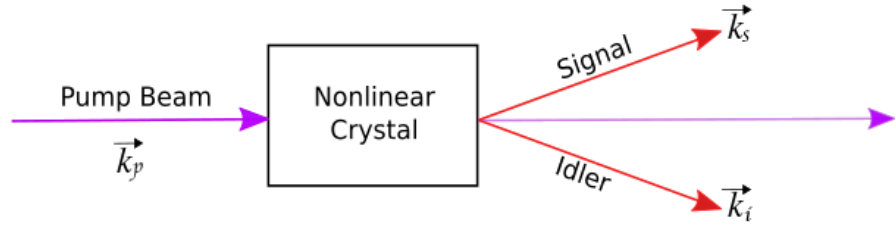


FIGURE 2.1: Spontaneous parametric down conversion (SPDC). A pump photon entering a non linear crystal probabilistically induces the production of a pair of phase-matched signal and idler photons. The case illustrated corresponds to the sub-case of non-collinear SPDC process i.e. the signal and idler photons are emitted at an angle compared to the direction of the pump.

idler (w_i) photons follow the energy conservation.

$$w_p = w_s + w_i \quad (2.1)$$

In addition, the efficiency of the emission is greatest when there is conservation of linear momentum and therefore the sum of the wave vectors of the signal (\vec{k}_s) and the idler (\vec{k}_i) equals that of the pump (\vec{k}_p):

$$\vec{k}_p = \vec{k}_s + \vec{k}_i \quad (2.2)$$

If both relations 2.1 and 2.2 are met, the condition is known as phase-matching and the pairs of photons created are both phase-matched in the frequency domain and have correlated polarisations. It is important to note that in order for the phase matching conditions to be met the generated fields must be in phase with the pump throughout the length of the crystal. This becomes a problem in the non-degenerate SPDC process where different optical frequencies are present as different optical frequencies propagate through a transparent medium with different phase velocities. The most common experimental way of mitigating this chromatic dispersion is through the use of a birefringent crystal as birefringent mediums have a refractive indices that varies with the direction of polarisation of the light [22]. It therefore

follows that when using a birefringent crystal, one must pay attention on the orientation of the crystal and the polarisation of the optical fields as only a certain number of geometries are allowed. In particular, phase matching in a birefringent crystal can take place for two possible phase matching conditions: if the signal and idler photons have the same polarisation which is orthogonal to the pump polarisation or if the signal and idler have perpendicular polarisation to each other. These two cases are known as type-I, and type-II down-conversion respectively. It must be pointed out that conservation of momentum can also be achieved through a process called quasi-phase matching where a crystal source with periodically poled domains such as a PPTKP crystal is used. In this case phase matching does not occur, but inside each domain a certain amount of mismatch takes place which then gets corrected in the adjoining domain which is set up so as to have a mismatch of equal value but of opposite sign. As this case does not need to use the birefringence property to maintain the phase-matching conditions it allows a third alignment geometry, also known as type-0 SPDC, where the signal, idler and pump photons have the same polarisation. In the experiments described in this thesis only type-I SPDC is used to generate the down-converted photons.

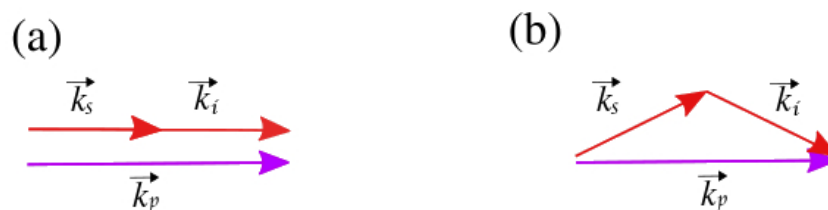


FIGURE 2.2: Illustrated are some different phase-matching scenarios. In particular (a) illustrated the perfect collinear case in which the two photons are emitted in the same direction as the pump. On the other hand (b) demonstrates perfect non-collinear SPDC where the two photons are emitted with opposite transverse momentum.

Finally as previously pointed out, when using a birefringent crystal to achieve phase matching, one must not only take in consideration the polarisation of the fields but also the orientation of the crystal. In particular, in the case of remaining mismatch

between the pump and the generated fields careful tuning of the angle of the crystal can be used to alter the path of propagation of the pump, signal and idler photons so as to compensate the phase mismatch and therefore satisfy equation 2.2. It therefore follows that the SPDC process can either be collinear (fig. 2.2a) or noncollinear (fig. 2.2b). In the first case the signal and idler photons are emitted in the same direction, parallel to the direction of the pump, while in the second case the signal and idler photons are emitted at an angle relative to the direction of the pump (fig. 2.2b). It is important to note that in the noncollinear case in order for equation 2.2 to be valid, the transverse momenta of the signal and idler photons must be opposite in direction. In an experimental set-up, the case of type-I collinear SPDC manifests itself as a bright on-axis spot in the far-field of the crystal. On the other hand, type-I noncollinear SPDC appears in the far-field as a bright annulus symmetric about the pump propagation axis where the generated signal and idler photon pairs appear in diametrically opposite positions and the width of the ring is determined by the width of the allowed frequencies i.e. it is directly correlated to the bandwidth of the generated photons. It is important to point out that the bandwidth of the photons is directly linked to the length of the crystal i.e. the shorter the crystal the wider the range of frequencies that can be generated while still maintaining the phase matching conditions. Similarly the spatial degree of freedom of the correlated photons is also linked to the length of the crystal. In particular, the longer the crystal the bigger the degree noncollinearity needed for the phase matching conditions to be met i.e. the correlated photons are generated over a narrow range of opening angles limiting the ambiguity in the direction of traveling of any one photon. A full analysis of the correlation between spatial bandwidth and length of a BBO type-I crystal can be found in the Miatto et al. paper [24].

2.1.2 Experimental apparatus

In the following chapters four distinct experiments will be presented, however, while the quantum effects tested in each experiment are different, all experiments share some common experimental methods and apparatus. In particular, all experiments are composed of a source of entangled photons and, at the output of the different experimental setups, a method of collecting the signal and idler photons in order to measure their correlation.

For all experiments discussed in this thesis the same SPDC source is used to generate entangled photons. In particular, the signal and idler source is composed of a 3mm type-I β -Barium Borate (BBO) crystal pumped either by a 355nm CW (chapter 3, 4, 6) or a quasi-CW (chapter 5) laser source. The use of a BBO crystal for SPDC is quite common as it not only has a high second order nonlinearity component, but it is also birefringent hence making it suitable for both type-I and type-II phase matching [25]. In particular, a 3mm type-I BBO crystal has been a common choice of crystal for quantum entanglement experiments carried out in my research group thus the choice of this crystal was made in order to have continuity with previous work performed in the research group [24, 26–28]. The SPDC source component of the setups is completed by the presence of a longpass filter. This filter is employed after the crystal to block the residual pump beam and only enable the entangled photons to be present in the experimental system. In particular, the longpass filter chosen for our experimental set-ups has a 93% transmission rate for all wavelengths between 504.7–900nm while reflecting all wavelengths under 504.7nm.

As well as a source of entangled photons, all our experimental systems necessitate of a way of collecting the outputted signal and idler photons and measuring their correlation. Hence, in all our experiments, the signal and idler photons are collected by fibres connected to silicon single photon avalanche photodiodes (SPADs) which

transmit their output to a coincidence circuit. In particular the SPADs used in all the experiments presented in this thesis are designed to have maximum efficiency for photons with wavelength of 700nm. Similarly, in all experiments, with the exception of the experiment described in chapter 5, the same coincidence circuit is used composed of an event timing module with a temporal resolution of about 3ps. When connecting the two detectors to the input channels of the event timing module a histogram of the relative temporal difference between the arrival of the two photons can be calculated. It is important to note that for non-classical states, i.e. the ones generated through SPDC, the events are independent of each other hence they will follow a Poissonian distribution [29]. It therefore follows that in the case of a CW laser pumping our 3-mm type-I BBO crystal, the coincidence events will manifest as a Poissonian peak over a certain number of time bins. It should be mentioned that the sole presence of single photons on each output can give rise to coincidence events that are not due to the pair of photons generated through SPDC but simply to chance. These are known as “accidentals” (Acc) and their probability can be estimated as

$$Acc = S \times I \times \Delta t \quad (2.3)$$

where S and I are the photons measured by the detectors on the signal and idler output of the system and Δt is the resolving coincidence window of the machinery (i.e. it is directly related to the number of time bins used to generate the histogram) [30, 31]. The strength of the correlation in our system can therefore be calculated by dividing the total number of coincidence events measured by the accidentals. This is known as quantum contrast (QC) and can be written as:

$$QC = \frac{MC}{Acc} = \frac{MC}{S \times I \times \Delta t}. \quad (2.4)$$

where MC is the measured coincidence. It is important to note that the use of coincidence to accidental ratio is quite useful as it is an useful way of characterising the efficiency of the experimental quantum system. A similar method to quantify the photon-pair signal to noise ratio is through what is known as coincidence to accidental-coincidence ratio (CAR) [32, 33]. In this case the purity of the state is quantified by:

$$CAR = \frac{MC - Acc}{Acc}. \quad (2.5)$$

It can easily be noted that limiting the time bins used to calculate the coincidence rates to only the ones in which the Poissonian peak appears is quite beneficial as the number of accidentals in the system is proportional to the coincidence window chosen (Δt). In our experimental set-ups we chose to use 500 bins for our histogram hence all our coincidence rates are calculated in a coincidence window of 1.5ns. As previously mentioned, the timing module just described is used in all experiments except the one described in chapter 5. This is because the experiment in chapter 5 is not limited to two output arms, but it contains four. A special time module was therefore employed which allowed the measurement of coincidence events from four different detectors. This time module was set to a temporal window of $\Delta t = 25\text{ns}$.

2.1.3 Klyshko advanced wave model

In parametric down-conversion, one can define coincidence detection as a simultaneous detection of the signal and idler photons. In general, during any experiment involving entangled states, the probability of detecting both the signal and the idler photons in their respective states represents the quantum mechanical prediction of the measurement outcome and is proportional to the coincidence rate. But detecting coincidences in a photon experiment is not always very easy in that a coincidence

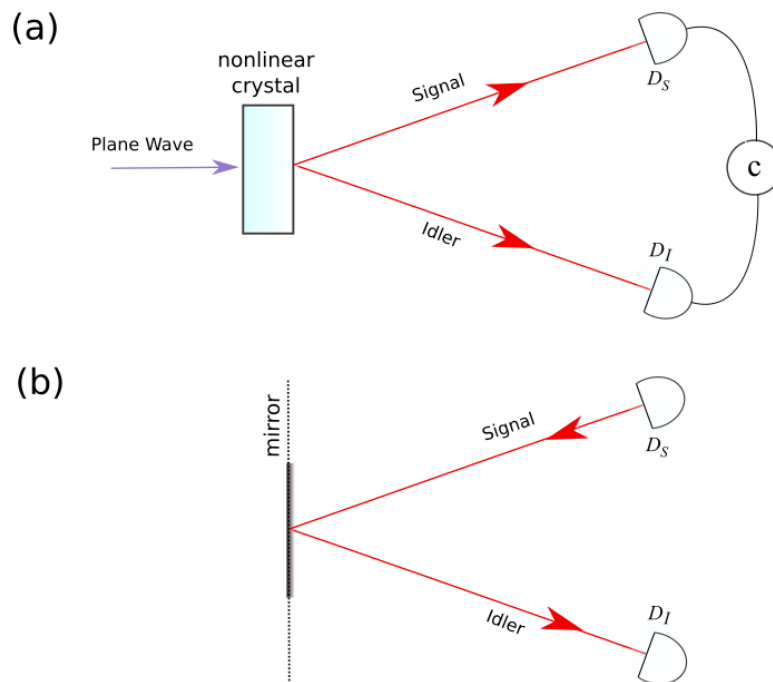


FIGURE 2.3: Schematic representation of the Klyshko advance wave picture where (a) represents the basis for all quantum correlation set-ups and (b) shows the classical counterpart to (a) as defined by Klyshko picture

rate only exists if the detectors are arranged to satisfy energy and momentum conservation and to have equal time delays. In 1988, David Klyshko formulated a different approach to predicting measurement outcomes through the use of an advanced-wave retrodiction model [34]. His approach, known as the Klyshko picture, arises from a rigorous formulation of quantum mechanics and is based on the fact that in a retrodictive model, a quantum system at any point in time between preparation and measurement is described in terms of its measured state, evolved backwards in time [34]. He therefore proposed a “back-propagating” model that allows for the prediction of the quantum correlations through a classical analogue. In particular, he showed that the quantum set-up, consisting of two detectors measuring the coincidence rates of the signal and idler photons generated through SPDC is equivalent to a classical set-up where one of the detectors is replaced with a light source and the down converted crystal acts as a mirror as above in figure 2.3. It is important to point out

that this model has now been verified by various experiments, most notably by ghost imaging experiments [35]. In my thesis I will therefore use this method for the design of the numerical simulation of my experiments.

Chapter 3

Encoding information in Aperture Limited Systems

3.1 Introduction to Quantum Communication

Communication is an important part of human society and it is closely linked to the development of civilisation. With the advancement of technology, new complex methods of communication have arisen making it possible to send information over large distances in very little time. This has inspired the development of the area of research called information theory.

Information theory was established by Claude E. Shannon in 1948 in a seminal paper called “A Mathematical Theory of Communication” [36], where he laid the basic elements for a general theory of communication and derived an equation to quantify the information that can be conveyed by a communication system. He was not the first to link information and probability, as Boltzmann and his followers had previously shown that information is the entropy associated with the probability distribution [1]. Shannon was, on the other hand, able to build upon this work and

link entropy to the quantity of information conveyed in a communication system. In his seminal paper, he derived two theorems that place upper limits on the ability to communicate information, and are the foundation of information and communication theory: the noiseless coding theorem and the noisy channel coding theorem [1].

In particular, the Shannon noiseless coding theorem sets a minimum limit on how much a message can be compressed whilst still maintaining its information without error [1]. This limit is shown to be a function of the entropy of the message sent and of the size of the alphabet used. On the other hand, no matter how large an alphabet is used, there is still a maximum amount of information that can be sent through a channel. This is given by the Shannon noisy channel coding theorem, which calculates the redundancy needed in order to combat noise in the channel used, therefore setting a theoretical maximum for the information transfer rate of the channel [1].

As communication channels are not limitless, a need arises to find means of communications that minimise the errors in transmission, while maximising the information capacity. In communication systems the most common method of maximising the information of each signal (i.e. increase the alphabet used) is to exploit the degrees of freedom of light in what is known as multiplexing. In particular there has been a great development in time, polarisation, and wavelength multiplexing schemes in order to satisfy the growing need of transmission capacity of current communication systems [37, 38]. These developments have brought current communication systems to reach information transfer rates close to the upper limits dictated by the channel's capacity [38]. Consequently, in recent years, there has been a growing interest in using the less developed degree on freedom of light i.e. the transverse or spatial degree of freedom of light to encode information [39–42]. It must be emphasised that the development of a new degree of freedom of light for communication channels is not meant as a simple replacement for previous multiplexing techniques. On the contrary, different multiplexing techniques can be used in conjunction with previous techniques

to enhance the channel's transmission capacity. Some recent examples can be found in the use of space-division multiplexing and dense wavelength-division multiplexing to achieve 112 Tb/s over a 76.8-km multicore fibre [43]; the use of spatial modes (in this case two orbital angular momentum modes) and wavelength-division (in this case 10 wavelengths) to achieve 1.6 Tb/s over a 1.1-km length of a special designed fibre [44]; and the use of spatial modes (in this case 12 orbital angular momentum modes), polarisation and wavelength-division multiplexing (in this case 42 wavelengths) in a free-space data link to achieve an aggregate capacity of 100.8 Tb/s [45].

Recent interest in using the spatial degree of freedom light is not only linked to the possibility it brings in enhancing the information transfer rates of communication channels but also for another potential application: cryptography and, in particular, quantum cryptography [46]. While standard classical methods rely on computational complexity to generate a secure communication channel, quantum cryptography relies on the properties of light to create a secure quantum channel [1]. Although the idea to use quantum systems for information security was originally proposed by S. Wiesner, the first protocol for quantum key distribution (QKD) was developed by Bennett and Brassard in 1984 [47]. These early protocols and quantum networks were based on the use of polarisation as the degree of freedom of light due to the well established knowledge of using polarisation as a degree of freedom for Bell-type tests. This had greatly expedited both the development of the theory itself and the development of optical tools for polarisation control [46]. Consequently, polarisation based secure quantum networks is a very active research field with cost-effective portable prototypes being recently developed which enable high secret-key distribution over a free space link of 145m [48]. It is important to note that the security of cryptography protocols is directly linked to the dimension of the Hilbert space or the number of mutual unbiased basis used in the protocol [49], the first being preferred as it also has the advantage of generating a larger secret key rate

compared to the latter [50]. In particular it has been shown that accessing high dimensional Hilbert spaces not only allows for a large encoding alphabet, but it also makes the communication harder to eavesdrop, as cloning fidelity scales inversely with dimensions. A high dimensional Hilbert space can also be crucial in certain QKD protocols as it allows for larger violations of Bell-type inequalities which is used in certain QKD protocols to reveal the presence of an eavesdropper [46]. In recent years the development of new techniques to employ spatial modes for quantum cryptography has therefore grown in popularity due to the fact that compared to some other degrees of freedom of light (e.g polarisation, time binning), the orthogonal transverse spatial structure of light is potentially infinite. The exploitation of this potentially unlimited Hilbert space is of great importance in the development of the new QKD protocols [9, 39, 50].

In this chapter, the information capacity of the two most known spatial modal sets, Laguerre-Gaussian and Hermite-Gaussian will be analysed in the context of a finite-aperture communication system.

3.1.1 Contributions

The study of the LG versus HG modes in a finite aperture system was undertaken here in Glasgow. This was done both experimentally and through modelling and the work is now published in *Optics Express* [18].

3.2 Encoding Information With Spatial Modal Sets

Photons have always been considered optimal for communication as they can transmit over long distances with little loss due to the absence of any known decoherence

mechanism in free space [51]. Compared to our current communication infrastructures, photons can not only travel in a confined medium (i.e., optical fibre), but can also be transmitted in free space, with recent experiments reaching terabyte data rates [51–55]. Free space optical communication is attractive as, compared to its fibre counterpart, it is a quick and reliable way to connect end users to their network in a cost-effective way, therefore being an optimal solution to what is known as the “last mile bottleneck” problem [56]. The advantage of spatial modes for communication has been known for some time, with the major limitation being technological [57–59]. With current advances in technology, such as the diode laser and the commercialisation of Spatial Light Modulators (SLM), being able to create and manipulate spatial modes of light has become easier and time efficient as compared to diffractive elements of fixed design, SLMs allow for fast switching between different states which can be easily implemented and optimised [40, 60, 61]. Consequently, the interest of the research community shifted from finding efficient ways to create and manipulate spatial modes, to developing strategies to best implement the characteristics of the modes and maximise the information encoded in each photon [62–64].

As previously mentioned, the use of spatial modal sets to increase information content is known as spatial division multiplexing. Various proposals have been made to generate an efficient spatial division multiplexing system. Some examples include encoding in plane waves i.e encoding by impressing phase information onto a cartesian coordinate [65]; LG modes; HG modes; more complex patterns for example airy beams [66]; or using an entirely different strategy in which the available telescope aperture is simply divided into multiple sub-apertures. All of these different encoding schemes have been designed to combat noise in the communication channel in order to try and send information as close as possible to the theoretical maximum transfer rate of the channel as defined by the Shannon theorem. The choice of encoding schemes is therefore dictated by the available technology and operating parameters

of the set-up used, and the circumstances under which the communication link is to be employed (i.e. the noise present in the system). However, noise is not the only limitation of a communication system. All real-life optical systems need to transmit and receive the information sent through the communication channel. It therefore follows that when setting up any free space communication system, the diffraction and loss due to the size and shape of the transmitting and receiving apertures must be considered. Specifically, the number N of low-loss channels that can be implemented in any given communication system, is given by $N \approx A_R A_T / (\lambda L)^2$, where A_R and A_T are respectively the area of the receiving and transmitting apertures, λ is the wavelength of light, and L is the distance between the sender and receiver. This value is known as the Fresnel number product of the sender and receiver [49, 63].

3.3 LG vs HG in a Finite-Aperture System

When comparing the information capacity of different spatial modes in an aperture limited system, regardless of what orthogonal base is chosen, the total number of modes transmitted with low loss should only be limited by the Fresnel number of the optical system [63]. However, as can be easily seen, this is not always true in practice. In this chapter, we demonstrate this by comparing the information capacity of the LG base and the HG base.

Both LG and HG modal sets are well known solutions to the paraxial wave equation making them examples of orthogonal bases in which any arbitrary light beam can be represented. In particular the LG modal set is a discrete cylindrical basis, which can be factored in an azimuthally only component, with angular dependency given by $\exp(-il\theta)$, where l is known as the azimuthal mode index and determines the number of wavefront helices for a light beam; and radial only component with mode index, p , where p represents the number of concentric, high-intensity, rings in the

transverse cross-section. It is important to note that the azimuthal component of the LG gaussian beam is what gives rise to the orbital angular momentum (OAM) of light which will be the topic of discussion of the next chapter. In comparison, the HG modal set is a discrete rectangular base, described by mode index m and n , where m and n correspond to the number of zero lines across the field in the y and x direction, respectively. It is important to note that higher order modes tend to diverge more quickly [67], therefore to make a fair comparison it is important to compare modes of the same order N . This is easily achieved when comparing LG to HG modes as a direct relationship exists between the two bases. In particular any LG mode of indices l, p , can be easily transformed into an HG mode mode of indices m, n and vice versa through the use of a pair of suitably spaced cylindrical lenses [68]. It therefore follows that any LG mode can be expressed as a linear combination of HG modes where $l = m - n$ and $p = \min(m, n)$ [69]. A direct comparison can therefore be made as long as the same mode order is chosen for both bases where $N = m + n = |l| + 2p$.

In a classical communication system, modes are generated by the sender, transmitted through the channel and finally detected by the receiver. Thus in order to assess the information capacity of the system, a correlation matrix can be constructed where the correlation between all possible modes in the modal sets can be either theoretically calculated or experimentally measured. As both HG and LG modes are orthogonal bases, from a theoretical standpoint there should be no cross-talk between modes i.e. the modes sent i and the ones received j should be either perfectly correlated or perfectly anti-correlated. In a communication system this matrix is known as the probability matrix $P_{i,j}$, where each element corresponds to the conditional probability $P_{i|j}$, of a received mode j given the sent mode i . It then follows that the total amount

of mutual information (MI) that can be carried by the system is given by [36]

$$\text{MI} = \sum_{i,j} P_{i|j} \text{Log} \left(\frac{P_{i|j}}{P_i P_j} \right). \quad (3.1)$$

When calculating the mutual information of a system it can be easily seen that the choice of logarithm base is completely arbitrary in that changing the base will simply define the units of information. In particular if the base two is chosen then the information is defined in “bits”, while if the natural logarithm is chosen the information is defined in “nats”. As binary systems are prevalent in information technology it is common practice to use the “bit” as the unit of measurement for information [1]. For the purpose of this study, the information capacity of the system is therefore calculated in ‘bits per photon’ (bpp), where

$$\text{bpp} = \sum_{i,j} P_{i|j} \text{Log}_2 \left(\frac{P_{i|j}}{P_i P_j} \right). \quad (3.2)$$

It is important to note that what has been discussed so far is not limited to classical communication systems, but can easily be extended to quantum systems (fig. 3.1). In particular, in a parametric down-conversion experiment, the probability matrix $P_{i,j}$ is simply the joint detection of the spatial mode of the signal photon (i) and idler photon (j) respectively. Accordingly, each element of the matrix corresponds to the conditional probability $P_{i|j}$, of detection of mode i given the detection of mode j .

Experimental Set-Up

As previously mentioned there is currently a great interest in quantum communication systems. For the purpose of this study we therefore chose to use a correlated single photon system to illustrate the effect of modal choice, in an aperture limited communication system.

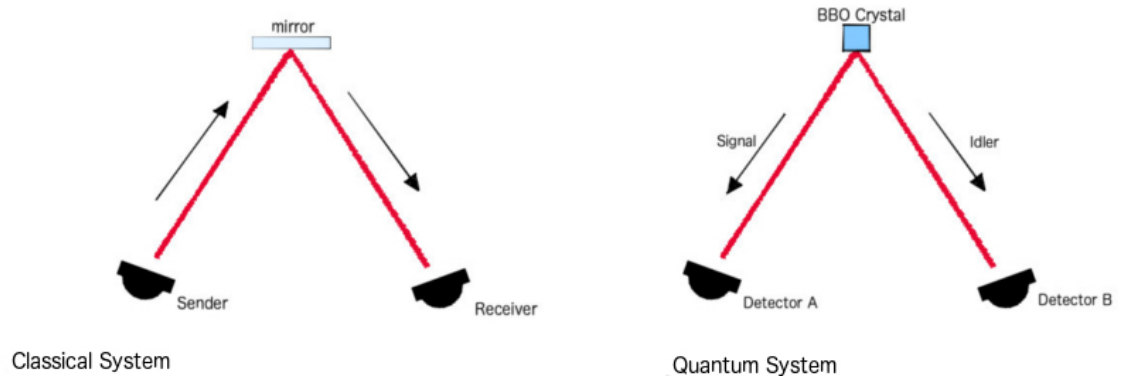


FIGURE 3.1: Comparison between a classical and a quantum system.

Experimentally, this is achieved by pumping a 3mm long BBO crystal with a 355nm CW laser to generate down-converted signal and idler beams at 710nm (fig. 3.2) [18]. The residual pump beam is then blocked through the use of a longpass filter. The remaining signal and the idler beams are then separated by a beam splitter and imaged onto two separate SLMs. The plane of the SLMs are themselves imaged to the entrance facets of single mode optical fibres, that are connected to single-photon counters. These counters are connected to an electronic coincidence detection circuit where the photon coincidence rate is recorded as a function of the measurement states as specified by the SLM.

The use of an SLM to generate and transform optical spatial modes is quite common in both quantum and classical communication systems as, compared to elements of fixed design, it allows for convenient switching between different states [40, 60, 61]. In our experimental set up, the SLMs are therefore used to impart the phase structure of the different modes onto the fundamental modes of the optical fibre. It can easily be seen (fig. 3.3), when setting up a quantum communication system, careful consideration must be given to the size of the pump beam used, the fibre waist and the mode waist as designed by the SLM. In particular, there are two important ratios to consider: (i) the waist size of the pump beam compared to that of the fibre and (ii) the waist size of the mode as designed by the SLM compared to that of the

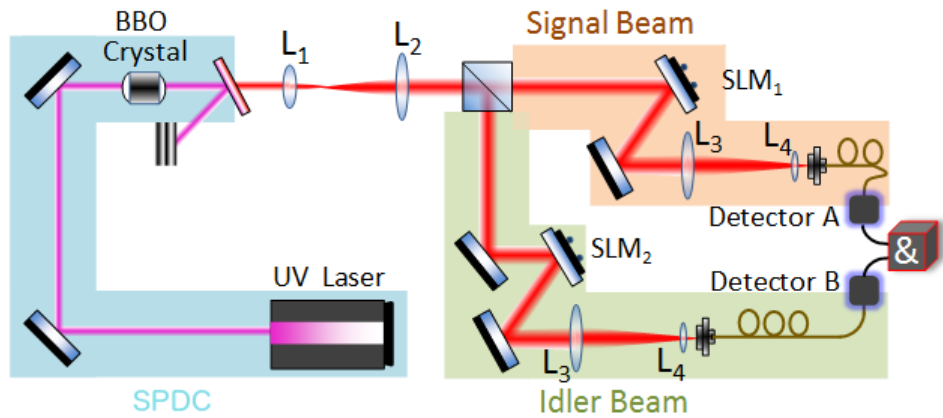


FIGURE 3.2: Experimental set-up [18]. A CW UV (355 nm) laser is used to produce spatially correlated photon pairs at the BBO crystal. The correlated photons are separated by a beamsplitter and imaged through the use of two lenses $L_1=200\text{mm}$ and $L_2=400\text{mm}$ onto two separate SLMs. The plane of the SLMs are then themselves imaged through the use of the lenses $L_3=600\text{mm}$ and $L_4=2\text{mm}$ onto the entrance facets of single-mode fibres. These fibres are connected to two SPAD detectors which are in turn connected to an electronic coincidence machine.

fibre. As demonstrated in previous works, the ratio of the width of the pump beam

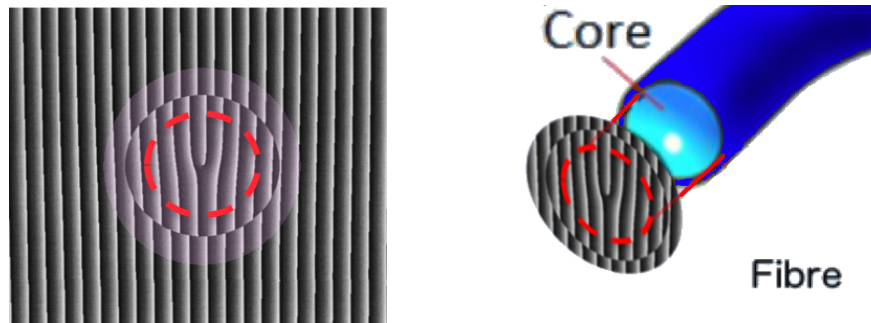


FIGURE 3.3: An example of the SLM phase pattern. The figure represents both the entangled photons beam (light pink circle), and the fibre waist being imaged onto the SLM pattern (red circumference). In particular this is for a non optimal mode to fibre waist ratio.

compared to the detection modes is responsible for the bandwidth of the entangled states [24]. For the purpose of this experiment, careful attention is taken in setting up the experiment so that in the plane of the SLM, this ratio is greater than one i.e. the size of the pump beam as imaged on the SLM is larger than that of the fibre waist. It therefore follows that, for the limited number of orthogonal modes tested in our experiment, we expect perfect orthogonality. In particular, we expect to measure

a high coincident count rate when the SLMs are programmed to detect modes that are complex conjugates of each other [70–73].

Having chosen a suitable pump beam to fibre waist ratio, so as to not make it a limiting factor in our experiment, the second ratio, i.e. the mode to fibre waist ratio, is considered. As previously mentioned, the spatial correlations of our entangled photons are studied through the use of SLMs that impart the phase structure of the different modes onto the fundamental mode of the optical fibre. As the optical fibres have a set aperture, when imaged onto the the plane of the SLM, they will demarcate a fixed modal waist. Hence, when designing the SLM's hologram a careful consideration must be taken in choosing its lateral scaling. In particular, the degree of orthogonality between the measured modes is directly linked to the proportionality between the phase term imaged on the SLM and the gaussian mode defined by the image of the fibre core on the SLM. For the purpose of this experiment we choose to compare the information capacity of both the LG and HG modal bases at different mode to fibre ratios in order to assess their resilience to the cross talk imposed on the system by the fibre aperture.

Modelling

The comparison between the two modal sets was not only performed experimentally but was also numerically simulated using a computer generated model. When designing the model, two characteristics of the experiment were taken into consideration: (i) the use of phase only SLMs to impart the desired modes onto the signal and idler beams and (ii) the fact that all components of the experimental set up are imaged onto each other. The first of these characteristics allows us to generate a simplified version of a communication system model as only the phase structuring of the Gaussian beams needs to be considered. Similarly, the later characteristic



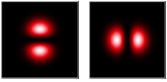

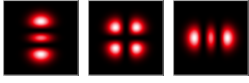
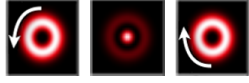
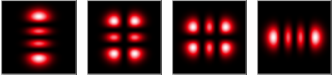
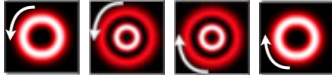
allows us to further simplify the model as the propagation of the beam does not need to be taken in consideration. The predicted correlation strength between the spatial modes imparted on the signal and idler photons can therefore be calculated by simply measuring the overlap integral between the two modes.

Results

The aim of the experiment was that of calculating the information capacity of the LG and HG modal sets in our aperture restricted system. Hence, the correlation between all modes within the set was calculated for different mode to fibre ratios (figs. 3.4, 3.5).

As the LG and HG modal sets are infinite, in order to test their information capacity, a choice had to be made on the number of modes to be tested. For our experiment we choose to compare all modes with mode order $N \leq 3$ (table 3.1). This allowed us to evaluate enough modes to make an informed conclusion without running into experimental complications that arise when generating higher order modes [74]. A range of 10×10 correlation matrices were therefore generated for both the LG and HG modal sets for different mode to fibre ratios. These matrices were then used to calculate the corresponding total mutual information through the employment of equation 3.2. Figure 3.4, displays the resulting data calculated with the model, while figure 3.5 displays the data measured from the experimental system. For analysis purposes, a sample of the correlation matrices used to calculate the bpp are also displayed. In particular, we chose to show the correlation matrices generated for both the LG and HG modal set when the mode to fibre ratio is both close and far from optimal. The latter correlation matrices are particularly interesting for our study as they help us to shed some light on the source of the cross talk and therefore allows us to postulate conclusions which are independent of the mode order tested.

TABLE 3.1: Intensity profile for LG and HG modes with mode order $N \leq 3$ [18]. In the case of the LG modes, the direction of rotation of the azimuthal phase term is indicated with an arrow.

Mode order N	Hermite Gaussian (m, n)	Laguerre-Gaussian (l, p)
0	 0,0	 0,0
1	 1,0 0,1	 +1,0 -1,0
2	 2,0 1,1 0,2	 2,0 0,1 -2,0
3	 3,0 2,1 1,2 0,3	 3,0 1,1 -1,1 -3,0

As can be seen in figure 3.4, and figure 3.5 respectively, both the modelling data and experimental data exhibit very similar trends. In particular, there is a striking visual agreement between the correlation matrices generated through our model and the ones measured in our experimental system, albeit the latter resulting in lower bpp. This is not abnormal, rather it is expected as modal impurities are harder to control in an experimental setting. Despite this we were still able to take steps to counteract unnecessary noise in our system that can skew our results. One such step was that of expressing our correlation matrices as a function of the quantum contrast (QC) measured rather than the coincidence measured where QC is simply defined as the ratio between the measured coincidences and the expected accidental

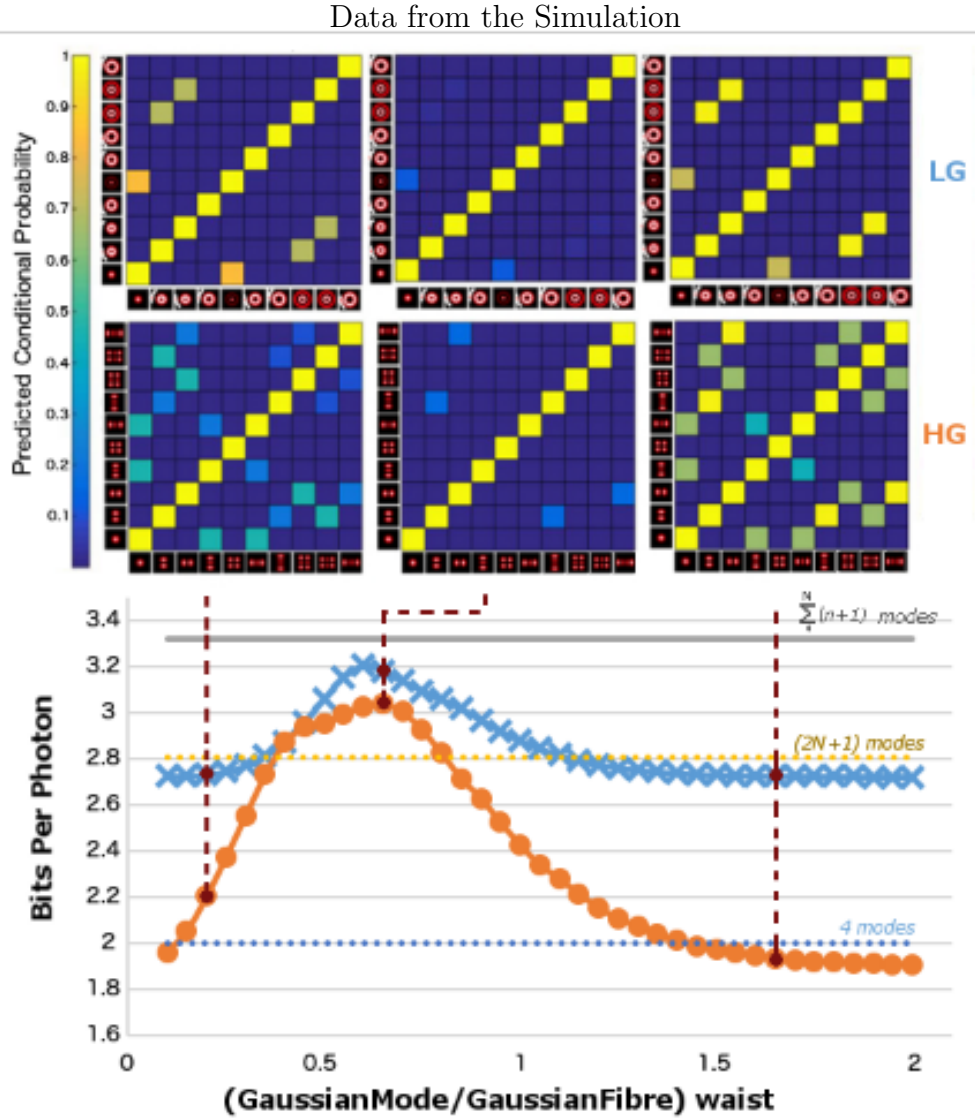


FIGURE 3.4: Results from the simulation of the experiment [18] This graph shows the value of bpp generated through the modelling system. In particular, the information capacity of the LG modal set is shown in blue while the corresponding values for the HG modal set are represented in orange. Some of the correlation matrices used to calculate the bpp are also displayed. Finally, for analysis purposes, three value of bpp are also displayed: the bpp corresponding to a system composed of only four orthogonal modes; the bpp corresponding to a system with $2N + 1$ orthogonal modes (i.e. the total subset OAM modes for an $N \leq 3$ LG modal set);

the bpp expected if the spatial modes where perfectly correlated ($\sum_{n=0}^N (n + 1)$).

coincidences (as defined by eq. 2.4 in chapter 2). This is particularly important for elements with low-count rate where the presence of accidental coincidences can be mistaken as a weak correlation. Nevertheless, accidentals are not the only cause

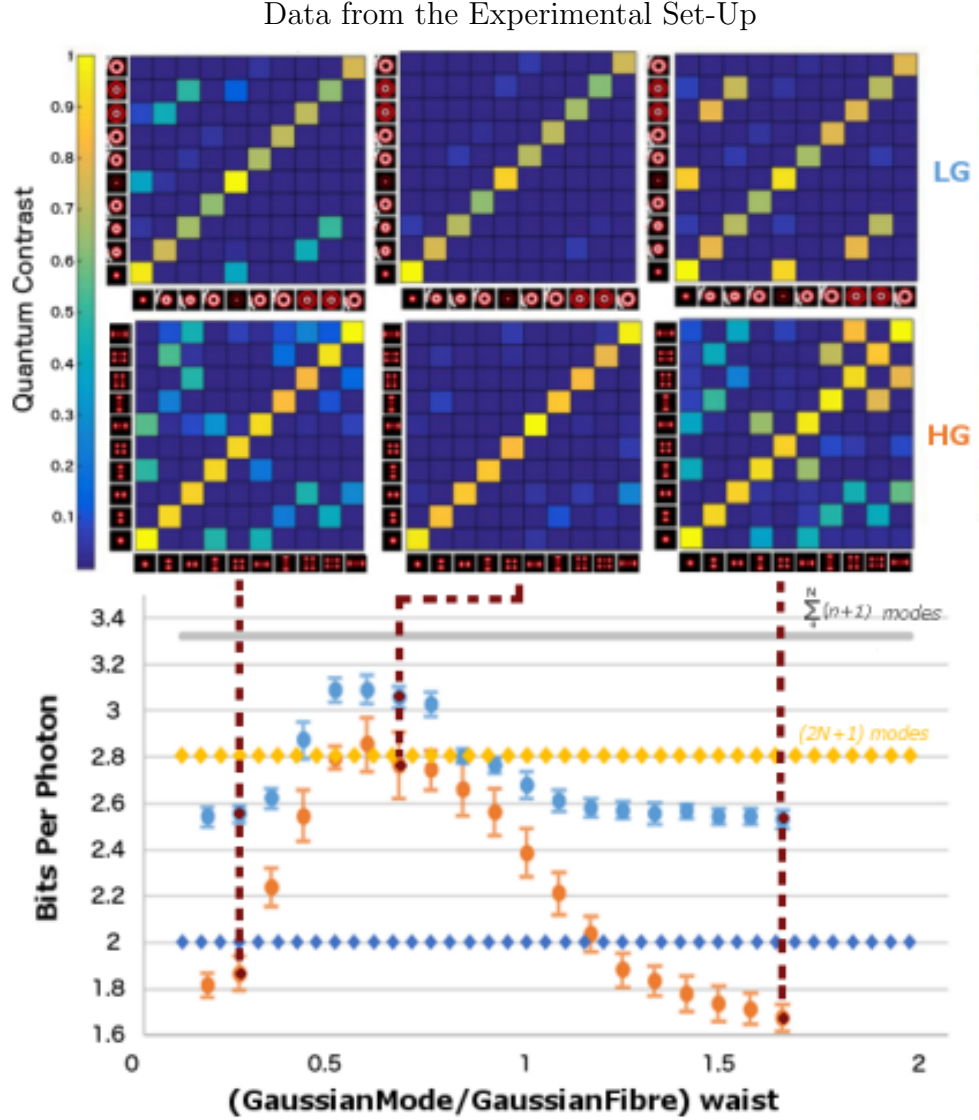


FIGURE 3.5: Experiment Data [18]. This graph shows the experimental set-up for different mode to fibre ratios. As for the modelling in figure 3.4, the information capacity of the LG modal set is shown in blue while the corresponding values for the HG modal set are represented in orange. Some of the correlation matrices measured in our experiment and used to calculate the bpp are also displayed. As for fig. 3.4, three value of bpp are displayed: the bpp corresponding to a system composed of only four orthogonal modes; the bpp corresponding to a system with $2N + 1$ orthogonal modes; the bpp expected if the spatial modes where perfectly

$$\text{correlated } \left(\sum_{n=0}^N (n + 1) \right).$$

of noise when calculating correlation matrices. Slight cross-talk can appear from a series of experimental factors, some examples being modal impurities of the pump beam or limitations in the generation of the modes due to SLM pixelation. Hence, in

our experimental data, the non correlated elements, although low in value, are never perfectly zero (as seen in fig. 3.5). In order to reasonably assess the information capacity of the modal sets, a background noise subtraction was performed on each correlation matrix prior to the calculation of its bpp. Finally, it is important to note that, in contrast to a computer simulated modelling system, an experimental system result will vary slightly between each run. We therefore choose to perform the experiment 10 consecutive times plotting the average bpp of the 10 runs, along with the corresponding error, as a function of the waist ratios, (figure 3.5).

Analysis and Discussion

From figures 3.4, and 3.5 it can be concluded that our modelling system is quite effective in predicting the features and trends present in the experimental system. In particular, for both the simulation and experimental data the information capacity of the LG modes either equals or exceeds that of the HG modes for all aperture ratios. This result can be understood by looking at the correlation matrices generated for both the LG and HG modal sets when the aperture ratio is not optimal.

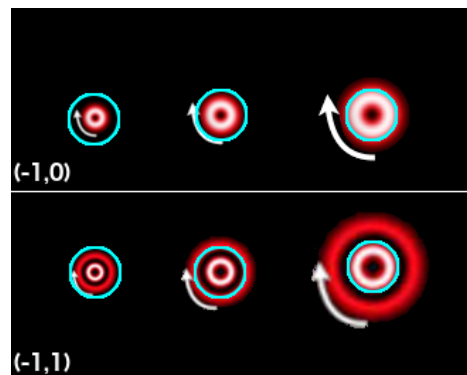


FIGURE 3.6: Example of the phase fronts for LG modes $l = -1, p = 0$ and $l = -1, p = 1$ at different waist ratios. In the image the blue circle represents the fixed fibre aperture. As can be seen, for large waist ratio the radial information is lost and the two modes are therefore no longer distinguishable.

For an optimal aperture ratio the correlation matrices for both the LG and the HG modal sets are almost a perfect diagonal. However, as can be seen in figures 3.4, and 3.5, this no longer holds true for non-optimal aperture ratios. In particular, in the case of the LG basis, when the aperture ratio is no longer optimal, cross-talk appears between modes with the same l but different p . This can easily be explained by the fact that, while the presence of an on-axis circular aperture may restrict the information carried by the radial component of the modal set (see figure 3.6), it has no effect on the azimuthal component. In other words, the presence of a limiting aperture does not alter the helicity of the phase-fronts. It therefore follows that, irrespective of the mode order N chosen, if the LG modal set is used, there will always be $2N + 1$ orthogonal modes present. Hence, in the case tested in our experiment, i.e. $N = 3$, if we consider the number of orthogonal modes alone, we would expect all values of LG to be greater or equal to 2.8 bits per photon. This is, however, based on the assumption that all orthogonal modes have the same correlation strength. This is not true for both the LG and HG modal sets, where the strength of the correlations between highly correlated modes depends upon the modes itself i.e. the strength of the correlation decreases as the mode's order increases. Hence, the mutual information calculated when running our simulation system is slightly below that which might have been expected from the number of orthogonal modes alone.

On the other hand, as can easily be seen in figures 3.4, and 3.5, the HG modal base is more susceptible to cross-talk than the LG modal base for non optimal aperture ratios. More specifically, in the case of the HG modal base, as the aperture ratio of the system becomes less optimal, cross-talk appears between modes with the same parity (see fig. 3.7). In other words, in the presence of a non-optimal aperture ratio, information on the number of horizontal (n) or vertical (m) nodes is lost and only information on the symmetry of the modes is retained (see fig. 3.8). As HG is a rectangular modal base, each mode has two axis of symmetry, the vertical and

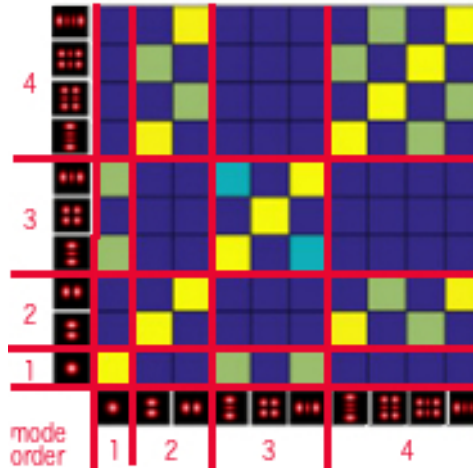


FIGURE 3.7: Simulated correlation matrix for the HG modal set with a non optimal aperture ratio. In this correlation matrix a red line has been drawn to separate modes of different orders for analysis purposes.

horizontal axis, and can either be symmetric (EVEN) or antisymmetric (ODD) compared to these two axis. It therefore follows that for non-optimal aperture ratios only 4 orthogonal states can be distinguished: (i) the mode is symmetric in both the vertical and horizontal axis i.e. both m and n are even; (ii) the mode is antisymmetric for both axis i.e. m and n are odd; (iii) the mode is vertically symmetric and antisymmetric horizontally i.e. m is even and n is odd; (iv) the mode is vertically antisymmetric and symmetric horizontally i.e. m is odd and n is even. Hence, for HG modes with a non-optimal aperture ratio, the information capacity of the system has a limit of 2 bpp irrespective of the modal set used, where this corresponds to the information capacity of a system with only 4 orthogonal modes (see figs 3.4, 3.5).

The advantage of the LG over the HG measurement set for an aperture restricted system is therefore readily understood as, irrespective of the aperture ratio the information capacity of the LG modal set will always exceed or be equal to the HG set. It is important to note that, while all our analysis has been done using a modal set of 10 modes, i.e. $N \leq 3$, our conclusions are general and can be extended to a modal set of any mode order. Moreover, as the size of the modal set increases so does the advantage of using a LG modal set compared to the HG modal set. This can easily

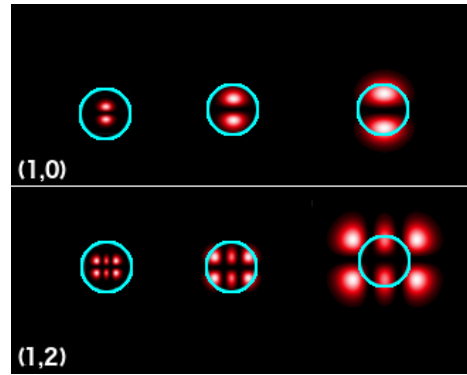


FIGURE 3.8: Example of the phase fronts for HG modes $m = 1, n = 0$ and $m = 2, n = 1$ at different waist ratios.

be deduced from our analysis as the information capacity of the HG modal base for a non-optimal aperture is a set value irrespective of the size of modal set while in the case of the LG modal base the number of modes that are not effected by the aperture restriction of the system increases with the mode size used (see figure 3.9).

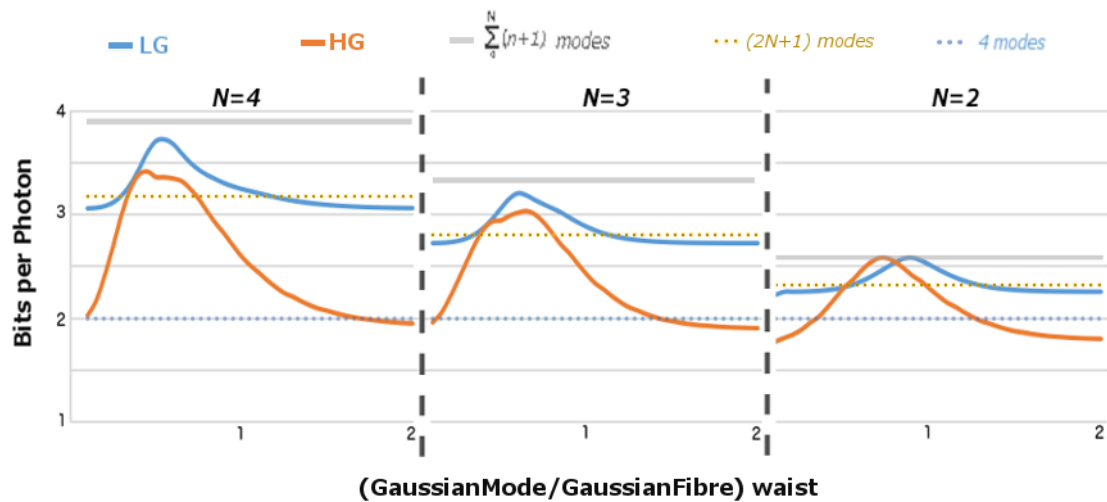


FIGURE 3.9: Bpp for different N calculated using the modelling system. In particular, we chose to compare the information capacity of the LG and HG modes for $N=2,3$ and 4 [18].

3.4 Conclusion

It is important to note that the conclusion reached in this chapter is simply based on the boundary conditions of the system. In particular, for this experiment careful consideration was taken in making the circular aperture size of our detecting fibres the only limiting factor of the system. For example, these results are only calculated for the specific case of all the apertures being co-axial and the advantage of the LG set does not necessarily extend to an axis displacement. In particular it has recently been shown that, in a system in which the aperture is not a limiting factor, when the modal bases are laterally displaced along a symmetry axis, the information capacity of the HG modal base can exceed the LG base [75]. Furthermore, another factor not considered in our analysis is the losses associated with the two sets. In particular, due to their helical phase fronts LG modes exhibit zero on-axis intensity: hence, a restricted aperture may introduce additional loss compared to the HG. As a quantum communication system is already a signal-starved environment, a reduction in photon flux may effect the ability to distinguish real coincidences from accidentals, hence reducing the information capacity of the modal set.

In this chapter we were able to demonstrate, from both a theoretical and experimental perspective, that for a restricted and/or measurement aperture in an optimal communication system, the information capacity of the LG model set possesses the capability of exceeding, or at minimal equalising the HG set. Furthermore, even though both model sets are affected by cross talk imposed by the aperture restriction, the LG model set has shown much greater resilience to cross talk than the HG set. This is of high importance as this conclusion is not limited to just quantum systems, but it also has validity for classical systems, where the two modes are the transmitted and received modes in a communication link.

Chapter 4

OAM in a Communication System

4.1 Introduction

Ever since the discovery by Allen, Woerdman and associates [57] that light beams with helical phase-fronts carry orbital momentum there has been a great interest in using this property of light in developing new optical applications. The idea that light not only carries energy but can also carry momentum is not a new one in physics as it is a property embedded in Maxwell's equations. Nevertheless, the first derivation of angular momentum from Maxwell equations didn't appear until 1909 when Poynting was able to show, through mechanical analogies, the existence of angular momentum in circularly polarised light [76]. This angular momentum is known as spin angular momentum (SAM) and it arises from the individual photons of the light beam either spinning in the left handed direction, with $SAM = -\hbar$, or right handed direction, with $SAM = \hbar$, when viewed from the direction of propagation. In 1936 Beth was able to measure this effect for the first time by showing that by allowing polarised light to pass through a half waveplate, a rotation can be induced in the latter [77]. It is important to note that any polarisation state of light can be expressed as a superposition of left or right circular polarisation and therefore SAM can be any

value between $-\hbar$ and \hbar . However, SAM is not the only momentum that a light beam can carry. In 1932 Darwin, grandson of the famous naturalist, demonstrated the existence of an additional momentum of light not bounded by the light beam's polarisation [78]. In his study of atoms he observed that when photons were emitted at short radius away from the centre of mass of the atom, the linear momentum of the emitted photon would lead to an additional torque acting on the centre of mass. This momentum is known as orbital angular momentum (OAM) and it can potentially have values many times larger than SAM. However, until the discovery by Allen and associates, it was believed that OAM was a rare phenomena, only present in high order atom transitions. In particular, in their groundbreaking paper, Allen et al. showed that any beams with an azimuthal phase dependence of $\exp(-il\theta)$ carry OAM of $l\hbar$, where l is the azimuthal index and θ is the azimuthal angle [57]. An important note to make is that the presence of helical phase fronts require a phase singularity running along the beam axis, resulting in an area of zero intensity and therefore creating what is known as an 'optical vortex' [79]. The presence of this 'optical vortex' makes OAM very important also for applications outside of entanglement, notable examples being its use in optical manipulation, imaging and the most relevant for this work, its application in optical communications systems [80]. In particular, OAM has been shown to have advantages not only for its potential possibility to encode an arbitrary large amount of information but also for its robustness against eavesdropping, quantum cloning and maintaining a secure transmission in a highly noisy channel [59]. Hence, following Gibson et al. demonstration of a free-space communication system using OAM in 2004 [61], there has been a great interest in the development of OAM communication systems with recent experiments being able to achieve TeraBit rates of data transfer [53]. In addition, the feasibility of using OAM for communication over large distances has also been shown, with OAM carrying photons being received as far as 143 km from the sender [81]. This is in no means an exhausted field of research, as new ways of generating and controlling OAM are being

proposed every year and experimental communication systems are rapidly advancing toward becoming viable commercial applications [80, 81]. In particular, with the advance of technology, especially in the field of nanofabrications, new techniques for the creation of optical vortex beams are being implemented [82]. One such new proposal is that of an analog OAM generator [19]. This new technique allows for control over the OAM of light continuously, including all rational states, all integer orders and fractional orders between them.

4.1.1 Contributions

The work in this chapter was carried out as part of a collaboration with the *National University of Singapore* on a project involving continuous shaping of photons with arbitrary rational orbital angular momentum (OAM). In particular, our collaborators in Singapore proposed the project and designed the grating discussed in this chapter. As part of the collaboration I was responsible for implementing the grating in a quantum communication system in order to test the feasibility of using the designed vortex beam for quantum communication systems. This work is now published in *Light: Science & Applications* in a research paper of which I am one of the joint first authors [19].

4.2 Generation of Continuous OAM beams

The study of optical vortices precedes the discovery of OAM [83]. In particular, this phenomena attracted great interest as it was shown not to be limited to light but to also originate in acoustic waves, electrons and neutrons [82]. It wasn't until the discovery that this phase singularity with a spiral wavefront carried quantised OAM

that the potential for communication became evident. Since then, a great deal of work has gone into devising new methods of generating optical vortices[82].

The first experiments following Allen et al.'s discovery were based on OAM beams generated by converting HG beams into LG beams using cylindrical lenses [69]. This was swiftly followed by a more direct method of generation where the light beam picked up the integer phase step along the azimuthal angle by interacting with a phaseplate that had a spiral inhomogeneity in the longitudinal direction [84]. With the invention and commercialisation of computer interfaced diffractive optical elements, SLMs and DMDs being some examples, the generation of OAM through the use of fork gratings became widespread. This is not a new technique as it was first implemented in 1990, when it was shown that a fixed diffraction grating containing a fork dislocation centered on the beam axis generated a first-order diffraction beam with a helical phase front [85]. It also must be pointed out that, compared to the cylindrical lens technique, this is a phase-only approach, and therefore creates only approximations of the desired modes. This loss in modal fidelity can often be tolerated when considering the unprecedented level of control over the generation of holograms that SLMs allow. In the case of modern communication experiments this transpires in the ability to rapidly generate and switch between different holograms, and consequently OAM states, without the need to physically modify the system. The generation of these digital holograms has been the centre of many subsequent studies with different techniques now existing for optimising the generated holograms in order to both create purer modes and correct for any aberrations arising from the optical elements, transmission medium or the hologram itself [86–88]. To generate OAM all of the mentioned techniques imprint a $2\pi l$ step in the phase of the propagating field where l is an integer. It is possible, however, to generate phase jumps that are not multiples of 2π [89]. This is known as non-integer, or fractional OAM and contrarily to the perfect helical structure of integer OAM these structures comprise

of many vortices at differing positions within the beam cross-section [90]. Interest in generating non integer OAM for quantum communication systems became very compelling when it was shown that conservation of OAM does not apply to only integer OAM but also pertain to superposition of OAM states [91] and to fractional OAM [71].

As the field of quantum communication briskly advances towards the commercial arena, there is an increased need for new techniques that allow for flexible and fast control of beams carrying OAM. It is in this context that our collaborators from the National University of Singapore designed and developed a new technique for the generation of beams carrying fractional OAM [19]. In particular, they designed a bilaterally symmetric grating which allows for the generation of beams with a phase profile containing regularly distributed singularities. When this grating is encoded into a beam generator, it generates optical vortices which can be tuned by allowing a gradually varying aperture to control the number of singularities present in the beam. A greater control is therefore gained in the generation of OAM as theoretically any arbitrary rational-order vortex beam can be generated by smoothly varying the limiting aperture, including all rational states, all integer orders and any fractional orders between them. It is important to point out that this is the first analog generator proposed for the generation of OAM states as, contrary to all previous methods, it allows for continuous generation of multiple OAM states in a single device. The possible applications for analog OAM generators are therefore still to be fully explored.

One area, pertinent to my studies, that can benefit from a device that is able to manipulate the OAM state of light in a continuous basis is that of quantum communication. Two experiments were therefore performed, using the quantum communication set-up described in chapter 3, to test the feasibility of this OAM generator for quantum communication systems. In the first experiment, the quantum spiral spectrum of the

OAM was measured. More specifically, we use entangled photon pairs to characterise the ability of this new technique to generate OAM states. This is done by studying the correlations between photons that have been converted into OAM states through the use of the new proposed hologram and photons projected into integer OAM states by the more traditional fork grating hologram. Having established that the proposed mechanism is valid for the generation and manipulation of OAM modes at a single-photon level, a second experiment was carried out to study the correlation strength of the modes. By tuning the OAM generators on both the signal and idler beams we were able to show a smooth diagonal correlation matrix, therefore demonstrating the applicability of this method for quantum communications.

4.3 Experimental Set-Up and Data Analysis

As previously mentioned, the system configuration used in this experiment is similar to the one described in the previous chapter, as both projects are interested in the study and development of techniques to encode and transfer information through a quantum channel. In particular, our photon pairs are generated through SPDC, separated by a beam splitter and imaged onto two individual SLMs. The resulting signal and idler beams are then imaged onto the facets of single-mode fibres connected to two separated SPAD detectors and the coincidence rates are recorded as a function of the states specified by the SLMs (see fig. 4.1).

A unique feature of this experiment is the design of the hologram used to impart the desired phase onto the beams. As explained in the premises of this chapter, our Singapore collaborators have designed (and tested in a classical communication system) a bilaterally symmetric metagrating capable of generating continuous OAM which can be tuned to any desired value by varying the size of the aperture conveniently placed in front of the hologram (see reference [19] supplementary materials).

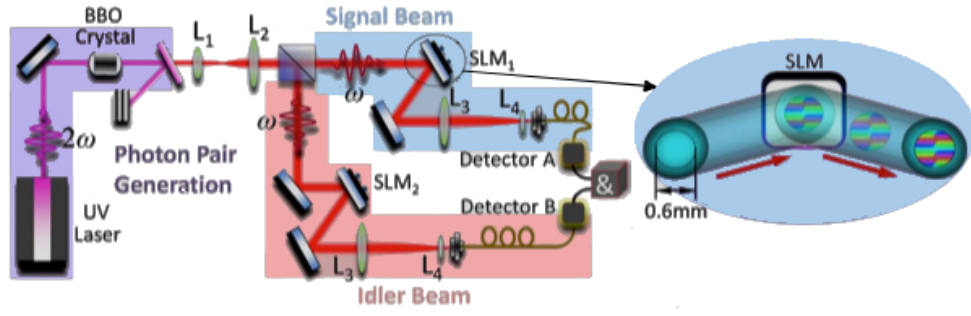


FIGURE 4.1: Experimental set-up [19]. As for the set-up in chapter 3, the entangled photons were generated using SPDC, separated by a BS and imaged (with $L_1=200\text{mm}$ and $L_2=400\text{mm}$) onto two separate SLMs which are in turn imaged through the use of the lenses ($L_3=600\text{mm}$ and $L_4=2\text{mm}$) onto the single-mode fibres. The fibres are then connected to two SPAD detectors. In this set-up the SLMs are used to generate the required phase profiles as designed by the hologram we designed. A pinhole, with a diameter 0.6mm , is also designed directly on the SLM to approximate the 2mm gaussian idler and signal beams into flat-topped illumination beams.

In particular, the metagrating was designed as a vortex transmitter composed of two gratings (with grating period Λ) which were arranged symmetric along the y -axis and tilted away from each other by an angle γ (as schematically displayed in figure 4.2(a)). When this grating interacts with a normal incident plane wave, the resulting first-order diffracting beam carries a linearly y -dependent phase function given by:

$$\chi(x, y) = e^{\text{sgn}(x)i\beta y} \quad (4.1)$$

where $\text{sgn}(x)$ refers to the sign function of the variable x and β is a constant phase gradient along the y -axis that depends on both the grating period Λ and inclination angle γ . In particular

$$\beta = \frac{2\pi \tan \gamma}{\Lambda \sqrt{1 + \tan^2 \gamma}}. \quad (4.2)$$

As can be noted in fig. 4.2 (b), the phase function generated presents equally spaced-out phase singularities along the y axis, where the distance τ between two consecutive singularities is given by $\tau = \pi/\beta$. A pinhole placed between the plane wave and the

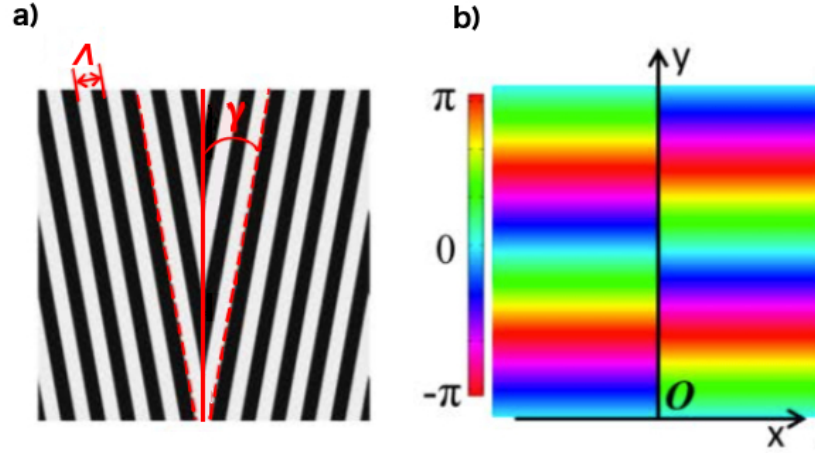


FIGURE 4.2: Vortex beam generator (images were published in the supplement materials of [19]). (a) Sketch of the bilaterally symmetric grating, with grating period Λ , used to generate the desired vortices. In the image the black and white bars represent opaque and transparent areas of the transmitter. (b) Phase profile encoded in the vortex transmitter as given by equation 4.1.

hologram can therefore act as a vortex regulator. In particular, by varying the diameter size d along the y -axis of symmetry one can control the number of singularities present in the phase of the transmitted beam i.e. the average OAM imparted on the beam by our transmitter (fig. 4.3 (a)). It is important to note that by smoothly varying d , the number of singularities present in the phase front is given by $q = d/\tau$ where q is not always an integer but can be any fractional value. However, as can easily be seen from our work in chapter 3 our quantum communication system is already an aperture limited system, where the aperture size is fixed and dictated by the size of the core of the optical fibres. Hence, for our quantum experiments, we choose to control the singularities present in the beam (q) not by varying the aperture size, but by smoothly varying the phase gradient (β) of the hologram along the y -axis, i.e. in our quantum experiment, for different singularity strengths (q), d is a fixed value set by the communication system, and τ is smoothly controlled (see fig. 4.3). This is of course, not very practical with a fixed metagrating transmitter where β , and consequently τ , are set at the manufacturing level. Hence, for the quantum experiments, we choose to create and control the vortex generating grating through

the use of SLMs (see 4.1). It must be noted that, contrarily to the metagrating transmitters, as SLMs have a pixel resolution limit, they cannot, in principle, generate a rigorously continuous OAM. This nevertheless does not impede the use of SLMs for this experiment as this effect is negligible for smaller values of OAM.

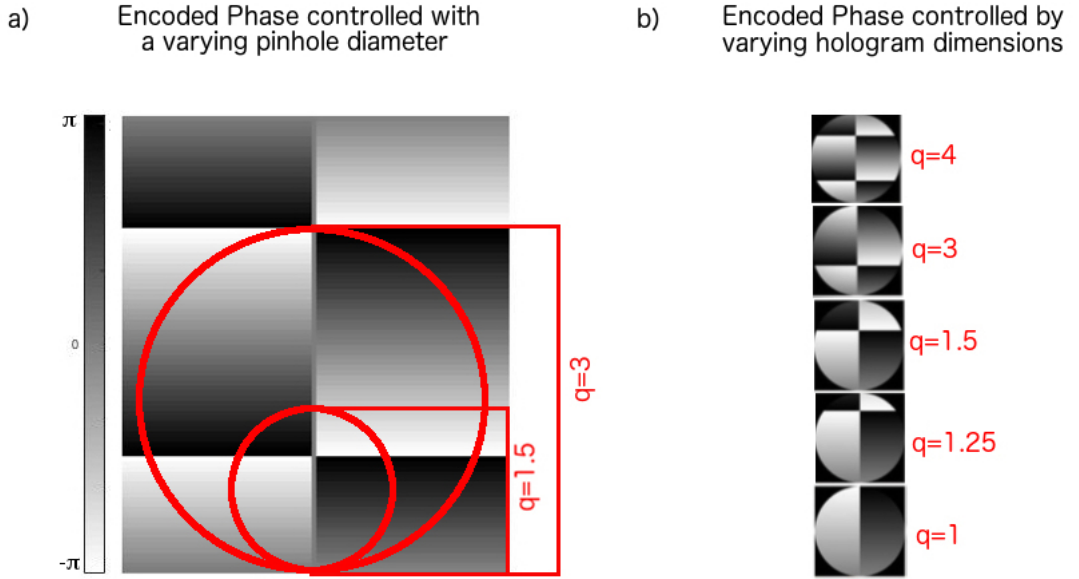


FIGURE 4.3: Comparison between classical and quantum hologram generation (original images can be found in the supplement materials of [19]). The images show the profile encoded in the vortex transmitter as given by equation 4.1 for different singularity strengths. In particular, in (a) the singularity strength (q) is controlled by varying the diameter of the aperture while in (b) q is controlled by varying the phase gradient (β) of the hologram.

Quantum Spiral Spectrum

As the premise of our vortex generator is that it can impart on a light beam any value of OAM (including non integer values), it is important to demonstrate that this is also valid for entangled photons. This can be achieved by measuring the OAM spectrum of the correlated photon pairs. Experimentally, this is done by analysing the correlations between the signal and idler photon beams where one is made to interact with the proposed grating, while the phase of the other is modified with a more traditional fork grating.

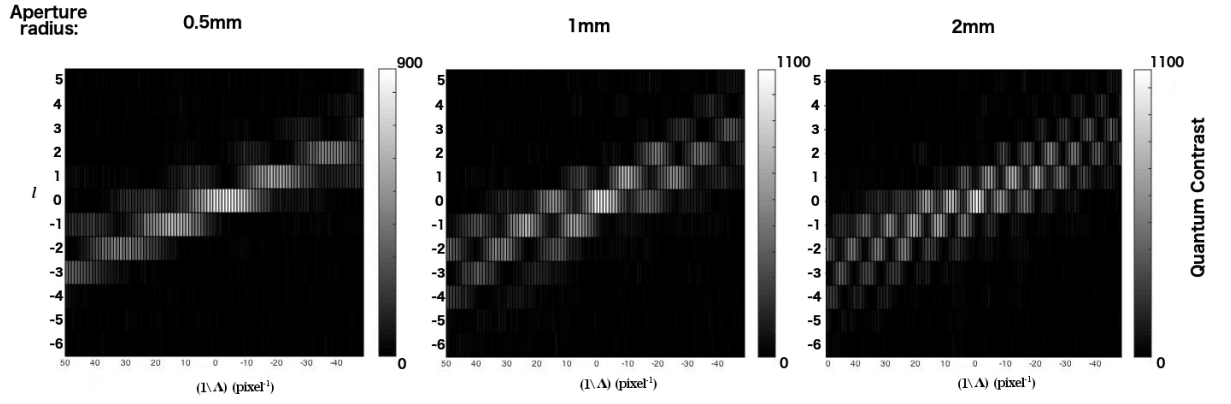


FIGURE 4.4: Spiral spectrum calculated for different aperture sizes. The spiral spectrum of the hologram is calculated at different aperture restrictions, where the 2mm aperture is equivalent to the beam size. All correlation matrices were generated by displaying a fork grating, for different values of l , on SLM_2 and the proposed grating, with grating period $1/\Lambda$ on SLM_1 (where Λ is measured in pixels). For the SLMs used in this experiment, the pixel pitch is $15\mu m$. It is important to note that by varying the grating period we are simply varying the phase gradient β which is responsible for the distance between two consecutive singularities (eq. 4.2). From the correlation matrices, it can be noticed that as the aperture gets smaller (i.e. the beam profile becomes more top-hat) the crosstalk between modes diminishes and the correlations become weaker.

It is important to highlight that the continuous OAM hologram used in this experiment was designed to be illuminated uniformly. However, the quantum experiment inherently uses Gaussian beams as the photons are collected by single mode fibres before reaching the coincidence system. It is possible, however, to approximate the Gaussian beam interacting with the hologram into a flat-topped illumination beam by introducing a restrictive aperture on the SLM (figure 4.1). The presence of the aperture will greatly decrease the cross-talk created when a non uniform beam interacts with our proposed hologram, albeit at the expense of the systems detection efficiency as fewer photons will reach the detectors (see figure 4.4). This reduction of photon flux can be problematic especially in the measurement of higher OAM modes where the correlation strength is weaker and therefore may not be distinguishable from background noise present in the system. For the quantum implementation of the vortex generator we therefore chose to encode the aperture on the spiniform phase

with a diameter of 0.6 mm. Furthermore, similarly to the experiment described in chapter 3, we also chose to express our correlation matrices as a function of the quantum contrast (QC) measured in order to reduce the effects of accidentals in our system.

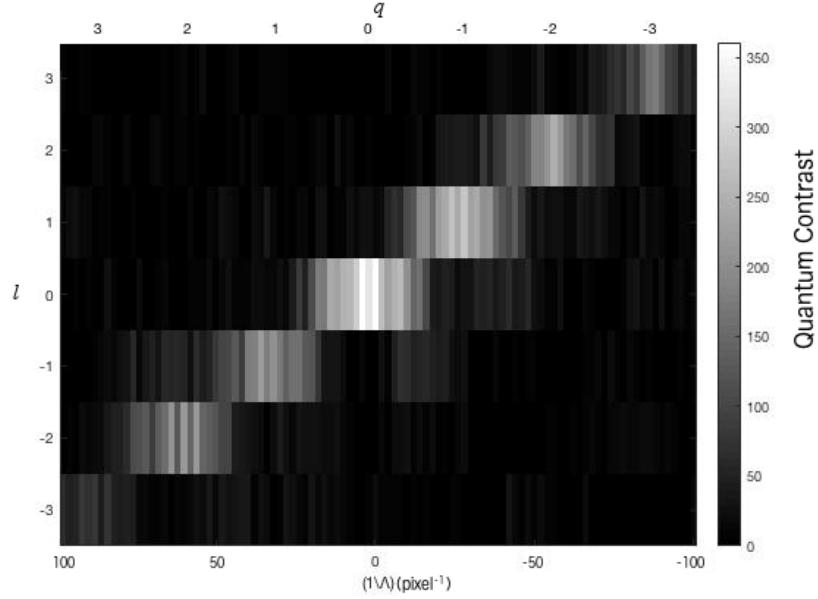


FIGURE 4.5: Quantum spiral spectrum of the spiniform phase [19]. We tested the spiniform phase with the set-up shown in figure 4.1. In particular, the correlation matrix was generated by displaying a fork grating, for different values of l , on SLM_2 and the proposed grating, with grating period $1/\Lambda$, on SLM_1 . The singularity strength (q) corresponding to the different values of $1/\Lambda$ is also shown.

We therefore calculated the correlation matrix between the entangled photons that have interacted with the two SLMs (see fig. 4.5). This was done by displaying a fork grating with OAM value l on SLM_2 and the grating of the proposed vortex generator, with singularity strength q , on SLM_1 . As mentioned above, for this quantum experiment we choose to control the value of q generated by our proposed hologram by gradually varying the phase gradient (β) of the hologram. In particular, as β is directly proportional to the inverse value of the grating period Λ (see eq. 4.2), we choose to test the correlation between values of $-3 \leq l \leq 3$ and $-100 \leq 1/\Lambda \leq 100$ where Λ is the pitch of the grating on the SLM (in pixels). In our experimental system the SLM has a pixel pitch of $15\mu m$.

Furthermore, similarly to the quantum communication experiment described in the previous chapter, the feasibility of using the proposed vortex generator to manipulate OAM is also tested numerically. In particular, as the experimental set-up used is similar to that of chapter 3, all considerations previously made when designing the numerical model are equally valid, hence the same numerical model can also be implemented to calculate the quantum spiral spectra of the proposed vortex generator. Thus, the predicted correlation strength between a signal beam carrying a helical phase of l and an idler beam whose phase component is generated using the same hologram encoded on SLM_1 , can be calculated (see figure 4.6).

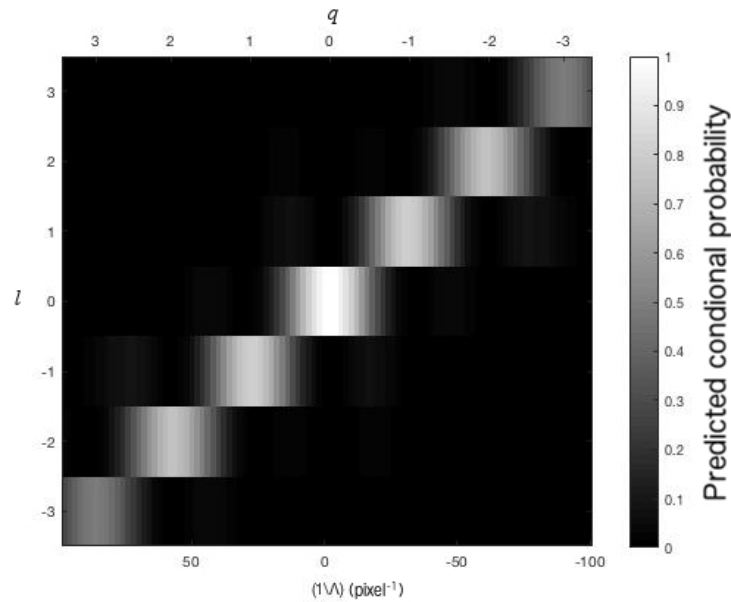


FIGURE 4.6: Simulated quantum spiral spectrum of the spiniform phase. A correlation matrix was generated by studying the overlap integral between the signal and idler beams where the signal beam is encoded with an OAM phase of l and the idler beam is encoded with a the spiniform phase singularity q .

As can easily be seen, both the measured (fig 4.5) and the simulated (fig. 4.6) results are in good agreement with each other with the measured correlation matrix displaying slightly more crosstalk than its counterpart. The presence of the added crosstalk is nevertheless consistent with our expectations as it can easily be explained by the limitations of the system as mentioned above. What is consistent in both the

experimental and simulated result is the presence of a smooth spiral spectrum, hence demonstrating that our proposed vortex generator, when used together with a more traditional fork grating, is still able to measure the anti-correlated diagonal consistent with OAM conservation both for integer and non integer values of q . This result thus allows us to conclude that our proposed vortex generator can be used at a quantum level to generate and manipulate OAM modes in the single-photon level.

Quantum Correlation

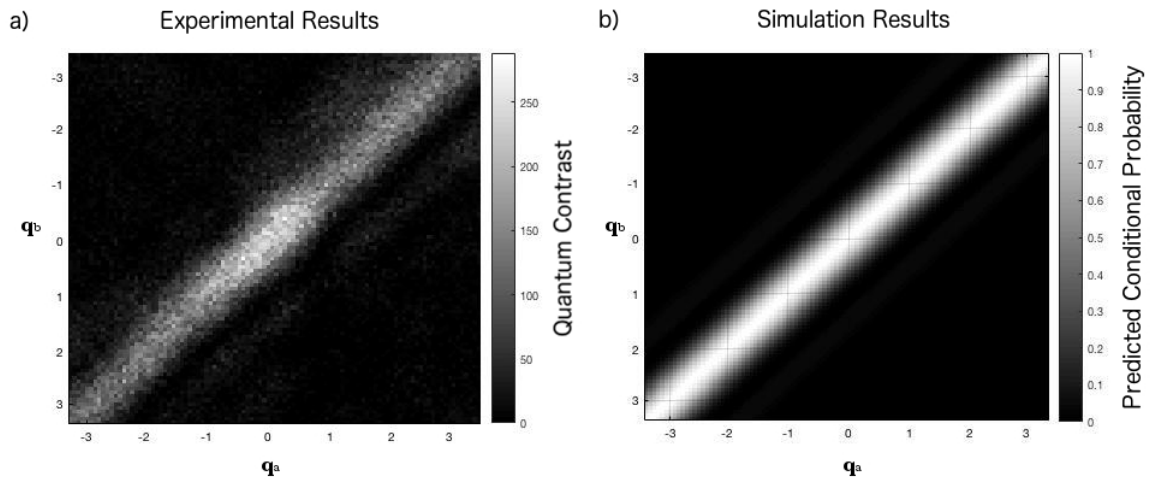


FIGURE 4.7: Quantum correlation matrix for the proposed vortex generator [19]. In order to test the feasibility of using the proposed vortex beam for a quantum communication system both SLM_1 and SLM_2 are used to impart phase singularities of q_A and q_B on the signal and idler beam accordingly. The joint detection of the vortex carrying signal and idler photons is therefore calculated and a correlation matrix constructed. As can be seen from the image above, a strong correlation is exhibited between the diagonal elements of the matrix with little to no crosstalk being exhibited for non diagonal elements.

Having shown that the spinform hologram is capable of imparting OAM on the correlated photons, the quantum coincidence between our vortex beams is also investigated. As for the quantum spiral spectrum, this is done both experimentally and numerically. In particular, similarly to the calculation of the vortex generator's spiral spectrum, the proposed hologram capacity to generate quantum coincidences is measured by calculating the correlation matrix between the entangled photons that

have interacted with the two SLMs. In this second experiment however, the grating displayed on both SLMs is the proposed vortex generator (fig. 4.1). This therefore allows for the measurement of the joint detection of the idler and signal photons carrying phase singularities of q_A and q_B respectively (fig. 4.7a). It is important to note that, as for the previous test, we choose to control the value of q generated by our proposed hologram by gradually varying $1/\Lambda$, hence measuring the joint detection of not only integer values of q but also non integer values inbetween. Furthermore, as previously mentioned, the quantum coincidence between the vortex beams is also numerically calculated. In particular, similarly to the numerical calculation of the quantum spiral spectrum, the predicted correlation strength between the vortex beam q_A and q_B is calculated by simply measuring the overlap integral between the two modes (fig. 4.7b).

Figure 4.7 displays the results for both the numerical and experimental measurements. As can be easily seen from fig 4.7, both the modelling data and experimental data exhibit very similar trends. In particular, in both cases, a strong correlation is exhibited between the diagonal elements of the matrix, correlation that rapidly dissipates the further the measurement is from the matrix diagonal. The presence of this clear diagonal correlation between the two photons, with little to no crosstalk being exhibited for non diagonal elements demonstrated the feasibility of using the proposed vortex beam for a quantum communication system.

It is important to note that, while a clear diagonal is present in the correlation matrix, this ‘‘correlation diagonal’’ has a full width at half maximum (FWHM) of about 0.9. This therefore implies that, when the vortex generator is applied in a quantum communication system, vortex beams with discrete q are preferred to avoid the strong crosstalk between two neighbouring states. The presence of this crosstalk can be easily understood as neighbouring non integer q possess a significant overlap in their spiral spectra.

4.4 Conclusion

In this chapter we have demonstrated for the first time a technique capable of generating optical beams that possess continuous OAM. In particular we have shown that the proposed mechanism is valid for the generation and manipulation of OAM modes at a single-photon level. The unique ability of the proposed vortex generator to smoothly transition from one OAM value to the next, can be therefore applied in the investigation of super-position states of OAM in quantum physics.

Furthermore, we have also shown that when applied to a quantum communication system, the proposed vortex is able to generate a smooth diagonal correlation matrix, therefore demonstrating the applicability of this method for quantum communications.

Finally, it is important to point out that this is the first analog method proposed for the generation of OAM states and therefore possible applications for this mechanism are still to be fully explored.

Chapter 5

Coherent Absorption of N00N States

5.1 Introduction

So far we have discussed different techniques to enhance the quantity of information that can be transmitted in a quantum communication system. In particular, we have both, compared the stability of modal bases in the presence of a non-ideal communication system (chapter 3), and proposed new techniques of imparting information on photons (chapter 4). However, even though we have demonstrated through our quantum correlation set-up that the methods proposed can be used for quantum communication, it is important to note that they are not exclusive to the quantum world but can also be applied to all classical communication (albeit without the added benefits that come when utilising entangled photons). On the other hand, an effect unique to the quantum world that is both the basis for many quantum protocols and fundamental in the creation of quantum logical gates is the Hong-Ou-Mandel (HOM) effect [59, 92–94].

The HOM experiment represents one of the simplest ways to test the degree of indistinguishability of two photons. This two-photon interference effect is unique in both the straightforwardness of its physics and geometry, and for the variety of quantum applications it is employed in, some examples being: phase metrology, quantum lithography, quantum state preparation, and as previously mentioned, quantum computing and quantum communication [23, 59, 95–97]. In particular, most of the quantum applications mentioned rely on the ability of HOM interferometers to generate maximally entangled two-photon quantum states known as $N00N$ states [97]. These two-photon superposition states have a high phase sensitivity which makes them ideal for applications in super-resolution experiments. More importantly for the scope of this chapter, the ability to generate multi-photon quantum-states is crucial for the generation of quantum computing schemes as a large number of quantum gates require the interaction between two or more qubits, where we use the term ‘qubits’ to distinguish the quantum bit from its classical counterpart. The different nomenclature is necessary as the classical basic information unit ‘bit’ can only have the discrete values of zero or one, while its quantum equivalent can have the discrete values of zero, one, or any superposition of the two. One such category of two-qubit gates is the controlled-unitary (CU) gates where one of the photons in the superposition is known as the control bit and the second photon is known as the target bit. In particular, in a CU gate, the state of the control bit is used to determine if the unitary operator in question should be applied on the target bit or if the target bit should be left unchanged [1]. A quite useful example of a CU gate is the $CNOT$ of which the output state is similar to that of the classical XOR gate. In particular, in a $CNOT$ gate if the state of the control bit (C) is $|0\rangle$ the outputted state of the target bit (T) is left unchanged, while, if the state of the control bit is $|1\rangle$, the outputted state of the target bit (T) is flipped i.e. from $|0\rangle$ to $|1\rangle$ or from $|1\rangle$ to $|0\rangle$ (fig. 5.1).

The importance of being able to generate CU gates for quantum computing becomes

Before		After	
C	T	C	T
$ 0\rangle$	$ 0\rangle$	$ 0\rangle$	$ 0\rangle$
$ 0\rangle$	$ 1\rangle$	$ 0\rangle$	$ 1\rangle$
$ 1\rangle$	$ 0\rangle$	$ 1\rangle$	$ 1\rangle$
$ 1\rangle$	$ 1\rangle$	$ 1\rangle$	$ 0\rangle$

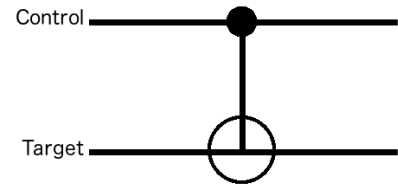


FIGURE 5.1: CNOT gate. The effect of the CNOT gate on the computational basis states is illustrated above, where C is the control bit and T is the target bit. A schematic representation of the gate is also shown [1].

apparent when one considers that any multi-qubit unitary transformation can be performed by simply combining single-qubit gates and a combination of universal two-qubit gates, the *CNOT* gate being a prominent example of such gates [1]. Equally important to the generation of multi-photon superposition states for the future of quantum computing with linear quantum optics, is the deterministic control of the multi-photons i.e. finding ways to implement the unitary transformations on the photons. Experimentally this is not trivial as photons are known to act as non-interactive particles, a condition that has great advantages (i.e. photons are potentially free from decoherence), however, this creates major problems in the application of quantum gates where interaction between the photons is essential. Different techniques have been proposed to overcome this difficulty, the most common being the use of nonlinear effects, like the optical Kerr-effect, to alter the environment in which the photons are propagating and induce a photon-photon interaction. Nevertheless all techniques considered for the implementation of linear optical quantum computers bring their own challenges, the presence of high losses and the hardship in scalability of the techniques being some examples. An extensive review of the different techniques and their limitations can be found in Kok et al.'s review: *Linear optical quantum computing* [98].

A promising field of research that could bring a solution to this problem is the newly discovered process of Coherent Perfect Absorption (CPA), first proposed in 2010 by Chang et al. [99]. CPA was proposed as the time-reversal counterpart to the laser

emission process, the set-up being similar to that of a laser optical cavity. Hence, in order to turn the classical laser into the proposed anti-laser, two things were necessary: that the gain medium inside the resonator cavity absorbs light at specific frequencies instead of emitting it and, that two counter-propagating coherent light beams are injected into the cavity. The feasibility of this process was demonstrated experimentally by the same group a year after its proposal by using a silicon wafer as the absorbing medium [100]. In this experiment, they were able to show that, by controlling the relative phase between the two counter-propagating beams entering the cavity, it was possible to either transmit or coherently absorb all of the incoming light as a result of the coherent interaction of the two light fields. More interesting for future applications in quantum optics was the realisation in 2012 that CPA can also occur in structures that have subwavelength thickness, as long as careful attention is placed on the position of the structure [101]. In particular, light will either be strongly absorbed or pass without loss depending if the film structure is placed on the antinode or node of the standing wave [101]. It is important to point out that the proportion of light absorbed by the thin film in a single pass is directly linked to the absorption property of the material used i.e. 100% coherent absorption can only be achieved if the thin film is 50% absorbant [102]. An example of a material that can be employed to generate this kind of thin film structure due to its absorption properties is graphene. In particular, it was shown that an unstructured multilayer graphene film could be used to modulate the imputed light with 80% efficiency [103]. Most recently, a major step towards the implementation of CPA for quantum systems was made when the applicability of this method was demonstrated at the single photon regime. In their experiment, Rogers et al. demonstrated that a single photon can be deterministically coupled to a plasmonic mode of a metamaterial [104]. They also showed that this conclusion is not unique to metamaterials but can also be achieved with a multilayer graphene sample.

In this chapter we discuss an experiment which builds on this work, and investigates two-photon N00N state coherent absorption in a multilayer graphene film. We show that by controlling the input phase of the photons, we can selectively choose if a single photon is deterministically absorbed or if the photon number is conserved in a combination of 2-photon output states [15]. Importantly, this is the first experiment that demonstrates how CPA can be used to deterministically control two-photon superposition states and consequently be a good asset in the generation of quantum gates.

5.1.1 Contributions

The work discussed in this chapter was carried out as part of a collaborative effort between members of multiple universities. In particular, the experimental set-up and data collection was performed by myself in the research lab at the *University of Glasgow*. The performed analysis was done by our collaborators in Prof. Faccio's group at *Heriot-Watt University* and the theoretical background for the paper was provided by Prof. Jeffers at the *University of Strathclyde*. As part of the collaboration, I was therefore responsible for setting up the HOM interferometer used as the source of the N00N states, which I did under the supervision of Dr Romero, postdoc in the group where I worked. I was also responsible for setting up, optimising and collecting data from the full Mach-Zehnder interferometer used in the experiment. This was done with the help of Drs Rogers and Lyons from Prof. Faccio's group. The output of this work is now published in *Physical Review Letters* [15].

5.2 The Hong-Ou-Mandel experiment

The goal of the experiment discussed in this chapter is to demonstrate that CPA can be used to coherently absorb a two-photon $N00N$ state. This is achieved through the use of a Mach-Zehnder interferometer (MZI) where the first beam splitter (BS_1) generates the two-photon $N00N$ states, and the second beam splitter (BS_2) performs the coherent absorption (fig. 5.7). More specifically, the $N00N$ states used in this experiment are generated through a HOM interference effect.

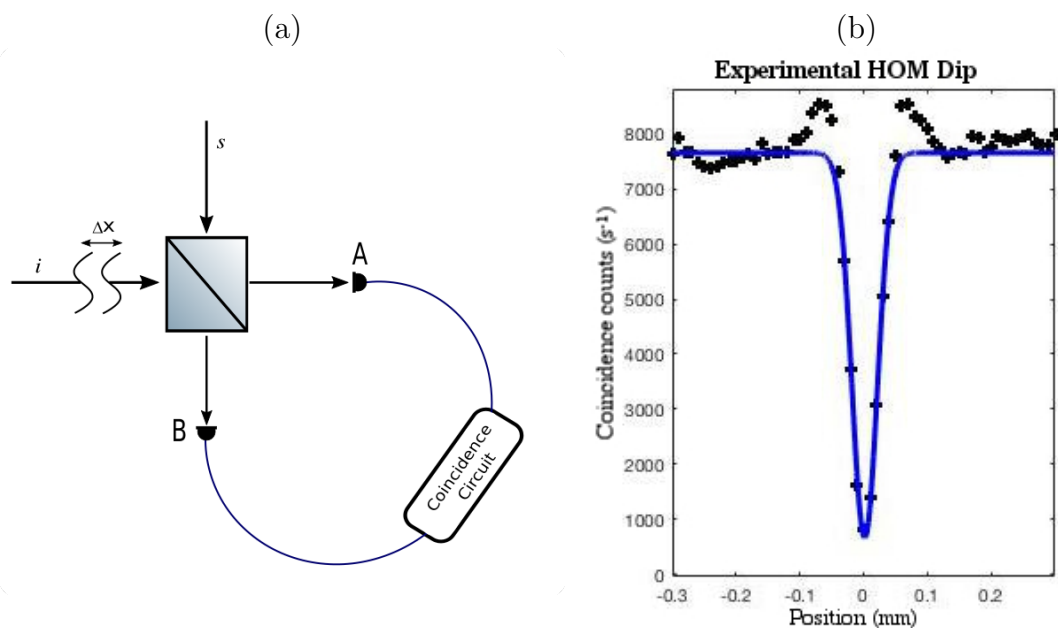


FIGURE 5.2: HOM interferometer. a) Schematic set up for a HOM experiment. The signal (s) and idler (i) photons are made to converge onto the input ports of the beam splitter and then collected by the detectors A and B at each of the outputs of the beam splitter. The two detectors are then checked for coincidences. b) Experimental HOM dip data taken for the $N00N$ experiment [15]. The graph shows the relationship linking the coincidence counts between the detectors measured in a 1 second time period (i.e. the coincidence rate) and the path length delay controlled using a translation stage. By moving the stage the path length, Δx of one of the photons changes in correlation to the other. When the optical path difference between the photons is zero, a dip in the coincidence rate occurs.

Proposed for the first time by Chung Ki Hong, Zhe Yu Ou & Leonard Mandel the HOM interferometer is simply based on the physical principle of two-photon interference [105]. This was accomplished using a simple layout consisting of very few components: a pump laser and nonlinear crystal for generating entangled-photon pairs

by SPDC, a lossless beam splitter and two photon detectors which are connected to a coincidence circuit. In this set-up, the two identical photons are separately (i.e. at different times) made to converge onto opposite input ports of the beam splitter and the resulting reflected and transmitted photons are collected by detectors placed at the two outputs (fig. 5.2a). It can easily be shown that, when two photons interact with a lossless 50:50 beam splitter, four equally probable outcomes exists for the imputed photons (fig. 5.3): 1) both are transmitted, 2) both are reflected, 3) the first is reflected while the other is transmitted, 4) the first one is transmitted while the other is reflected [20]. Hence, the total two-photon quantum state ($|\Psi_{total}\rangle$) at the detectors is the superposition of all four possible outcomes, half of which will generate coincidence counts as one of the photons will reach detector A and the other detector B.

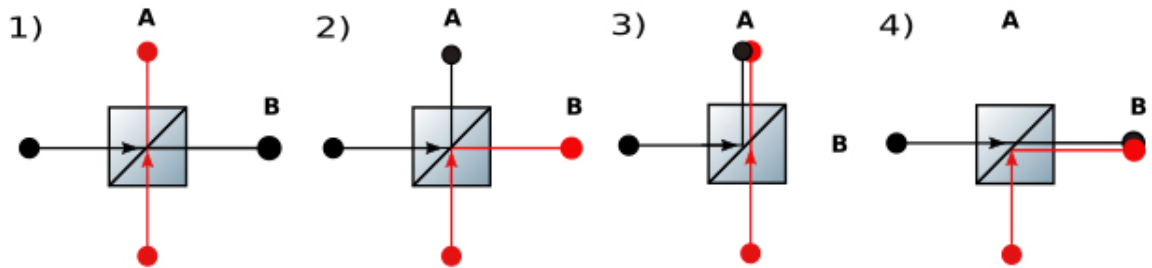


FIGURE 5.3: Outputs of a HOM interferometer. In this figure, the four outputs that are generated when two photons enter a beam splitter are depicted. In particular 1) shows both photons being transmitted, i.e. $|\Psi_1\rangle = |1_a, 1_b\rangle$. 2) shows both photons being reflected, i.e. $|\Psi_2\rangle = |1_a, 1_b\rangle$. 3) shows the first photon being reflected while the other photon being transmitted, $|\Psi_3\rangle = |2_a, 0_b\rangle$. Finally, 4) shows the first photon being transmitted while the second photon being reflected, i.e $|\Psi_4\rangle = |0_a, 2_b\rangle$.

On the other hand, if we consider the case in which the two photons are completely indistinguishable (i.e. photons that have the same path length, polarisation, spatial and momentum modes) the outcome of the interference is no longer the one described above. This is due to the fact that the outcomes that allow for photons to reach both the detectors at the output ports (i.e. parts 1 and 2 of fig. 5.3) become indistinguishable and undergo destructive interference [20]. This equates experimentally to

a disappearance of coincidence counts as both photons will reach either one of the two detectors but never both (i.e. parts 3 and 4 of fig. 5.3). The experiment carried out by Hong, Ou, and Mandel demonstrated this effect for the first time. In particular, they chose to consider the relative path delays between the two photons as the distinguishable property (fig. 5.2). It must also be noted that around the time that the HOM paper was published a separate independent experiment by Shih and Alley also demonstrated this same effect but instead of showing the effect in the temporal domain, they controlled the distinguishability of the photons by controlling the relative polarisation of the photon pair [106].

From a mathematical perspective this effect can be explained by calculating the total two-photon quantum state ($|\Psi_{total}\rangle\rangle$) at the detectors. As we have previously noted, the resulting quantum state generated by two entangled photons interacting with a 50:50 beam splitter can be written as the superposition of all four equally probable outcomes, i.e.:

$$|\Psi\rangle = p(e^{\phi_1} |\Psi_1\rangle + e^{\phi_2} |\Psi_2\rangle + e^{\phi_3} |\Psi_3\rangle + e^{\phi_4} |\Psi_4\rangle), \quad (5.1)$$

where p is the probability of the outcome (in the case of a 50% transmissive/reflective beam splitter, this value is equal to 25%), and the $|\Psi_i\rangle$ are the wave-functions for the four outcomes. In particular, if we adopt the convention $|\Psi_i\rangle = |N_a, M_b\rangle$ where N_a represents the number of photons exiting the beam splitter toward the output with detector A and M_b the number of photons at the output with detector B, we can write the four superposition states in fig. 5.3 as: $|\Psi_1\rangle = |1_a, 1_b\rangle$, $|\Psi_2\rangle = |1_a, 1_b\rangle$, $|\Psi_3\rangle = |2_a, 0_b\rangle$ and $|\Psi_4\rangle = |0_a, 2_b\rangle$. Furthermore, in the analysis, we have to consider the convention that exists by which any photon that gets reflected by the bottom half of a beam splitter acquires a π -phase shift [20]. This effect is a characteristic of

all beam splitters indiscriminately as it guarantees the conservation of energy of the system. We can therefore rewrite equation 5.1 as:

$$|\Psi_{total}\rangle = p(|2_a, 0_b\rangle - |0_a, 2_b\rangle + |1_a, 1_b\rangle - |1_a, 1_b\rangle). \quad (5.2)$$

Hence, if the two photons are indistinguishable then $|\Psi_1\rangle$ and $|\Psi_2\rangle$ will be equal to each other and therefore cancel out. Consequently, the equation for the total two-photon quantum state at the detectors can be simply rewritten as:

$$|\Psi_{total}\rangle = \frac{1}{\sqrt{2}}(|2_a, 0_b\rangle - |0_a, 2_b\rangle). \quad (5.3)$$

This two-photon quantum state output is known as N00N state where N is used to represent the number of photons in the output superposition state of the interference -i.e. $|N, 0\rangle - |0, N\rangle$.

5.3 Graphene as a lossy beam splitter

Having described the process behind the creation of the N00N states, I will give a brief summary on the mechanism behind the second half of our experimental set-up, i.e the use of graphene as a coherent perfect absorber (CPA). It is important to note, that this section is based on the work of our collaborator Prof. Jeffers who provided the theoretical background for the paper. This summary is hence in no way meant to be extensive. A more in-depth analysis of the working of a lossy beam splitter on superposition states can be found in “*Interference and the lossless lossy beam splitter*” by Jeffers [107]. Furthermore a good summary of the history, mathematical background and application of coherent perfect absorbers can also be found in Dr Lyons’s dissertation work [23].

To apply a thin layer coherent perfect absorber in an interferometer (in our case of our experiment a 50% absorbing graphene sample) it is first essential to understand how light interacts with the sample. It is therefore worth noting that a thin layer CPA is not very dissimilar from a traditional beam splitter like the one whose properties are described in the previous section. In particular, a lossless beam splitter is defined as a four-port device that superposes two incident or input fields to produce two output fields. This can be in the form of a cube beam splitter, where the two incident beams are at right angles to each other (see fig 5.4(1)) or it can be in the form of a partially reflecting film where the two beams are incident on the film at normal angles (fig 5.4(2)) [108]. Nevertheless, the geometry of the beam splitter does not effect the properties of the device and both a cube beam splitter and the thin film version can be represented by the same mathematical equations.

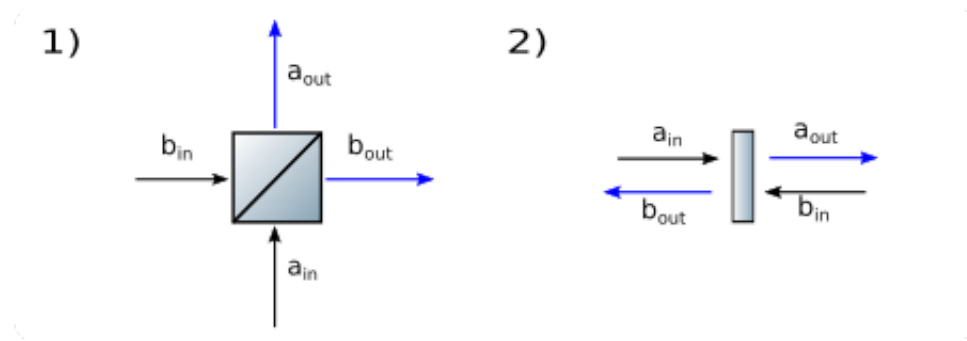


FIGURE 5.4: Schematic representations of beam splitters [108]. In both the diagrams two independent incident modes, mode a_{in} and b_{in} , are made to converge onto opposite input ports of the beam splitters. In the device they will either be reflected or transmitted and will exit the device as modes a_{out} or b_{out} as seen in figure 5.3. Hence, both the (1) cube beam splitter and the (2) partially reflecting film can be described by the same mathematical model.

The similarities between a thin layer CPA and a partially reflecting film beam splitter are quite evident. In particular, both partially absorbing devices operate with light incident normally on both sides. Furthermore, they both relate two input ports to two output ports with the crucial difference that, while the thin film beam splitters are designed to conserve energy and therefore have no loss, a thin film CPA is by design chosen to absorb energy and thus have loss (fig. 5.5). Hence, the thin film

CPA can be considered a “lossy beam splitter” and be represented by the same mathematical equations which describe a lossless beam splitter with the addition of two noise operators which are required to compensate for the presence of absorbing forces (fig. 5.5.i) [107].

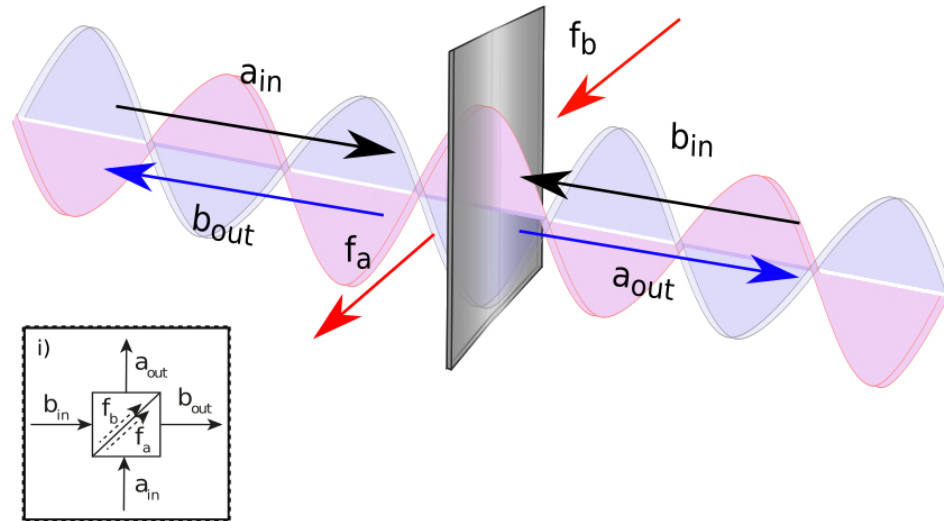


FIGURE 5.5: Schematic representation of a thin layer CPA (adapted from [104]). A thin layer coherent absorber can be modelled as a lossy beam splitter. In particular, similarly to the thin film beam splitter it has two input channels (a_{in} and b_{in}) and two output channels (a_{out} and b_{out}). On the other hand, it also poses two extra internal noise input and output channels (f_b and f_a) which are linked to the absorption process. When placed in a standing wave composed of two counter-propagating coherent beams the light will either be strongly absorbed or pass without loss depending if the film structure is placed on the antinode or node of the standing wave. Similarly, the insert shows the equivalent beam splitter representation as defined by Jeffers [107].

It is important to point out that, in order for the ‘lossy beam splitter’ to act as a coherent absorber it must be placed in a standing wave composed of two counter-propagating coherent beams. This is because, similarly to the HOM effect described above, the ability of a CPA to deterministically control the absorption of photons is directly linked to the interference of the photon wavefunctions inside the lossy beam splitter. This was mathematically demonstrated in Jeffers’ study of ‘lossy beam splitters’ for both the single photon regime and the multi-photon regime [107]. In

particular, in the case of a single photon regime, the coherent superposition of the single photon at the beam splitter can be defined as:

$$|1\rangle = \frac{1}{\sqrt{2}}(|1_a, 0_b\rangle) + e^{i\phi} |0_a, 1_b\rangle, \quad (5.4)$$

where a and b denote the input channels of the beam splitter and ϕ is the phase shift between them (fig. 5.5). From Jeffers' mathematical analysis it can easily be seen that, when studying the interaction between any coherent superposition state and a beam splitter device, there are two important cases to consider: $\phi = 0$ and $\phi = \pi$. The importance of these two cases becomes evident if one considers that, when imparted on a lossless beam splitter, these are the only cases that will pass through the device with no change to the number of photons in each mode. Hence, Jeffers choose to study the resulting interaction of this two single photon superposition with an ideal 50% absorbing, 25% reflective and 25% transmissive lossy beam splitter [107]. He therefore demonstrates that, in the case of $\phi = 0$ the lossy beam splitter will act in a similar way to its lossless counterpart and the superposition state will be transmitted through the device unchanged. More interestingly, is the case in which $\phi = \pi$, where the presence of the additional noise modes results in the coherent state being deterministically absorbed by the lossy beam beam splittersplitter. As previously mentioned, this result was experimentally demonstrated for the first time by Rogers et al. in his 2015 *Nature Communication* article [104].

TABLE 5.1: Quantum states for a lossless beam splitter. This table is based on an original table shown in our paper [15]. The table summarises the output photon states for various two-photon input states for a 50:50 beam splitter.

Input relation (θ)	Output
$ 2_+\rangle$	$ 1_a, 1_b\rangle$
$ 2_-\rangle$	$\mp 2_{\pm}\rangle$

Furthermore, in his study, Jeffers didn't limit himself to the single-photon regime but also explored coherent absorption in the case of a two photon interference -i.e. the N00N states mentioned in the previous section. This interaction can either be composed of two separate single states, hence producing the HOM effect previously mentioned, or more interestingly be composed of a superposition of two photons in one arm of the interferometer and zero in the other. Mathematically, this second case can be written as a coherent superposition of the two photon states at the beam splitter, defined as:

$$|2\rangle = \frac{1}{\sqrt{2}}(|2_a, 0_b\rangle) + e^{2i\phi} |0_a, 2_b\rangle). \quad (5.5)$$

As for the single photon regime, it can easily be shown that for this coherent superposition state, two important cases exist: $\phi = 0$ and $\phi = \pi/2$. Similarly to the single photon regime, when the superposition mode with $\phi = \pi/2$ interacts with a lossless beam splitter it will simply acquire a phase shift but otherwise transit through the device unchanged. On the other hand, the case in which $\phi = 0$ corresponds to the time reversal process of the HOM interference. In other words, the interaction of this two photon superposition state with a 50:50 beam splitter will result in the two bunched photons being deterministically split back into the two separate distinguishable photons. These results are summarized in the Table 5.1.

TABLE 5.2: Quantum states for a lossy beam splitter. This table is based on an original table shown in [107] and displays the output photon states generated when a two-photon input states interacts with a 50:25:25 lossy beam splitter. For the purpose of this table, $|\psi_2\rangle$ is defined as: $|\psi_2\rangle = (|1_a, 1_b\rangle \pm |2_+\rangle)/\sqrt{2}$

Input	Output
$ 2_+\rangle$	$\frac{1}{2} 0_a, 0_b\rangle\langle 0_a, 0_b \pm \frac{1}{2} \psi_2\rangle\langle\psi_2 $
$ 2_-\rangle$	$\mp 1_\pm\rangle$
$ 1_a, 1_b\rangle$	$\frac{1}{2} 0_a, 0_b\rangle\langle 0_a, 0_b + \frac{1}{2} \psi_2\rangle\langle\psi_2 $

More interestingly for our experiment is the interaction of these two photon coherent superpositions with a 50:25:25 lossy beam splitter. Similarly to the case 50:50 lossless beam splitter the interaction can either be composed of two separate single states ($|1_a, 1_b\rangle$) or be composed of a superposition of two photons in one arm of the interferometer and zero in the other (as defined by equation 5.5). However, the resulting output is no longer as simple as the lossless case but can be composed of a single photon state or a mixture of zero and two-photon states. These output states, derived in Prof. Jeffers 2000 article *Interference and the lossless lossy beam splitter* are summarised in Table 5.2 where for convenience the superposition state with $\phi = 0$ case is represented as $|2_+\rangle$ and the state with $\phi = \pi/2$ as $|2_-\rangle$ [107]. In particular, it was found that if the input state is $|2_+\rangle$, then either both photons survive interaction with the sample or both photons are absorbed. For the case in which there is no absorption, the output state ($|\psi_2\rangle$) can be described as an even superposition of a $|1_a, 1_b\rangle$ and a $|2_+\rangle$ state. Hence the total output of a $|2_+\rangle$ can be mathematically described as a statistical ensemble of the two photon state $|\psi_2\rangle$ and a state with no photons in the output ports. Interestingly, the same output can be achieved if two separate single photons interact with the lossy beam splitter (i.e. the case corresponding to the HOM interference in a lossless beam splitter) with the only difference that in this case the output photons have one less phase dependency [107]. In contrast, when the superposition state interacting with the lossy beam splitter is a $|2_-\rangle$ input state, then one photon of the pair is always absorbed while the other is transmitted. The output can therefore be described as superposition of one-photon states.

5.4 Coherent Absorption of N00N states

As described in the introduction, it has now been demonstrated both in the classical wave regime and in the single photon regime, that a thin multilayer graphene sample can be used efficiently as a coherent perfect absorber (CPA) [103, 104]. The experiment described in this chapter expands on this work and tests the ability of graphene to deterministically control photons in the multi-photon regime. It is important to point out that, despite the multi-photon case being theoretically demonstrated by Jeffers [107] this is the first known experimental demonstration of coherent perfect absorption for $N=2$ N00N states.

As previously mentioned, our experimental set-up is a MZI (shown in fig. 5.7) assembled by combining a HOM interferometer (schematically represented in 5.2) and a 50% absorbing multilayer graphene film (schematically represented in 5.5). In particular, as for the experiments in the previous chapters, the photons used in our experiment are generated through the SPDC process in which a 355 nm Nd:YAG laser is used to pump a type I BBO crystal. The residual pump beam from the SPDC process is then blocked through the use of a longpass filter, allowing only the 710nm down-converted signal and idler beams in the system. These two beams are then further filtered by a 10nm bandpass filter. The presence of this filter has a twofold purpose: it reduces the presence of unwanted noise photons in the system and it determines the width of the HOM dip as bandwidth and coherence length are inversely proportional to each other (see fig. 5.6). In particular, by filtering the entangled photons with the 10nm bandpass filter we increase the width of the HOM Dip from 0.02mm to 0.08mm therefore making the generation of N00N states by the HOM interferometer easier, and less susceptible to misalignment and temperature fluctuation.

The resulting filtered signal and idler photons are thus separated in the far field by

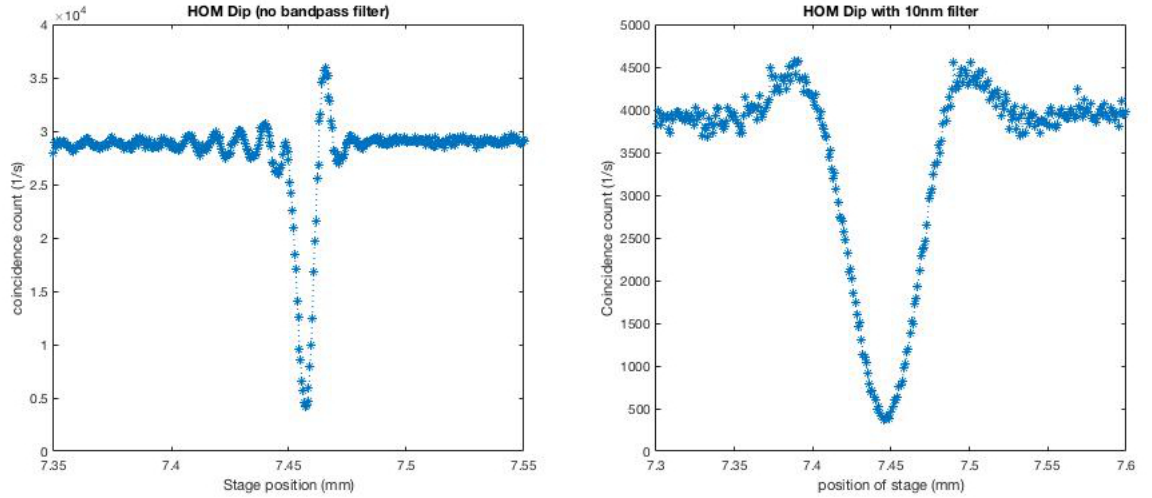


FIGURE 5.6: HOM Dips at different bandwidth. The two graphs show the HOM dip of coincidence counts measured by the detectors in a 1 second time period versus the relative delay between single-photons in our system. In particular the graph on the left shows different HOM dips calculated when no filter is inserted in the system, while the graph on the right shows different HOM dips calculated when a 10nm wide bandwidth filter is inserted in the system. As bandwidth and coherence length are Fourier counterparts, by filtering the entangled photons with a small transmission window bandpass filter, the width of the Dip can be increased i.e the Dip goes from being 0.02mm wide (with no filters) to 0.08 mm (with the 10nm filter present). The presence of the filters also determines the shape of the Dip. In particular, as the Fourier transfer of a top hat function is a *sinc* function, the presence of a sharp top hat filter generate the well define “bumps” artefacts that can be noticed on the side of the DIP generated with the 10nm filter.

a knife-edge prism mirror and coupled into single-mode polarisation-maintaining fibres which act as input ports to the HOM beam splitter (BS_1). As for the presence of the bandwidth filter, coupling into single-mode polarisation-maintaining fibres is also chosen to facilitate the experimental set-up, as it constrains the entangled photons which will interact with the HOM beam splitter to a single spatial mode, hence making the relative path delay between the two entangled photons their only distinguishable property. This delay can then be controlled by adjusting the position of one of the fibre couplers through the use of a computer activated stage, making it possible to measure the HOM interference dip (as previously shown in figure 5.2). In particular, in our experiment, we were able to measure a HOM dip with a depth of 89% (fig. 5.2 b). By carefully choosing the position of the motorised stage so as

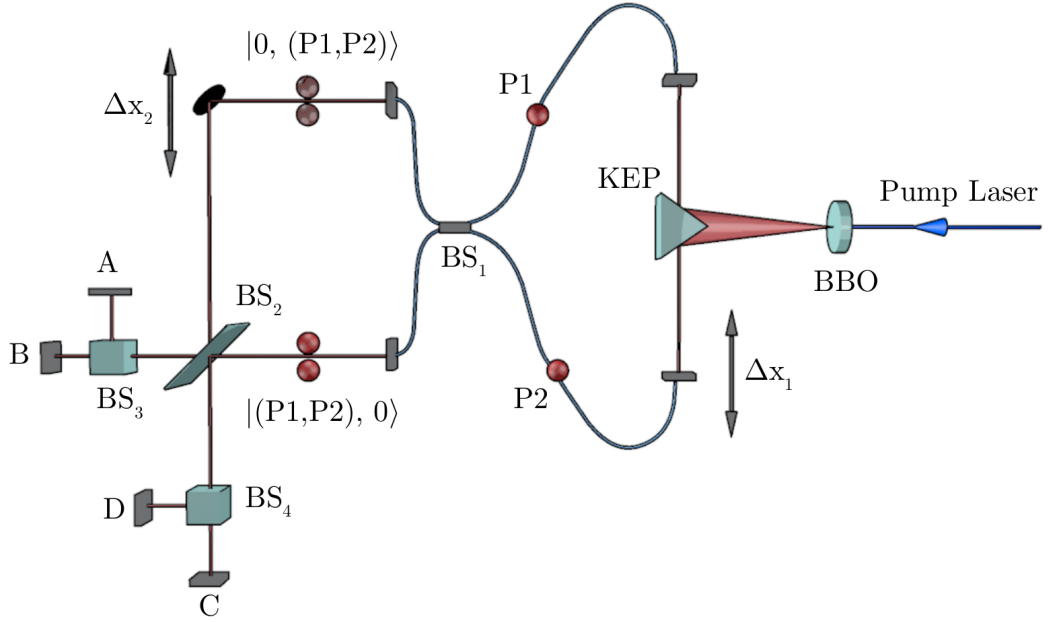


FIGURE 5.7: Experimental set-up [15]. Our experimental is a MZI assembled by combining a HOM interferometer and a 50% absorbing multilayer graphene film. The entangled photons are generated using SPDC, separated by a knife-edge prism (KEP) and coupled into the two single-mode polarisation-maintaining fibres which act as input ports to the HOM beam splitter (BS_1). In order to control the relative delay between the two photons (Δx_1), and consequently control the generation of the bunched photons states, one of the fibre couplers is placed on a motorised linear stage. The superposition state resulting from the HOM interference is then coupled out of the fibre beam splitter and directed to recombine at the second beam splitter (BS_2) through the use of an optical mirror in one of the interferometer arms. In the experiment, BS_2 can be a multilayer graphene film or a lossless 50:50 beam splitter. The phase ϕ of the superposition state in the MZI is controlled by using a piezo stage to vary the position of the mirror (Δx_2 in the figure). The output states from this interference are then split through the use of two 50:50 beam splitters (BS_3 and BS_4) and distributed over 4 single photon avalanche detectors (SPADs) connected to a PicoQuant Hydra Harp 400 with a temporal window of $\Delta\tau = 25\text{ns}$ allowing time-tagged events to be recorded.

to be at the minimum of the HOM interference dip we can therefore generate the bunched $N00N$ state required for this experiment and defined by equation 5.5. This superposition state is coupled out of the fibre beam splitter and into the second, open optical path, section of the MZI.

In this open path section of the MZI, the bunched photons are directed towards a beam splitter (BS_2) placed at the end of the interferometer at a 45° angle, though in this case the beam splitter is either a multilayer graphene film or a lossless 50:50

beam splitter film. As shown in the previous section, the relative phase delay (ϕ) between the incident beams at BS₂ plays an important role in determining the output of the device. We therefore choose to control this phase delay in the experiment by varying the position of the mirror present in one of the MZI arms with a piezo stage (Δx_2 in fig. 5.7). The output states from BS₂ are then themselves made to interact with two 50:50 lossless beam splitters, BS₃ and BS₄, placed at the two output ports of the interferometer resulting in four detection ports (A , B , C and D in fig. 5.7). The photons at these detection ports are subsequently collected by multimode fibres and directed toward four single photon avalanche detectors (SPADs). Finally the SPADs are themselves connected to a PicoQuant Hydra Harp 400 detection card, with a temporal window of $\Delta\tau = 25\text{ns}$, allowing time-tagged events to be recorded, therefore allowing us to measure coincidences across all four detection ports as a function of the interferometer phase. It is important to note that SPAD detectors are not able to distinguish between a single photon or a two photon state, hence the importance of BS₃ and BS₄. Any resulting two photon state output from BS₂ will probabilistically split at these beam splitters giving a coincidence count between AB or CD, and therefore providing us with an experimental way of measuring the presence of N00N state at the output of the interferometer.

5.5 Data Collection

As previously stated, the goal of this experiment is to demonstrate that a multi-layer graphene sample can be used to coherently absorb N00N states. Hence, after positioning the HOM delay stage (Δx_1) so as to be inside the HOM dip, a time tag measurement ($\Delta\tau=25\text{ns}$) of the single photons at the four detectors is taken as a function of the interferometer phase ($\Delta\phi$), where each time tag measurement is taken over an integration time of 1.2s. The coincidence counts for the detectors multiple

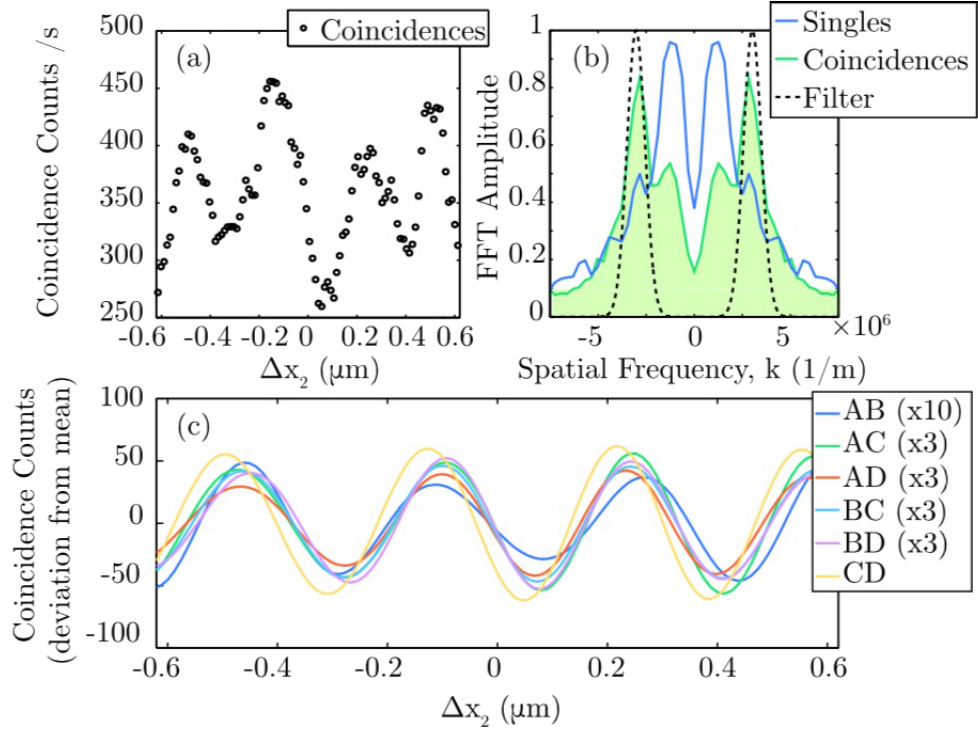


FIGURE 5.8: Experimental data from a lossy beamsplitter (figure from [15]). (a) Raw data showing the coincidence counts per second measured between detectors A and B as a function of MZI piezo stage. (b) Blue curve, Fourier transform of the *single* detector counts showing an oscillation at $k_1 = 1/\lambda$. Green shaded curve, Fourier transform of the *coincidence* counts showing a peak at frequency $k_2 = 2/\lambda$. Dashed black curve, gaussian fit to the peak at k_2 used to filter the raw data. (c) Fourier-filtered data for all six detection pairs as a function of mirror position. Due to the asymmetry of the sample, some of the output have lower visibility. In order to present the data on the same vertical scale, we multiplied AB by 10 and AC, AD, BC and BD by 3.

configurations (i.e. AB, AC, AD, BC, BD, CD) can therefore be calculated as a function of the position of the MZI piezo stage (Δx_2). An example of this coincidence measurement can be found in figure 5.8a.

Before discussing the data measured it must be noted that not all photons going through the HOM beam splitter will bunch. In particular, as our HOM has a depth of 89% (fig. 5.2), 11% of the entangled photons will not bunch and therefore will travel through the MZI and arrive at the graphene BS as two single states (i.e. in the form of $|1_a, 1_b\rangle$). Nevertheless, it is well known that a $N00N$ state will oscillate at twice the frequency of single photons. Hence the Fourier transformation of the data

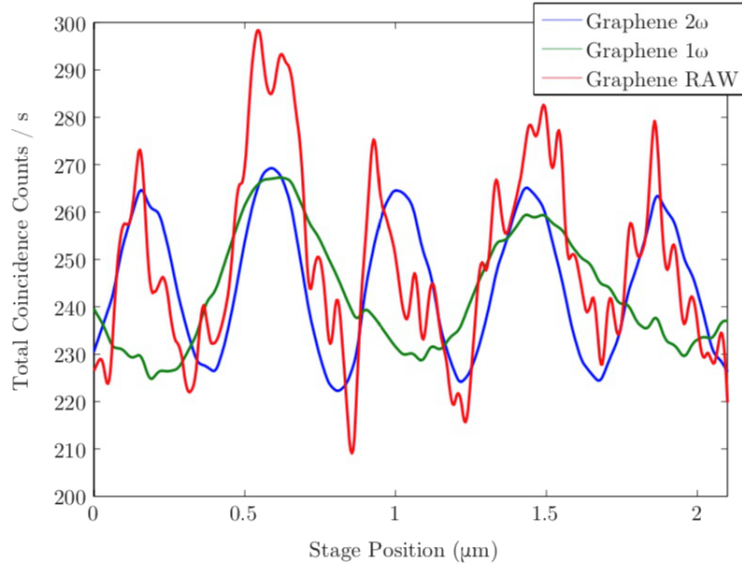


FIGURE 5.9: Fourier transform of RAW data. The graph shows in red, the coincidences counts vs interferometer mirror position for the graphene sample. Fourier filtering is then used to find the total coincidence rate at both $\lambda/2$ and $\lambda/4$ (figure originally generated by Dr. Roger.)

(fig. 5.8b) can be performed in order to distinguish the coincidence contributed by single photons and those contributed by $N00N$ states. In particular, in the frequency domain, the single photons will appear as a first harmonic frequency, while the $N00N$ states as a second harmonic frequency. A Gaussian-shaped filter (represented in fig. 5.8(b) by a black line) is then used to isolate the single photons and the $N00N$ photons, before Fourier transforming the data back into the plane of the stage position (see fig. 5.9). As we are interested in the interaction between $N00N$ photons and the lossy beam splitter, the $N00N$ component of the raw data is extracted for all the coincidence count detector pairing and plotted in figure (5.8c).

Finally, the graphene sample is then removed from the system and a glass 50:50 lossless beam splitter is inserted as the second beam splitter of the MZI (BS_2 in fig. 5.7). The full experiment is therefore repeated and the results are shown in fig. 5.10.

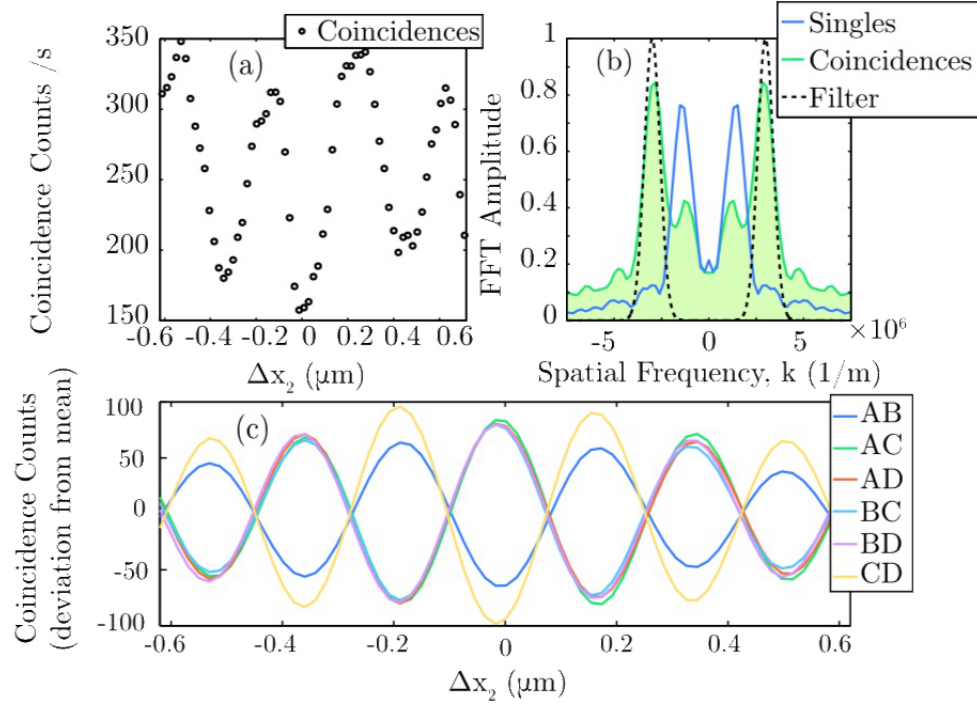


FIGURE 5.10: Lossless 50:50 beamsplitter (figure from [15]). (a) Raw experimental data showing the coincidence counts per second measured between detectors A and B as a function of interferometer mirror position. (b) Blue curve, Fourier transform of the *single* detector counts showing an oscillation peak at $k_1 = 1/\lambda$. Green shaded area curve, Fourier transform of the coincidence counts, showing a peak at frequency $k_2 = 2/\lambda$. Dashed black curve - gaussian fit to the peak at k_2 used to filter the raw data. (c) Fourier-filtered data for all six detection pairs as a function of mirror position.

5.6 Analysis of the results

As previously mentioned, BS_3 and BS_4 are inserted into the system to provide an experimental way to measure the presence of bunched photons at the output of the MZI. Hence, only the presence of coincidence between AB and CD will represent the presence of $N00N$ state at the output of the interferometer (i.e. the $|2\rangle$ term in tables 5.1 and 5.2). Accordingly, coincidence counts between detectors that are located at opposite output ports of the interferometer (AC, AD, BC, BD) will measure anti-bunched photon pairs (i.e. the $|1_a, 1_b\rangle$ term in tables 5.1 and 5.2).

Furthermore, the phase between these two categories of detection pairing (i.e. AB/CD and AC/AD/BC/BD) also plays an important role in the analysis of the interaction

of the N00N states with the lossy/lossless beam splitters. In particular, as can be seen from figure 5.8c and figure 5.10c, while in the lossy case there is near to no phase difference between coincidence counts of these detection pairings, in the case of the lossless beam splitter, the coincidence counts measured for the detector pairings are out of phase with each other. This is in agreement with the theoretical predictions discussed in section 5.3.

In particular, it can be seen from table 5.2, that for a lossy beam splitter, both the $|2\rangle$ and $|1_a, 1_b\rangle$ are outputs of the interaction of the graphene sample with the two-photon superposition state $|2_+\rangle$, while when a $|2_-\rangle$ N00N superposition state interacts with the lossy beamsplitter, only a single photon is outputted (hence no coincidence will be detected as only one detector will be hit). The slight phase mismatch between the coincidence counts measured by the detectors can be attributed to the imperfect phase between the two output fields of the graphene sample caused by the presence on one side of the sample of a very thin glass slide on which the graphene is layered.

Similarly, the outputs for the 50:50 lossless beam splitter case (figure 5.10c) are in agreement with the theory in section 5.3. In particular, it can be seen from table 5.1, that depending on whether the N00N superposition state arrive at the beam splitter in phase ($|2_+\rangle$) or out of phase ($|2_-\rangle$) the output will either be $|1_a, 1_b\rangle$ or $|2_\pm\rangle$. As we have previously mentioned $|1_a, 1_b\rangle$ corresponds to coincidence counts between the beam splitters AC/AD/BC/BD and $|2_\pm\rangle$ corresponds to coincidences between the AB/CD, hence a phase shift in the interferometer will simply translate to a π phase shift between the coincidence count rates at these detection pairs.

Finally, to reiterate the fact that in the case of a lossy beam splitter a coherent absorption of N00N states has taken place, the total number of coincidences measured by all detection pairs as a function of the interferometer path delay (Δx_2) is calculated.

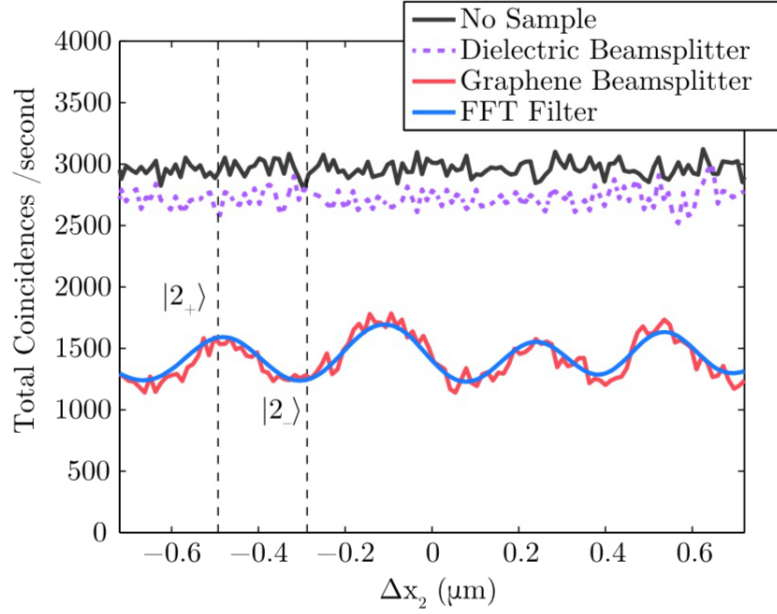


FIGURE 5.11: Comparison between the total measured two photon states (figure from [15]). The sum of coincidence counts for all six detection pairs as a function of interferometer mirror position is shown for (i) no sample, (ii) 50:50 lossless beamsplitter (dielectric BS) (iii) lossy graphene beamsplitter.

In summing the coincidence counts, it is important to take into consideration that 50% of the time two photons interact with BS_3 or BS_4 they will bunch together and therefore be recorded as a single coincidence by the detector. We take this into account in our sum by multiplying the coincidence detected by AB and CD by a factor of 2 (i.e. the total coincidence is given by $2AB + AC + AD + BC + BD + 2CD$). This calculation is conducted for the case in which: (i) no sample is present in the system; (ii) a 50:50 lossless beamsplitter is placed as BS_2 ; (iii) a lossy graphene sample is placed as BS_2 (fig. 5.11). From fig. 5.11, we can therefore conclude that while, as expected, there is no substantial difference in total coincidence counts between the case with no sample and a lossless beamsplitter present at BS_2 , when a lossy beamsplitter is placed as the second beam splitter of the MZI, the total number of coincidence rates oscillates as a function of the interferometer phase. This result is consistent with both the theory in 5.3 and with our previous analysis.

5.7 Conclusions

In this chapter we were therefore able to demonstrate the coherent absorption of NOON states through the use of a lossy beam splitter. This was performed by using a multilayer graphene sample as a CPA. Furthermore, since NOON states exhibit half of the period of a single photon state, by demonstrating the coherent absorption of NOON states, we have also demonstrated a potential way of isolating single and two-photon processes. As previously mentioned, the coherent control and absorption of qubits is essential for the generation of quantum gates. By demonstrating the ability of the CPA process to coherently control and absorb two-photon NOON states we therefore open the possibility for future applications in the field of quantum computing.

Chapter 6

Quantum Gyroscope

6.1 Introduction

The use of laser interferometers to study the Sagnac effect can be traced back to the Macek and Davis experiment in early 1963 [109]. In their experiment, they constructed the first ever ring laser gyroscope to detect the earth's rotation. It is important to point out that the sensitivity of optical gyroscopes is directly related to the cavity length of the system [110]. With the development of single-mode fibres, the opportunity therefore arose to significantly increase the sensitivity of optical gyroscopes by using these fibres as the propagating medium. In 1976 the first fibre optic gyroscopes (FOG) was therefore proposed by Vali and Shorthill [111]. Since then, both ring laser gyroscopes (RLG) and FOG have been used to study a variety of phenomena including acoustic fields [112], magnetic fields [113], as well as being proposed for the measurement of gravitational waves [114].

With the growing sophistication of the optical components the sensitivity and dynamic range of both RLG and FOG has greatly increased and gyroscopes are now found in a variety of fields and applications (see fig. 6.1); airplanes, space navigation

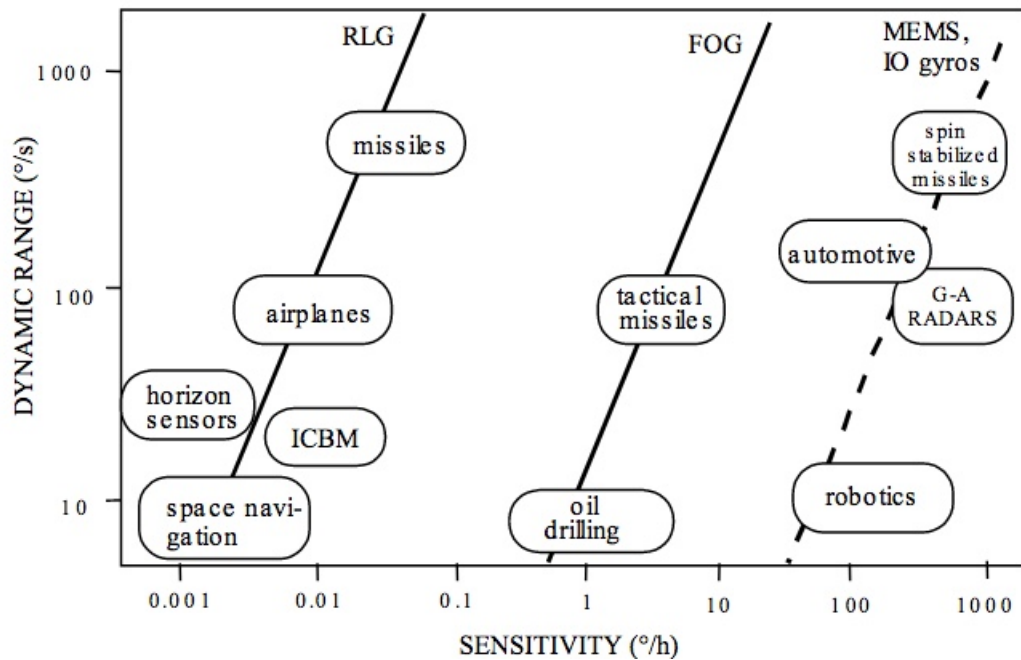


FIGURE 6.1: Dynamic range and sensitivity of the different types of gyroscope currently presented in the market (original image can be found in [110]).

and oil drilling being a few examples [110]. It must be pointed out that, the initial goal of FOG to create a system more sensitive than the RLG gyroscope did not come true as modern RLG can reach sensitivities of $0.001^\circ/\text{hour}$ vs the $0.1^\circ/\text{hour}$ of the FOG. Nevertheless, this sensitivity comes at the price of size and manufacturing cost. In particular, the sensitivity of RLG increases quadratically with the size of the cavity hence attempting to miniaturise the system simply leads to a loss in reliability of the apparatus [115]. In order to surpass the sensitivity of other forms of gyroscopes, RLG are constructed on large scales with a recent set-up covering an area of 834 m^2 [116]. On the other hand, due to the presence of very few optical components, the FOG gyroscope is not only cheaper to build but can easily be miniaturised, with recent prototypes being as small as 11.5 cubic inches [117]. It is important to note that the research in the development of new, more sensitive, gyroscope designs has also not deemed with time, with novel research being published as recently as May 2016 [118].

In any event, no matter if it is a RLG or FOG, all optical gyroscopes operate by measuring what is known as the Sagnac-effect. This relativistic effect relies on the interference of two counter-propagating waves traveling around a rotating platform. In particular, the rotation of the platform induces a change in path lengths between the counter-propagating light beams which will manifest as a phase difference between the two waves. By measuring this phase shift, optical gyroscopes are therefore able to measure the angular speed of the system in relation to the inertial system.

It is important to note the similarities between the configuration of the HOM interference (as described in section 5.2) and the Sagnac interference effect. In particular, both effects rely on the presence of a path difference between two interfering light beams. In the Sagnac interferometer this relativistic delay manifests itself as a phase shift ($\Delta\phi$) of the interference pattern at the detector plane. Similarly, in a HOM interferometer two indistinguishable entangled photons are made to interfere at a beam splitter resulting in destructive interference when the path length of the two photons are matched. Hence by controlling the path delay between the two entangled photons, a dip in coincidence can be measured at the detectors, resulting in scanning of what is known as the HOM dip. But while similar in configuration, the physics behind the working of these two experiment is quite different, the first being a well established special relativistic effect while the second being a well known test of quantum mechanics [105].

Interestingly, while both the fields of quantum mechanics and relativity are separately well established, the unification of the two is one of modern physics open problems. Traditionally, this problem has been approached by proposing theories that quantised gravity while retaining the foundational principles of quantum mechanics [119]. While an abundance of quantum gravity theories have now been proposed (string theory being one such example), being able to experimentally demonstrate the validity of one over the other has been challenging. In particular, in conventional quantum

gravity theories general relativistic effects are predicted to occur at the Plank scale which is tens of orders of magnitude away from current measurement sensitivities. The lack of experimental confirmation for any particular quantum gravity theory has lead to a recent theoretical shift in the way the unification of these two theories is tackled. In particular, an alternative approach has been suggested where the need to quantise gravity is called into question, but instead suggests that a unified theory should require the current framework of quantum theory to be modified i.e. suggesting that the unified theory be a “gravitize quantum theory” [119]. Quantum mechanical experiments that probe gravity can be divided into two categories, local and nonlocal. In particular, quantum mechanics experiments that are in the local category are proposed as a way to test special relativistic effects and noninertial effects in Minkowski spacetime, where the Riemann tensor corrections can be neglected. On the other hand nonlocal quantum mechanics experiments are proposed as a way to test probe general relativistic effects, where the result is directly related to the curvature of spacetime. It is important to note that, while very few experiments have been performed in the local category [17, 120], no nonlocal experiment has currently been experimentally realised. It is in this context that the experiment in this chapter is proposed. In particular, in this chapter, we performed a novel experiment in which we combine, in a single experiment, the relativistic Sagnac effect with a quantum mechanical HOM effect. This “quantum gyroscope” is a local quantum mechanic experiment where the behaviour of entangled photons in a noninertial reference frame is probed. As very few experiments exists testing quantum effects in non-inertial frame we proposed this experiment as a way to increase the general understanding of the interface between quantum mechanics and general relativity.

6.1.1 Contributions

The work discussed in this chapter was carried out as part of a collaborative effort between members of different research groups. In particular, the experiment was proposed by my supervisor Prof. Padgett. The design and construction of the experimental set-up was performed by myself with the help of my postdoc Dr. Gibson in the research lab at the *University of Glasgow*. The experiment's data collection and data analysis was also performed by myself. The output of this work has been submitted to *Physical Review Letters* and includes an extensive theoretical background provided by Dr. Toroš from the *University of Southampton* and Prof. Faccio formally from *Herriot Watt University* now at the *University of Glasgow*.

6.2 Sagnac effect

As mentioned in the introduction, the principle of a FOG gyroscope is based on the relativistic Sagnac effect [121]. The basic principles of this effect are therefore discussed in this section.

In particular, in the FOG interferometer, a laser generated light beam is split, through the use of a beam splitter, into two identical beams. These two beams are then coupled into opposite ends of single mode optical fibre, coiled in loops of radius R . After traveling through the fibre in counter-propagating directions, the two beams are then coupled out of the fibre and recombined at a detection plane, through the same beam splitter used to separate them (fig. 6.2). The whole system is itself mounted on a movable platform. This platform, is therefore made to rotate about an axis perpendicular to its surface, at an angular velocity of Ω radians per second. It is important to point out that, as can be seen from figure 6.3, this rotation plays an important role in the functionality of the system. In particular, during the time

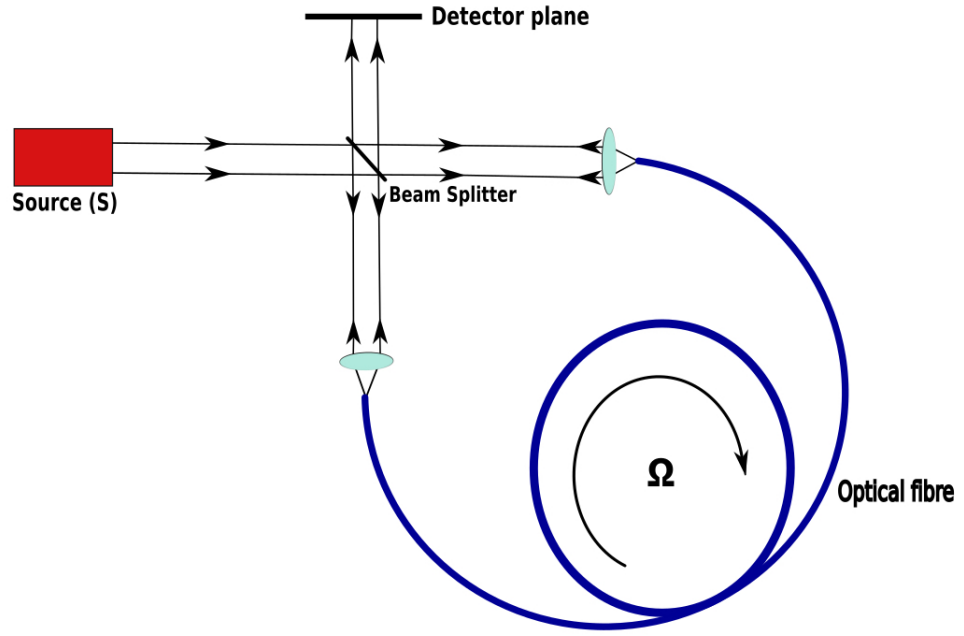


FIGURE 6.2: Classical design of a fibre Sagnac interferometer (original image can be found in [121]). A light source (S) generates a light beam is split through the use of a beam splitter, into two identical beams. These two beams are then coupled into opposite ends of single mode optical fibre. After traveling through the fibre in counter-propagating directions, the two beams are coupled out of the fibre and recombined at a detection plane, through the use of the original beam splitter. The whole system is then rotated at an angular velocity of Ω .

it takes for the two counter-propagating light beams to travel along the fibre path (Δt) the position of the input/output of the fibre will no longer be the same. In fact, one input coupler will have moved $\Delta l_+ = (\Omega * R * \Delta t_+)$ toward the propagating beam and the other coupler will have moved $\Delta l_- = (\Omega * R * \Delta t_-)$ away from the propagating beam. The overall path difference Δl induced by the rotation of the set-up can therefore be defined as:

$$\Delta l = \Delta l_+ + \Delta l_- = \Omega R (\Delta t_+ - \Delta t_-).$$

As previously mentioned, Δt is simply the time it takes for the light beams to travel along the fibre path L , which in the case of photons traveling in a vacuum is equal to: $\Delta t = L/c$. It is important to point out that the medium in which the photons

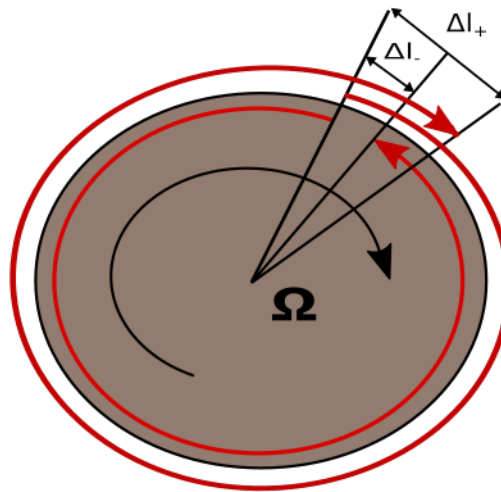


FIGURE 6.3: Principle of the Sagnac effect (original image can be found in [121]).
The phase shifts between two counter-propagating waves

travel is irrelevant to the derivation of the Sagnac equation, as any relative drag effect produced by the presence of a dielectric medium would be equally present in the clockwise and anticlockwise beams. Hence, it has been well documented in the literature that, modifying the equations to consider the drag effect will simply yield the same Sagnac expression that is calculated for photons traveling in a vacuum [121]. Also, since both counter-propagating light beams are identical, the fact that Δt_+ must be equal to $-\Delta t_-$ can easily be inferred. The overall path difference Δl can therefore be written as:

$$\Delta l = 2\Omega R\Delta t = \frac{2\Omega RL}{c}. \quad (6.2)$$

But, as described in the introduction to the chapter, the Sagnac interferometer measures the relativistic delay induced by the rotation through the measurement of the phase shift ($\Delta\phi$) of the counter-propagating waves at the detector plane. Hence, by

considering that the path and phase difference in an interferometer are related by the equation $\Delta x/\Delta\phi = \lambda/2\pi$, we can therefore rewrite equation 6.2 as:

$$\Delta\varphi = \frac{4\pi\Omega RL}{\lambda c}. \quad (6.3)$$

Equation 6.3 is therefore the Sagnac effect measured with a circular shape FOG interferometer of radius R and fibre length L .

It is important to note that the area inclosed inside the Sagnac interferometer loop does not necessarily need to be circular but can be any generic geometric form. In order to generalise equation 6.3 to an expression valid for any geometric form, we first point out that in the circular case, the length of the fibre can be re-expressed as a function of the number of turns needed to coil the full fibre path around the system i.e. $L = 2\pi RN$. Equation 6.3 therefore becomes:

$$\Delta\varphi = \frac{8\pi^2 R^2 \Omega N}{\lambda c}. \quad (6.4)$$

It is important to note that πR^2 in equation 6.4 is simply the circular area enclosed by the coiled fibres. Therefore, by replacing this part of the expression with a more general variable A we can obtain an expression of the phase shift which is independent of the geometric form of the system:

$$\Delta\varphi = \frac{8\pi\Omega NA}{\lambda c}. \quad (6.5)$$

Equation 6.5 is the standard formula for Sagnac effect and hence it is the one most commonly found in the literature.

6.3 HOM as a Sagnac interferometer

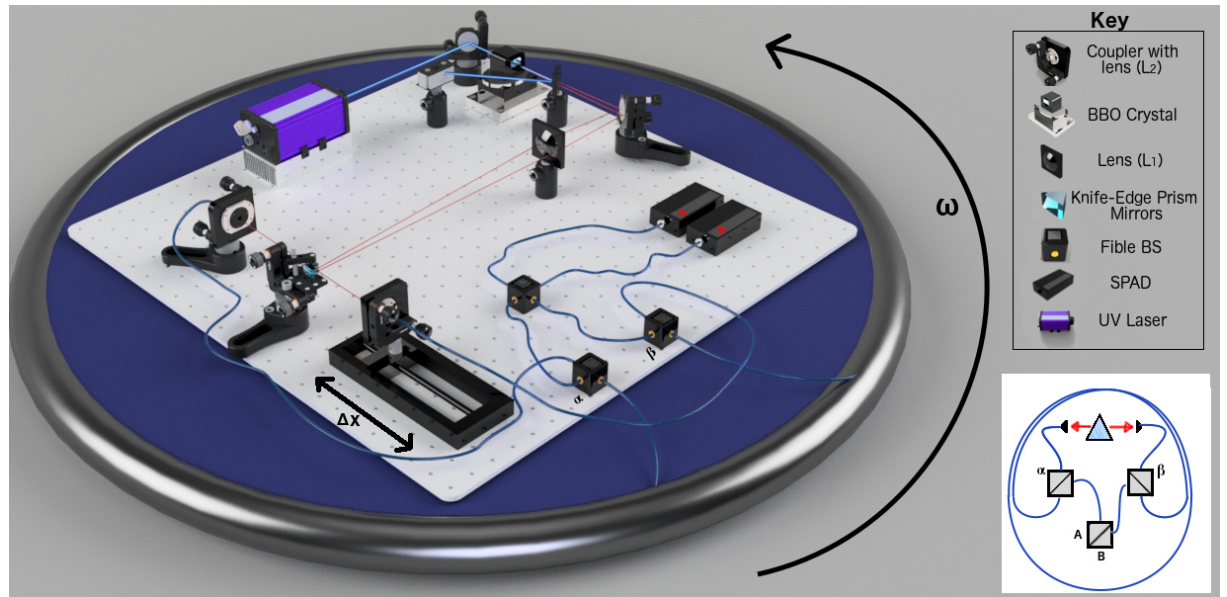


FIGURE 6.4: 3D representation of the HOM gyroscope. The experimental set-up is built on a circular rotating platform, of radius $R = 0.454m$, which can be made to rotate at a constant angular velocity Ω . On this set-up SPDC generated entangled photons are split at a KEP and coupled into single mode fibres. The photons are directed by BS α (in the case of the idler photon) and β (in the case of the signal photon) towards an $L=100m$ single mode fibre coiled in a loop around the outside of the table. After traveling through the fibre the photons will be redirected by the BS α and β towards the final beam splitter. The outputs of this beam splitter are then connected to SPAD detectors A and B.

As mentioned in the introduction, the goal of this experiment is that of testing, through a HOM interferometer in a non inertial frame, the role of relativity in quantum mechanics. A Sagnac interferometer is therefore built on a rotating platform, where the light traveling in the two arms of the interferometer are SPDC generated entangled photons (fig. 6.4). More specifically, a CW UV (355 nm) laser is used to pump a type I BBO crystal and generate the two correlated photons. The residual pump beam from the SPDC process is then reflected toward a beam blocker by a dichroic mirror allowing only the 710nm photons in the system. These entangled photons are directed toward a knife-edge prism (KEP) placed at the far field of the crystal, where the signal and idler beams are separated and coupled into single mode

polarisation maintaining fibres. Inside this fibre component of the interferometer, the signal and idler photons are made to travel clockwise and anticlockwise respectively through a 100m looped fibre located at the perimeter of the circular platform of radius $R = 0.454m$ (figures 6.4 and 6.5). After traveling through this fibre the photons are then recombined at a fibre beam splitter and the outputs from the beam splitter are collected by two single photon avalanche detectors (SPADs A and B) which are connected to a coincidence machine (a schematic representation of this can be seen in fig. 6.5).

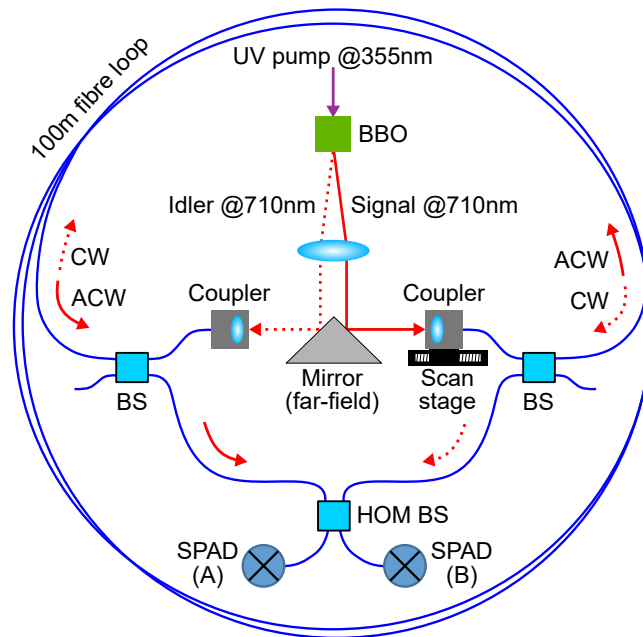


FIGURE 6.5: Schematic representation of the HOM interferometer on the rotating platform [122]. The generation of the signal and idler photons is shown together with the path they follow through the interferometer before interfering at the HOM beam splitter.

As comprehensively described in section 5.2, whenever two indistinguishable photons combine at the HOM beamsplitter, quantum interference dictates that they will bunch and therefore always exit from the same output port in an effect known as the HOM interference effect. This will manifest itself as a drop in coincidence counts detected by the system compared to the case in which the photons are distinguishable and therefore do not bunch. Its important to highlight that, similarly to the

experiment in chapter 5, careful consideration is taken to make the photons in the system completely indistinguishable therefore making the measurement of a HOM dip possible. For example, as for the NOON experiment, in the current set-up the choice of using single-mode polarisation-maintaining fibres is made as it constrains the entangled photons that will interact with the HOM beam-splitter to one single mode while also ensuring that their polarisation does not change while traveling through the fibre. Hence, similarly to the NOON experiment the only distinguishable property in this HOM set-up is the time of arrival of the photons at the beam-splitter. In the case of a non rotating system, this time delay can be controlled by generating a path difference between the signal and idler and photons through the use of a delay stage placed at one of the fibre couplers (fig. 6.5).

Finally, it must be noted that, as for all the sensitive experiments I undertook during my PhD, controlling the noise in the system plays an important role in being able to successfully operate the experiment. In particular, as we are interested in testing if a rotation of the experimental system induces a relative delay in the photons arrival, any noise effect that will create a change in path length in the system has to be suppressed. Different precautions were therefore taken in the construction and running of the experiment to control these noises. Specifically, as we are using pure silica fibres, these fibres can be susceptible to drift due to unwanted path-length variations caused by effects generated by the rotation of the system. Such effects may include temperature variations caused by air movement or the stretching of the fibres caused by the rotation generated centrifugal force. Hence, instead of using separate fibres for the clockwise and anticlockwise loops we set-up the experiment so both photons would travel through the same fibre. In order to do so, two additional beamsplitters were added to the system after the coupling optics (labeled α and β in figure 6.4). In particular the beam-splitter labeled α allows for the signal photons to enter the 100m long coiled fibre and travel through it in an anticlockwise direction

while, at the same time, redirecting the idler photons, having traveled in the clockwise direction, towards the HOM beam-splitter. Equally, the beam-splitter β sends the idler photons through the fibre towards beam-splitter α while redirecting the arriving signal photons to the HOM beam-splitter. It must be noted that while allowing us to only use one fibre for both the clockwise and anticlockwise paths this comes with a reduction in optical coupling efficiency.

As previously mentioned, the rotating set-up will be subjected to a noise component due to the presence of a centrifugal acceleration. It is important to note that this phenomena does not only affect the fibre, but also all mechanical components present on the system. However, while the Sagnac effect is sensitive to change in rotation (i.e. clockwise and anticlockwise will generate a result with opposite signs) the centrifugal force is not sensitive to the direction of rotation. We therefore can by-pass the existence of this noise by calculating our measurements as an average (in absolute value) between clockwise and anticlockwise rotation measurements (see fig. 6.6).

Experimental results and analysis

As mentioned above, in a classical Sagnac interferometer, rotation induces a phase shift between the clockwise and anticlockwise beams that is observed at the output of the interferometer. The question is whether the HOM dip undergoes a corresponding change. In particular, as the Sagnac effect is linearly dependent on the rotation speed (as demonstrated in section 6.2) we therefore performed our experiment for a range of rotation speeds of the system.

This can be done by performing a series of repetitive measurements for each speed in which the full HOM dip is scanned by the scanning stage present at the fibre coupling. This approach provides photon path delay measurements with a precision of the order of a micrometer, as both the stage precision and the stage repeatability,

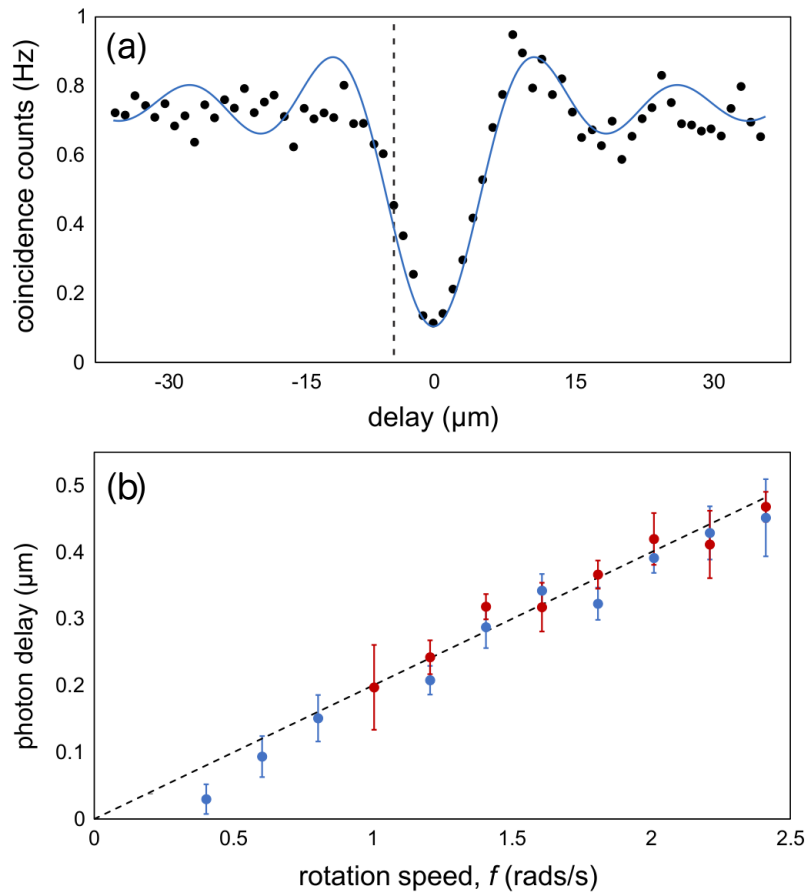


FIGURE 6.6: Results of the quantum experiment [122].(a) HOM interference dip measured by scanning the delay stage with no rotation of the experiment. The vertical dashed line marks the delay corresponding to the point of maximum steepness of the HOM dip. The shift can then be measured by fixing the stage at this delay and observing the changes in coincidence counts when the interferometer is in rotation. (b) Results showing measured HOM interference shift (circles) and fitted line (dashed). [105]

have to be taken in consideration. Moreover, in a recent paper [123], it has been shown that this precision can be greatly increased if instead of gauging the location of the dip by moving the delay stage, a movement of the DIP can simply be measured by observing changes in the coincidence counts as the interferometer is rotated. In particular, as can be seen from fig. 6.6(a), if the HOM interferometer is set at the maximum steepness of the dip (indicated by the dashed line), a shift of the dip due to changes in photon path will result in an increase (if the dip shifts right) or decrease (if the dip shifts left) of photons at the coincidence machine. Hence, a reference HOM dip

is obtained for each data set. This dip is consequently fit with an inverse Sinc function which is used as a maximum-likelihood estimator, allowing us to map the coincidence counts to photon path delay. It is important to note that the narrower the dip, the steeper the HOM curve hence the higher the precision that can be obtained using this method. In this system we therefore do not use any bandpass filters after the BBO crystal, hence generating a HOM dip of 0.02mm wide (as previously discussed in 5.6). This allows us to measure very small photon path delays down to 100 nm and smaller.

The results of the quantum experiment are therefore shown in figure 6.6(b), where the photon delays, as inferred from the changes in the coincidence counts, are shown at increasing rotation rates. In particular, figure 6.6(b) shows the values obtained on two different occasions (data points blue/red circles), where, between the runs, the system is reoptimized. This results in slightly different depths of the reference HOM dip but, more interestingly, a consistency in the results. It is also important to point out that each data point in the figure corresponds to the average and standard deviation of 50 measurement runs, hence demonstrating the repeatability of the experiment. Finally, the best fit to the data is calculated and is displayed in figure 6.6(b) as a dashed line. In particular, we found that the data is best described by a linear fit with slope $\Delta x_{\text{fit}} = 200 \pm 12 \text{ nm Hz}^{-1}$ where the error on the slope was simply calculated by finding the error band in which $\chi^2/N = 1$. These results clearly show that rotation can, for a fixed physical path length of the interferometer, modify the degree of distinguishability of two entangled photons and thus modify the quantum interference between the two photons. As such, this demonstrates a clear influence of non-inertial motion on non-classical photon states.

6.4 Classical counterpart to the Quantum Gyroscope

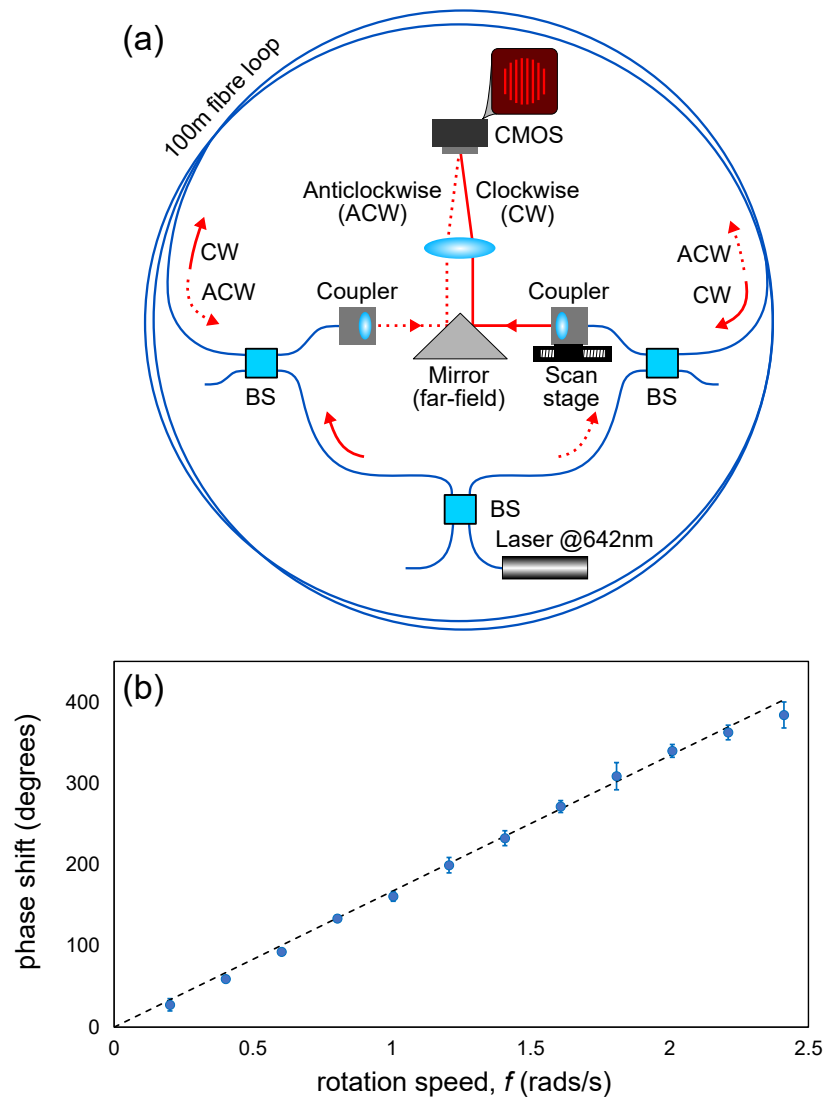


FIGURE 6.7: Classical experiment [122]. (a) The layout of the classical counterpart to the experiment. In particular, the detectors in the quantum experiment are replaced by a 642nm laser and the BBO crystal is replaced by a CMOS camera. (b) The results of the Sagnac phase measured by the system is displayed together with a fitted line that best fits the data.

Having shown a change in the bunching of the photons as a result of the presence of a rotation motion, a second experiment is carried out in which a purely classical measurement of the Sagnac effect is taken. This experiment holds two purposes: by

producing results in agreement with equation 6.3, it confirms that the set-up is indeed a gyroscope. It also sets an experimental benchmark on which we can calibrate the setup for the quantum measurements. Hence, in order to turn the HOM interference gyroscope previously described into its classical counterpart, two changes are carried out: the two SPADs are removed from the table and a 642 nm fibre coupled laser is connected to the HOM beam-splitter; and the BBO crystal is replaced with a CMOS camera (see fig. 6.7(a)). It is easy to see that, by making these simple changes, we have now created a classical system that retraces the path of its quantum counterpart and most importantly, it does so by keeping the configuration intact (i.e. all components between the generation of the light beams and the detection of the interference remain exactly the same as for the quantum experiment). In particular, the light generated by the coupled 642nm laser is split at the HOM beam splitter into clockwise and anticlockwise light beams, which after travelling through the system, recombine at a small angle at the CMOS camera. As the path length of the system is within the laser's coherence length, fringes will therefore appear on the CMOS camera. As demonstrated in the Sagnac equation (eq. 6.3), when the table is set to rotate at a constant speed, a shift of the fringes position can be seen. As for the quantum experiment, this shift can therefore be measured at different rotation speeds. The results of these measurements are shown in Fig. 6.7(b), where the averaged measured phase shifts $\Delta\phi$ together with their standard deviation over 50 measurement runs are plotted. Also, similarly to the quantum experiment, the shifts are obtained by performing the average (in absolute value) between a clockwise and an anticlockwise rotation measurement. Finally, the best fit to the data is calculated as in the quantum experiment and is displayed as a dashed line in Fig. 6.7(b). These results hence show that the best fit to the data is a line with slope $\Delta\phi_{\text{fit}} = 167 \pm 4 \text{ deg Hz}^{-1}$. This is then compared with the theoretical estimate based on the standard formula for the Sagnac effect, i.e. $\Delta\phi = 4\pi\Omega RL/(\lambda c) = 170 \text{ deg Hz}^{-1}$. As a good agreement exists between the theory and experimental result

we can therefore conclude that this experimental set-up is reliable in measuring the Sagnac effect.

6.5 Conclusion

We explicitly benchmark our experiment against a standard Sagnac (classical) interferometer in which phase interference is modified by rotation. However, the key point in our case is that it is the quantum interference of two photons that is modified by relativistic effects. As a result of this, we observe a clear change in the bunching of the photons as a result of purely mechanical rotation that is in agreement with our theory based on relativistic modifications to the standard HOM effect.

We can compare the quantum and the classical results, for example by taking the ratio of the slopes of the two fitted lines in Figs. 6.7(b) and 6.6(b): $\Delta x_{\text{fit}}/\Delta\phi_{\text{fit}} = 1.2 \pm 0.07 \text{ nm deg}^{-1}$. Path and phase differences in an interferometer are related by $\Delta x/\Delta\phi = \lambda/2\pi$. If we use the vacuum wavelength for the classical laser (642 nm), we find that $\Delta x_{\text{fit}}/\Delta\phi_{\text{fit}}$ and $\Delta x/\Delta\phi$ differ by a multiplicative factor of 1.478 ± 0.09 . Interestingly, this value is compatible with the refractive index $n \sim 1.45$ of the optical fibre used, as may intuitively be expected based on the fact that the classical measurement is sensitive to phase (and does not depend on the fibre index n [124]) whereas the quantum measurements rely on time delay hence it is not independent of photon drag (which does depend on n). In order to conclusively demonstrate that this is indeed related to the refractive index of the fibre, subsequent measurements would be required using different refractive index mediums. In one such experiment the current 100m long fibre could be replaced with a hollow core photonic-crystal fibre.

In conclusion, the experiment therefore implies that the quantum interference of two photons is affected by non-inertial motion, which opens new pathways to probe the relation between gravity and quantum mechanics.

Chapter 7

Conclusions and Future Work

Throughout this thesis, it has been shown how entangled photons can be used to advance a variety of fields: communication, computing and sensing being prime examples. Hence, in this thesis I have shown that two photon states, generated via SPDC can be integrated in a variety of experiments each exploiting a different characteristic of this quantum effect. As the SPDC effect was central to all the experiments, this thesis begins with an introduction to this process and in particular the use of a Type I phase matching nonlinear crystal in order to generate the entangled photon beams which were employed in the different experiments. In particular, both chapter 3 and chapter 4 utilise the spatial degree of freedom of SPDC generated entangled photons to enhance the quantity of information that can be transmitted in quantum communication systems. On the other hand, chapter 5 and chapter 6 rely on the ability of SPDC to generate indistinguishable photons.

As previously pointed out, quantum entanglement has been proposed to advance a variety of application fields, one such field being the field of quantum communication. In particular, as the spatial degree of freedom of light is theoretically unbounded, there has been a growing interest in using spatial modes to increase the information content in both quantum and classical communication systems. In chapter 3 I

therefore chose to compare the information capacity of two of the best known spatial modal sets, the LG set and the HG set, when transmitted in a finite-aperture system. Its important to note that all free space optical communication systems are aperture-limited, as they rely on the presence of finite sized optical elements for the transmitter and receiver (or in the case of our quantum system, two receiving apertures). In my experiment I was able to show, both through simulation and experimental data that the information capacity of the LG modes either equals or exceeds that of the HG modes for all aperture ratios, therefore making the LG modal set the optimal choice for an aperture limited system. This conclusion was solely based on the boundary conditions of the system where careful consideration was taken in making the circular aperture size of our detecting fibres the only limiting factor of the system. However, the advantage of the LG modal set could no longer be guaranteed if other source of loss are present in the system, an example being the loss caused by the modes' lateral displacement at the data receiver. In the future I therefore intend to extend this work to both incorporate all the major boundary conditions present in optical communication systems, and more sophisticated modal sets that are more suited to counteract the specific losses (the prolate spheroidal functions being a possible example [49]). This study will therefore have the ultimate goal of presenting a comprehensive study on the optimum choice of modal set depending on the boundary conditions of the experiment and the requirements of the free-space optical link.

Similarly to chapter 3, the goal of the experiment carried out in chapter 4 was also to enhance the quantity of information that can be transmitted in a quantum communication system. In chapter 4, this was achieved by presenting a new approach to imparting information on photons. In particular, our collaborators at the *National University of Singapore* designed a meta-fork grating capable of producing optical vortices carrying arbitrary rational values of OAM. By implementing this new grating in a quantum communication system, I was able to demonstrate the

feasibility of using this OAM generator for quantum communication systems. In particular, I demonstrated, both through simulation and experimental data, the ability of the proposed grating to generate a smooth spiral spectrum, thus demonstrating that the proposed vortex generator can be used to manipulate OAM modes at the single-photon regime. Furthermore, I was also able to demonstrate the ability of the proposed vortex generator to generate a smooth diagonal correlation matrix, with little to no crosstalk being exhibited by off diagonal elements, hence demonstrating the applicability of this method for quantum communications. It is important to point out that this is the first analog method proposed for the generation of OAM states and therefore possible applications for this mechanism are still to be fully explored.

While the experiments in chapters 3, and 4, rely on the spatial degree of freedom of entangled photons this is not the only property of entanglement that can be used for application purposes. In fact, both chapters 5, and 6 rely on the ability of SPDC to generate entangled photon pairs that are completely indistinguishable, therefore when made to interfere at a beam splitter, they will bunch together in what is known as a N00N state. These two-photon superposition states, also known as qubits, play an important role in quantum computing scheme as many types of quantum gates require the interaction of two or more qubits. But as discussed in chapter 5, being able to generate qubits is necessary but not sufficient for constructing quantum gates as equally important is the ability to deterministically control these photons. A process that has been shown to be able to deterministically absorb or transmit light at the single-photon regime is the recently discovered ‘Coherent Perfect Absorption’ process (CPA). In chapter 5 we therefore chose to build on this work and demonstrate that a thin multilayer graphene sample can be used to coherently absorb two-photon N00N states. In particular, we showed that by controlling the input phase of the N00N state at the graphene sample we were able to selectively control whether one photon or two-photon absorption occurs. It is important to emphasise that this was the first

experiment of its kind, as no previous experiment existed demonstrating the ability to coherently absorb quantum superposition states. As previously mentioned, the coherent control and absorption of qubits is essential for the generation of quantum gates. By demonstrating the ability of the CPA process to coherently control and absorb two-photon N00N states we therefore open the possibility of designing new quantum gates based on coherent perfect absorbers.

Finally, in chapter 6, the last experiment in my PhD is discussed. In contrast to all the previous experiments, the goal of this quantum test was not to advance an application field but rather to better understand quantum mechanics itself. More specifically, this experiment was proposed to test the role of relativity in quantum mechanics. This was done through the use of a “quantum gyroscope” composed of a HOM interferometer on a rotating table. In the experiment I was therefore able to measure a shift in position of the HOM dip as a function of the rotation speed of the table. This relative delay in the photons arrival is equivalent to the classical Sagnac effect with the sole difference being that while in the classical set-up the rotation motion induces a change in the interference of the two beams, in the quantum set-up the change is in the quantum interference of the two photons. This experiment therefore implies that the quantum interference of two entangled photons is effected by a uniform gravitational field. In the future I plan to extend this experiment in a more complicated reference frame. In particular I plan to use the non-uniform rotation to investigate the effect of time-dependent curvature on quantum entanglement.

Bibliography

- [1] Stephen Barnett. *Quantum Information*. Oxford University Press, Inc., New York, 2009.
- [2] Gilbert Grynberg, Alain Aspect, Claude Fabre, and Claude Cohen-Tannoudji. *Introduction to Quantum Optics: From the Semi-classical Approach to Quantized Light*. Cambridge University Press, 2010. doi: 10.1017/CBO9780511778261.
- [3] Erwin Schrödinger. Die gegenwärtige situation in der quantenmechanik. die naturwissenschaften 23, s. 807–812. *S.*, 823:844–849, 1935.
- [4] John S Bell. On the einstein podolsky rosen paradox. *Physics Physique Fizika*, 1(3):195, 1964.
- [5] John F. Clauser, Michael A. Horne, Abner Shimony, and Richard A. Holt. Proposed experiment to test local hidden-variable theories. *Phys. Rev. Lett.*, 23:880–884, Oct 1969. doi: 10.1103/PhysRevLett.23.880. URL <https://link.aps.org/doi/10.1103/PhysRevLett.23.880>.
- [6] Jun-Feng Tang, Zhibo Hou, Qi-Fan Xu, Guo-Yong Xiang, Chuan-Feng Li, and Guang-Can Guo. Polarization-independent coherent spatial-temporal interface with low loss. *Phys. Rev. Applied*, 12:064058, Dec 2019. doi: 10.1103/PhysRevApplied.12.064058. URL <https://link.aps.org/doi/10.1103/PhysRevApplied.12.064058>.

- [7] Han-Sen Zhong, Yuan Li, Wei Li, Li-Chao Peng, Zu-En Su, Yi Hu, Yu-Ming He, Xing Ding, Weijun Zhang, Hao Li, Lu Zhang, Zhen Wang, Lixing You, Xi-Lin Wang, Xiao Jiang, Li Li, Yu-Ao Chen, Nai-Le Liu, Chao-Yang Lu, and Jian-Wei Pan. 12-photon entanglement and scalable scattershot boson sampling with optimal entangled-photon pairs from parametric down-conversion. *Phys. Rev. Lett.*, 121:250505, Dec 2018. doi: 10.1103/PhysRevLett.121.250505. URL <https://link.aps.org/doi/10.1103/PhysRevLett.121.250505>.
- [8] Ashley Lyons, Thomas Roger, Niclas Westerberg, Stefano Vezzoli, Calum Maitland, Jonathan Leach, Miles J. Padgett, and Daniele Faccio. How fast is a twisted photon? *Optica*, 5(6):682–686, 6 2018. ISSN 2334-2536. doi: 10.1364/OPTICA.5.000682.
- [9] Frédéric Bouchard, Khabat Heshami, Duncan England, Robert Fickler, Robert W Boyd, Berthold-Georg Englert, Luis L Sánchez-Soto, and Ebrahim Karimi. Experimental investigation of quantum key distribution protocols with twisted photons. *arXiv preprint arXiv:1802.05773*, 2018.
- [10] Robert W. Boyd and Jonathan P. Dowling. Quantum lithography: status of the field. *Quantum Information Processing*, 11(4):891–901, Aug 2012. ISSN 1573-1332. doi: 10.1007/s11128-011-0253-y. URL <https://doi.org/10.1007/s11128-011-0253-y>.
- [11] D Giovannini, J Romero, J Leach, A Dudley, A Forbes, and MJ Padgett. High-dimensional mutually unbiased bases for quantum state tomography, quantum key distribution and other applications. In *Quantum Information and Measurement*, pages QTu2A–5. Optical Society of America, 2014.
- [12] Daniel Giovannini, Jacqueline Romero, Václav Potoček, Gergely Ferenczi, Fiona Speirits, Stephen M Barnett, Daniele Faccio, and Miles J Padgett. Spatially

- structured photons that travel in free space slower than the speed of light. *Science*, 347(6224):857–860, 2015.
- [13] Sun Kyung Lee, Tai Hyun Yoon, and Minhaeng Cho. Quantum optical measurements with undetected photons through vacuum field indistinguishability. *Scientific Reports*, 7(1):6558, 2017. doi: 10.1038/s41598-017-06800-0. URL <https://doi.org/10.1038/s41598-017-06800-0>.
- [14] Marco Genovese. Research on hidden variable theories: A review of recent progresses. *Physics Reports*, 413(6):319–396, 2005.
- [15] Thomas Roger, Sara Restuccia, Ashley Lyons, Daniel Giovannini, Jacqueline Romero, John Jeffers, Miles Padgett, and Daniele Faccio. Coherent absorption of n00n states. *Physical review letters*, 117(2):023601, 2016.
- [16] Government Office for Science. *The Quantum Age: technological opportunities*. OGL, 2016.
- [17] Matthias Fink, Ana Rodriguez-Aramendia, Johannes Handsteiner, Abdul Ziarkash, Fabian Steinlechner, Thomas Scheidl, Ivette Fuentes, Jacques Pienaar, Timothy C. Ralph, and Rupert Ursin. Experimental test of photonic entanglement in accelerated reference frames. *Nature Communications*, 8:15304 EP –, 05 2017. URL <https://doi.org/10.1038/ncomms15304>.
- [18] Sara Restuccia, Daniel Giovannini, Graham Gibson, and Miles Padgett. Comparing the information capacity of laguerre-gaussian and hermite-gaussian modal sets in a finite-aperture system. *Opt. Express*, 24(24):27127–27136, Nov 2016. doi: 10.1364/OE.24.027127. URL <http://www.opticsexpress.org/abstract.cfm?URI=oe-24-24-27127>.
- [19] Kun Huang, Hong Liu, Sara Restuccia, Muhammad Q Mehmood, Sheng-Tao Mei, Daniel Giovannini, Aaron Danner, Miles J Padgett, Jing-Hua Teng, and

- Cheng-Wei Qiu. Spiniform phase-encoded metagratings entangling arbitrary rational-order orbital angular momentum. *Light: Science & Applications*, 7:17156 EP –, 03 2018. URL <https://doi.org/10.1038/lsa.2017.156>.
- [20] Zhe-Yu Jeff Ou. *Multi-photon quantum interference*, volume 43. Springer, 2007.
- [21] J. A. Giordmaine and Robert C. Miller. Tunable coherent parametric oscillation in linbo_3 at optical frequencies. *Phys. Rev. Lett.*, 14:973–976, Jun 1965. doi: 10.1103/PhysRevLett.14.973. URL <https://link.aps.org/doi/10.1103/PhysRevLett.14.973>.
- [22] R. W. Boyd and D. Prato. *Nonlinear Optics*. Elsevier Science, 2008. ISBN 9780080485966.
- [23] Ashley Lyons et al. *Two photon quantum metrology*. PhD thesis, Heriot-Watt University, 2017.
- [24] FM Miatto, D Giovannini, J Romero, S Franke-Arnold, SM Barnett, and MJ Padgett. Bounds and optimisation of orbital angular momentum bandwidths within parametric down-conversion systems. *The European Physical Journal D*, 66(7):178, 2012.
- [25] Gintaras Tamošauskas, Gvidas Beresnevičius, Darius Gadonas, and Audrius Dubietis. Transmittance and phase matching of bbo crystal in the $3\text{--}5\ \mu\text{m}$ range and its application for the characterization of mid-infrared laser pulses. *Opt. Mater. Express*, 8(6):1410–1418, Jun 2018. doi: 10.1364/OME.8.001410. URL <http://www.osapublishing.org/ome/abstract.cfm?URI=ome-8-6-1410>.
- [26] J. Leach, B. Jack, J. Romero, M. Ritsch-Marte, R.W. Boyd, A.K. Jha, S.M. Barnett, S. Franke-Arnold, and M. J. Padgett. Violation of a bell inequality in two-dimensional orbital angular momentum state-spaces. *Opt. Express*, 17

- (10):8287–8293, May 2009. doi: 10.1364/OE.17.008287. URL <http://www.opticsexpress.org/abstract.cfm?URI=oe-17-10-8287>.
- [27] Jonathan Leach, Barry Jack, Jacqui Romero, Anand K Jha, Alison M Yao, Sonja Franke-Arnold, David G Ireland, Robert W Boyd, Stephen M Barnett, and Miles J Padgett. Quantum correlations in optical angle–orbital angular momentum variables. *Science*, 329(5992):662–665, 2010.
- [28] D Giovannini, J Romero, and M J Padgett. Interference of probability amplitudes: a simple demonstration within the hong–ou–mandel experiment. *Journal of Optics*, 16(3):032002, mar 2014. doi: 10.1088/2040-8978/16/3/032002. URL <https://doi.org/10.1088%2F2040-8978%2F16%2F3%2F032002>.
- [29] Christophe Couteau. Spontaneous parametric down-conversion. *Contemporary Physics*, 59(3):291–304, 2018.
- [30] Chung K. Hong, Stephen R. Friberg, and Leonard Mandel. Optical communication channel based on coincident photon pairs. *Appl. Opt.*, 24(22):3877–3882, Nov 1985. doi: 10.1364/AO.24.003877. URL <http://ao.osa.org/abstract.cfm?URI=ao-24-22-3877>.
- [31] David C. Burnham and Donald L. Weinberg. Observation of simultaneity in parametric production of optical photon pairs. *Phys. Rev. Lett.*, 25:84–87, Jul 1970. doi: 10.1103/PhysRevLett.25.84. URL <https://link.aps.org/doi/10.1103/PhysRevLett.25.84>.
- [32] Yong Meng Sua, Heng Fan, Amin Shahverdi, Jia-Yang Chen, and Yu-Ping Huang. Direct generation and detection of quantum correlated photons with 3.2 um wavelength spacing. *Sci Rep*, 7(1):17494, Dec 2017. ISSN 2045-2322 (Electronic); 2045-2322 (Linking). doi: 10.1038/s41598-017-17820-1.

- [33] Kai Guo, Erik N Christensen, Jesper B Christensen, Jacob G Koefoed, Davide Bacco, Yunhong Ding, Haiyan Ou, and Karsten Rottwitt. High coincidence-to-accidental ratio continuous-wave photon-pair generation in a grating-coupled silicon strip waveguide. *Applied Physics Express*, 10(6):062801, 2017.
- [34] D N Klyshko. A simple method of preparing pure states of an optical field, of implementing the einstein–podolsky–rosen experiment, and of demonstrating the complementarity principle. *Soviet Physics Uspekhi*, 31(1):74–85, jan 1988. doi: 10.1070/pu1988v031n01abeh002537. URL <https://doi.org/10.1070/2Fpu1988v031n01abeh002537>.
- [35] Reuben S Aspden, Daniel S Tasca, Andrew Forbes, Robert W Boyd, and Miles J Padgett. Experimental demonstration of klyshko’s advanced-wave picture using a coincidence-count based, camera-enabled imaging system. *Journal of Modern Optics*, 61(7):547–551, 2014.
- [36] C. E. Shannon. A mathematical theory of communication. *Bell Syst. Tech. J.*, 27:379–423, 1948.
- [37] Guifang Li and Xiang Liu. Focus issue: Space multiplexed optical transmission. *Opt. Express*, 19(17):16574–16575, Aug 2011. doi: 10.1364/OE.19.016574. URL <http://www.opticsexpress.org/abstract.cfm?URI=oe-19-17-16574>.
- [38] D. J. Richardson, J. M. Fini, and L. E. Nelson. Space-division multiplexing in optical fibres. *Nature Photonics*, 7(5):354–362, Apr 2013. ISSN 1749-4893. doi: 10.1038/nphoton.2013.94. URL <http://dx.doi.org/10.1038/NPHOTON.2013.94>.
- [39] Mohammad Mirhosseini, Omar S Magaña-Loaiza, Malcolm N O’Sullivan, Brandon Rodenburg, Mehul Malik, Martin PJ Lavery, Miles J Padgett, Daniel J Gauthier, and Robert W Boyd. High-dimensional quantum cryptography with twisted light. *New Journal of Physics*, 17(3):033033, 2015.

- [40] A. E. Willner, H. Huang, Y. Yan, Y. Ren, N. Ahmed, G. Xie, C. Bao, L. Li, Y. Cao, Z. Zhao, J. Wang, M. P. J. Lavery, M. Tur, S. Ramachandran, A. F. Molisch, N. Ashrafi, and S. Ashrafi. Optical communications using orbital angular momentum beams. *Adv. Opt. Photon.*, 7(1):66–106, Mar 2015. doi: 10.1364/AOP.7.000066. URL <http://aop.osa.org/abstract.cfm?URI=aop-7-1-66>.
- [41] Mario Krenn, Robert Fickler, Matthias Fink, Johannes Handsteiner, Mehul Malik, Thomas Scheidl, Rupert Ursin, and Anton Zeilinger. Communication with spatially modulated light through turbulent air across vienna. *New Journal of Physics*, 16(11):113028, 2014.
- [42] Alan E Willner, Jian Wang, and Hao Huang. A different angle on light communications. *Science*, 337(6095):655–656, 2012.
- [43] B. Zhu, T.F. Taunay, M. Fishteyn, X. Liu, S. Chandrasekhar, M. F. Yan, J. M. Fini, E. M. Monberg, and F. V. Dimarcello. 112-tb/s space-division multiplexed dwdm transmission with 14-b/s/hz aggregate spectral efficiency over a 76.8-km seven-core fiber. *Opt. Express*, 19(17):16665–16671, Aug 2011. doi: 10.1364/OE.19.016665. URL <http://www.opticsexpress.org/abstract.cfm?URI=oe-19-17-16665>.
- [44] Nenad Bozinovic, Yang Yue, Yongxiong Ren, Moshe Tur, Poul Kristensen, Hao Huang, Alan E Willner, and Siddharth Ramachandran. Terabit-scale orbital angular momentum mode division multiplexing in fibers. *science*, 340(6140):1545–1548, 2013.
- [45] Hao Huang, Guodong Xie, Yan Yan, Nisar Ahmed, Yongxiong Ren, Yang Yue, Dvora Rogawski, Moshe J. Willner, Baris I. Erkmen, Kevin M. Birnbaum, Samuel J. Dolinar, Martin P. J. Lavery, Miles J. Padgett, Moshe Tur, and Alan E. Willner. 100-tbit/s free-space data link enabled by three-dimensional multiplexing of orbital angular momentum, polarization, and

- wavelength. *Opt. Lett.*, 39(2):197–200, Jan 2014. doi: 10.1364/OL.39.000197.
URL <http://ol.osa.org/abstract.cfm?URI=ol-39-2-197>.
- [46] Andrew Forbes and Isaac Nape. Quantum mechanics with patterns of light: Progress in high dimensional and multidimensional entanglement with structured light. *AVS Quantum Science*, 1(1):011701, 2019.
- [47] C. H. Bennett and G. Brassard. Quantum cryptography: public key distribution and coin tossing. In *Proceedings of IEEE International Conference on Computers Systems and Signal Processing*, volume 175, 1984.
- [48] M Avesani, L Calderaro, M Schiavon, A Stanco, C Agnesi, A Santamato, M Zahidy, A Scriminich, G Foletto, G Contestabile, et al. Full daylight quantum-key-distribution at 1550 nm enabled by integrated silicon photonics. *arXiv preprint arXiv:1907.10039*, 2019.
- [49] Brandon Rodenburg. *Communicating with transverse modes of light*. University of Rochester, 2015.
- [50] Nicolas J Cerf, Mohamed Bourennane, Anders Karlsson, and Nicolas Gisin. Security of quantum key distribution using d-level systems. *Physical Review Letters*, 88(12):127902, 2002.
- [51] Juan Yin, Yuan Cao, Yu-Huai Li, Sheng-Kai Liao, Liang Zhang, Ji-Gang Ren, Wen-Qi Cai, Wei-Yue Liu, Bo Li, Hui Dai, et al. Satellite-based entanglement distribution over 1200 kilometers. *Science*, 356(6343):1140–1144, 2017.
- [52] Kai Pang, Haoqian Song, Zhe Zhao, Runzhou Zhang, Hao Song, Guodong Xie, Long Li, Cong Liu, Jing Du, Andreas F Molisch, et al. 400-gbit/s qpsk free-space optical communication link based on four-fold multiplexing of hermite-gaussian or laguerre-gaussian modes by varying both modal indices. *Optics letters*, 43(16):3889–3892, 2018.

- [53] Jian Wang, Jeng-Yuan Yang, Irfan M Fazal, Nisar Ahmed, Yan Yan, Hao Huang, Yongxiong Ren, Yang Yue, Samuel Dolinar, Moshe Tur, et al. Terabit free-space data transmission employing orbital angular momentum multiplexing. *Nature photonics*, 6(7):488, 2012.
- [54] Martin PJ Lavery, Christian Peuntinger, Kevin Günthner, Peter Banzer, Dominique Elser, Robert W Boyd, Miles J Padgett, Christoph Marquardt, and Gerd Leuchs. Free-space propagation of high-dimensional structured optical fields in an urban environment. *Science Advances*, 3(10):e1700552, 2017.
- [55] E. Ciaramella, Y. Arimoto, G. Contestabile, M. Presi, A. D’Errico, V. Guarino, and M. Matsumoto. 1.28-tb/s (32×40 gb/s) free-space optical wdm transmission system. *IEEE Photonics Technology Letters*, 21(16):1121–1123, 8 2009. ISSN 1041-1135. doi: 10.1109/LPT.2009.2021149.
- [56] Heinz Willebrand and Baksheesh S Ghuman. *Free space optics: enabling optical connectivity in today’s networks*. SAMS publishing, 2002.
- [57] Les Allen, Marco W Beijersbergen, RJC Spreeuw, and JP Woerdman. Orbital angular momentum of light and the transformation of laguerre-gaussian laser modes. *Physical Review A*, 45(11):8185, 1992.
- [58] Alison M Yao and Miles J Padgett. Orbital angular momentum: origins, behavior and applications. *Advances in Optics and Photonics*, 3(2):161–204, 2011.
- [59] Manuel Erhard, Robert Fickler, Mario Krenn, and Anton Zeilinger. Twisted photons: new quantum perspectives in high dimensions. *Light: Science & Applications*, 7(3):17146, 2018.
- [60] Jennifer E Curtis, Brian A Koss, and David G Grier. Dynamic holographic optical tweezers. *Optics communications*, 207(1-6):169–175, 2002.

- [61] Graham Gibson, Johannes Courtial, Miles J Padgett, Mikhail Vasnetsov, Valeriy Pas'ko, Stephen M Barnett, and Sonja Franke-Arnold. Free-space information transfer using light beams carrying orbital angular momentum. *Optics express*, 12(22):5448–5456, 2004.
- [62] Mauritz Andersson, Eilert Berglind, and Gunnar Björk. Orbital angular momentum modes do not increase the channel capacity in communication links. *New Journal of Physics*, 17(4):043040, 2015.
- [63] Ningbo Zhao, Xiaoying Li, Guifang Li, and Joseph M Kahn. Capacity limits of spatially multiplexed free-space communication. *Nature photonics*, 9(12):822, 2015.
- [64] Boulat A Bash, Nivedita Chandrasekaran, Jeffrey H Shapiro, and Saikat Guha. Quantum key distribution using multiple gaussian focused beams. *arXiv preprint arXiv:1604.08582*, 2016.
- [65] Robert W Boyd, Brandon Rodenburg, Mohammad Mirhosseini, and Stephen M Barnett. Influence of atmospheric turbulence on the propagation of quantum states of light using plane-wave encoding. *Optics express*, 19(19):18310–18317, 2011.
- [66] Guoxuan Zhu, Yuanhui Wen, Xiong Wu, Yujie Chen, Jie Liu, and Siyuan Yu. Obstacle evasion in free-space optical communications utilizing airy beams. *Opt. Lett.*, 43(6):1203–1206, Mar 2018. doi: 10.1364/OL.43.001203. URL <http://ol.osa.org/abstract.cfm?URI=ol-43-6-1203>.
- [67] Ronald L. Phillips and Larry C. Andrews. Spot size and divergence for laguerre gaussian beams of any order. *Appl. Opt.*, 22(5):643–644, Mar 1983. doi: 10.1364/AO.22.000643. URL <http://ao.osa.org/abstract.cfm?URI=ao-22-5-643>.

- [68] Johannes Courtial and MJ Padgett. Performance of a cylindrical lens mode converter for producing laguerre–gaussian laser modes. *Optics communications*, 159(1-3):13–18, 1999.
- [69] M.W. Beijersbergen, L. Allen, H.E.L.O. van der Veen, and J.P. Woerdman. Astigmatic laser mode converters and transfer of orbital angular momentum. *Optics Communications*, 96(1):123 – 132, 1993. ISSN 0030-4018. doi: [https://doi.org/10.1016/0030-4018\(93\)90535-D](https://doi.org/10.1016/0030-4018(93)90535-D). URL <http://www.sciencedirect.com/science/article/pii/003040189390535D>.
- [70] Alois Mair, Alipasha Vaziri, Gregor Weihs, and Anton Zeilinger. Entanglement of the orbital angular momentum states of photons. *Nature*, 412:313 EP –, 07 2001. URL <https://doi.org/10.1038/35085529>.
- [71] SSR Oemrawsingh, X Ma, D Voigt, A Aiello, E.R. Eliel, and JP Woerdman. Experimental demonstration of fractional orbital angular momentum entanglement of two photons. *Physical review letters*, 95(24):240501, 2005.
- [72] Melanie McLaren, Megan Agnew, Jonathan Leach, Filippus S. Roux, Miles J. Padgett, Robert W. Boyd, and Andrew Forbes. Entangled bessel-gaussian beams. *Opt. Express*, 20(21):23589–23597, Oct 2012. doi: 10.1364/OE.20.023589. URL <http://www.opticsexpress.org/abstract.cfm?URI=oe-20-21-23589>.
- [73] Robert Fickler, Radek Lapkiewicz, William N Plick, Mario Krenn, Christoph Schaeff, Sven Ramelow, and Anton Zeilinger. Quantum entanglement of high angular momenta. *Science*, 338(6107):640–643, 2012.
- [74] Naoya Matsumoto, Taro Ando, Takashi Inoue, Yoshiyuki Ohtake, Norihiro Fukuchi, and Tsutomu Hara. Generation of high-quality higher-order laguerre-gaussian beams using liquid-crystal-on-silicon spatial light modulators. *J. Opt.*

- Soc. Am. A*, 25(7):1642–1651, Jul 2008. doi: 10.1364/JOSAA.25.001642. URL <http://josaa.osa.org/abstract.cfm?URI=josaa-25-7-1642>.
- [75] Bienvenu Ndagano, Nokwazi Mphuthi, Giovanni Milione, and Andrew Forbes. Comparing mode-crosstalk and mode-dependent loss of laterally displaced orbital angular momentum and hermite–gaussian modes for free-space optical communication. *Opt. Lett.*, 42(20):4175–4178, Oct 2017. doi: 10.1364/OL.42.004175. URL <http://ol.osa.org/abstract.cfm?URI=ol-42-20-4175>.
- [76] J. H. Poynting. The wave motion of a revolving shaft, and a suggestion as to the angular momentum in a beam of circularly polarised light. *Proceedings of the Royal Society of London A: Mathematical, Physical and Engineering Sciences*, 82(557):560–567, 1909. ISSN 0950-1207. doi: 10.1098/rspa.1909.0060. URL <http://rspa.royalsocietypublishing.org/content/82/557/560>.
- [77] Richard A. Beth. Mechanical detection and measurement of the angular momentum of light. *Phys. Rev.*, 50:115–125, Jul 1936. doi: 10.1103/PhysRev.50.115. URL <https://link.aps.org/doi/10.1103/PhysRev.50.115>.
- [78] C. G. Darwin. Notes on the theory of radiation. *Proceedings of the Royal Society of London A: Mathematical, Physical and Engineering Sciences*, 136(829):36–52, 1932. ISSN 0950-1207. doi: 10.1098/rspa.1932.0065. URL <http://rspa.royalsocietypublishing.org/content/136/829/36>.
- [79] P. Couillet, L. Gil, and F. Rocca. Optical vortices. *Optics Communications*, 73(5):403 – 408, 1989. ISSN 0030-4018. doi: [https://doi.org/10.1016/0030-4018\(89\)90180-6](https://doi.org/10.1016/0030-4018(89)90180-6). URL <http://www.sciencedirect.com/science/article/pii/0030401889901806>.
- [80] Miles J. Padgett. Orbital angular momentum 25 years on [invited]. *Opt. Express*, 25(10):11265–11274, May 2017. doi: 10.1364/OE.25.011265. URL <http://www.opticsexpress.org/abstract.cfm?URI=oe-25-10-11265>.

- [81] Mario Krenn, Johannes Handsteiner, Matthias Fink, Robert Fickler, Rupert Ursin, Mehul Malik, and Anton Zeilinger. Twisted light transmission over 143 km. *Proceedings of the National Academy of Sciences*, 113(48):13648–13653, 2016. ISSN 0027-8424. doi: 10.1073/pnas.1612023113. URL <http://www.pnas.org/content/113/48/13648>.
- [82] Xuewen Wang, Zhongquan Nie, Liang Yao, Jian Wang, Tao Li, and Baohua Jia. Recent advances on optical vortex generation. *Nanophotonics*, 7:1533, 2018-11-20T11:19:13.756+01:00 2018. doi: 10.1515/nanoph-2018-0072. URL <https://www.degruyter.com/view/j/nanoph.2018.7.issue-9/nanoph-2018-0072/nanoph-2018-0072.xml>.
- [83] John Frederick Nye and Michael Victor Berry. Dislocations in wave trains. *Proc. R. Soc. Lond. A*, 336(1605):165–190, 1974.
- [84] M.W. Beijersbergen, R.P.C. Coerwinkel, M. Kristensen, and J.P. Woerdman. Helical-wavefront laser beams produced with a spiral phaseplate. *Optics Communications*, 112(5):321 – 327, 1994. ISSN 0030-4018. doi: [https://doi.org/10.1016/0030-4018\(94\)90638-6](https://doi.org/10.1016/0030-4018(94)90638-6). URL <http://www.sciencedirect.com/science/article/pii/0030401894906386>.
- [85] V. Bazhenov, M. V. Vasnetsov, and M. S. Soskin. Laser-beams with screw dislocations in their wave-fronts. *JETP. Lett.*, 52:429–431, 1990.
- [86] A. Jesacher, A. Schwaighofer, S. Fürhapter, C. Maurer, S. Bernet, and M. Ritsch-Marte. Wavefront correction of spatial light modulators using an optical vortex image. *Opt. Express*, 15(9):5801–5808, Apr 2007. doi: 10.1364/OE.15.005801. URL <http://www.opticsexpress.org/abstract.cfm?URI=oe-15-9-5801>.
- [87] Thomas W. Clark, Rachel F. Offer, Sonja Franke-Arnold, Aidan S. Arnold, and Neal Radwell. Comparison of beam generation techniques using a phase only

- spatial light modulator. *Opt. Express*, 24(6):6249–6264, Mar 2016. doi: 10.1364/OE.24.006249. URL <http://www.opticsexpress.org/abstract.cfm?URI=oe-24-6-6249>.
- [88] Neal Radwell, Rachel F Offer, Adam Selyem, and Sonja Franke-Arnold. Optimisation of arbitrary light beam generation with spatial light modulators. *Journal of Optics*, 19(9):095605, 2017.
- [89] MV Berry. Optical vortices evolving from helicoidal integer and fractional phase steps. *Journal of Optics A: Pure and Applied Optics*, 6(2):259, 2004.
- [90] Jonathan Leach, Eric Yao, and Miles J Padgett. Observation of the vortex structure of a non-integer vortex beam. *New Journal of Physics*, 6(1):71, 2004.
- [91] Alipasha Vaziri, Jian-Wei Pan, Thomas Jennewein, Gregor Weihs, and Anton Zeilinger. Concentration of higher dimensional entanglement: Qutrits of photon orbital angular momentum. *Phys. Rev. Lett.*, 91:227902, Nov 2003. doi: 10.1103/PhysRevLett.91.227902. URL <https://link.aps.org/doi/10.1103/PhysRevLett.91.227902>.
- [92] Ebrahim Karimi, Daniel Giovannini, Eliot Bolduc, Nicolas Bent, Filippo M Miatto, Miles J Padgett, and Robert W Boyd. Exploring the quantum nature of the radial degree of freedom of a photon via hong-ou-mandel interference. *PHYSICAL REVIEW A Phys Rev A*, 89:013829, 2014.
- [93] Peter C. Humphreys, Benjamin J. Metcalf, Justin B. Spring, Merritt Moore, Xian-Min Jin, Marco Barbieri, W. Steven Kolthammer, and Ian A. Walmsley. Linear optical quantum computing in a single spatial mode. *Phys. Rev. Lett.*, 111:150501, Oct 2013. doi: 10.1103/PhysRevLett.111.150501. URL <https://link.aps.org/doi/10.1103/PhysRevLett.111.150501>.

- [94] Hwang Lee, Pieter Kok, Colin P Williams, and Jonathan P Dowling. From linear optical quantum computing to heisenberg-limited interferometry. *Journal of Optics B: Quantum and Semiclassical Optics*, 6(8):S796, 2004.
- [95] Agedi N. Boto, Pieter Kok, Daniel S. Abrams, Samuel L. Braunstein, Colin P. Williams, and Jonathan P. Dowling. Quantum interferometric optical lithography: Exploiting entanglement to beat the diffraction limit. *Phys. Rev. Lett.*, 85:2733–2736, Sep 2000. doi: 10.1103/PhysRevLett.85.2733. URL <https://link.aps.org/doi/10.1103/PhysRevLett.85.2733>.
- [96] Keiichi Edamatsu, Ryosuke Shimizu, and Tadashi Itoh. Measurement of the photonic de broglie wavelength of entangled photon pairs generated by spontaneous parametric down-conversion. *Phys. Rev. Lett.*, 89:213601, Nov 2002. doi: 10.1103/PhysRevLett.89.213601. URL <https://link.aps.org/doi/10.1103/PhysRevLett.89.213601>.
- [97] Pieter Kok, Hwang Lee, and Jonathan P Dowling. Creation of large-photon-number path entanglement conditioned on photodetection. *Physical Review A*, 65(5):052104, 2002.
- [98] Pieter Kok, W. J. Munro, Kae Nemoto, T. C. Ralph, Jonathan P. Dowling, and G. J. Milburn. Linear optical quantum computing with photonic qubits. *Rev. Mod. Phys.*, 79:135–174, Jan 2007. doi: 10.1103/RevModPhys.79.135. URL <https://link.aps.org/doi/10.1103/RevModPhys.79.135>.
- [99] YD Chong, Li Ge, Hui Cao, and A Douglas Stone. Coherent perfect absorbers: time-reversed lasers. *Physical review letters*, 105(5):053901, 2010.
- [100] Wenjie Wan, Yidong Chong, Li Ge, Heeso Noh, A Douglas Stone, and Hui Cao. Time-reversed lasing and interferometric control of absorption. *Science*, 331(6019):889–892, 2011.

- [101] Mingbo Pu, Qin Feng, Min Wang, Chenggang Hu, Cheng Huang, Xiaoliang Ma, Zeyu Zhao, Changtao Wang, and Xiangang Luo. Ultrathin broadband nearly perfect absorber with symmetrical coherent illumination. *Opt. Express*, 20(3):2246–2254, Jan 2012. doi: 10.1364/OE.20.002246. URL <http://www.opticsexpress.org/abstract.cfm?URI=oe-20-3-2246>.
- [102] Sukosin Thongrattanasiri, Frank H. L. Koppens, and F. Javier García de Abajo. Complete optical absorption in periodically patterned graphene. *Phys. Rev. Lett.*, 108:047401, Jan 2012. doi: 10.1103/PhysRevLett.108.047401. URL <https://link.aps.org/doi/10.1103/PhysRevLett.108.047401>.
- [103] Shraddha M. Rao, Julius J. F. Heitz, Thomas Roger, Niclas Westerberg, and Daniele Faccio. Coherent control of light interaction with graphene. *Opt. Lett.*, 39(18):5345–5347, Sep 2014. doi: 10.1364/OL.39.005345. URL <http://ol.osa.org/abstract.cfm?URI=ol-39-18-5345>.
- [104] Thomas Roger, Stefano Vezzoli, Eliot Bolduc, Joao Valente, Julius J F Heitz, John Jeffers, Cesare Soci, Jonathan Leach, Christophe Couteau, Nikolay I Zheludev, and Daniele Faccio. Coherent perfect absorption in deeply subwavelength films in the single-photon regime. *Nat Commun*, 6:7031, 2015. ISSN 2041-1723 (Electronic); 2041-1723 (Linking). doi: 10.1038/ncomms8031.
- [105] C. K. Hong, Z. Y. Ou, and L. Mandel. Measurement of subpicosecond time intervals between two photons by interference. *Phys. Rev. Lett.*, 59:2044–2046, Nov 1987. doi: 10.1103/PhysRevLett.59.2044. URL <https://link.aps.org/doi/10.1103/PhysRevLett.59.2044>.
- [106] YH Shih and Carroll O Alley. New type of einstein-podolsky-rosen-bohm experiment using pairs of light quanta produced by optical parametric down conversion. *Physical Review Letters*, 61(26):2921, 1988.

- [107] John Jeffers. Interference and the lossless lossy beam splitter. *Journal of Modern Optics*, 47(11):1819–1824, 2000.
- [108] Stephen M. Barnett, John Jeffers, Alessandra Gatti, and Rodney Loudon. Quantum optics of lossy beam splitters. *Phys. Rev. A*, 57:2134–2145, Mar 1998. doi: 10.1103/PhysRevA.57.2134. URL <https://link.aps.org/doi/10.1103/PhysRevA.57.2134>.
- [109] W. M. Macek and D. T. M. Davis. Rotation rate sensing with traveling-wave ring lasers. *Applied Physics Letters*, 2(3):67–68, 1963. doi: 10.1063/1.1753778. URL <https://doi.org/10.1063/1.1753778>.
- [110] Sabina Merlo, Michele Norgia, and Silvano Donati. Fiber gyroscope principles. *Handbook of Fibre Optic Sensing Technology*, pages 1–23, 2000.
- [111] V. Vali and R. W. Shorthill. Fiber ring interferometer. *Appl. Opt.*, 15(5): 1099–1100, May 1976. doi: 10.1364/AO.15.001099. URL <http://ao.osa.org/abstract.cfm?URI=ao-15-5-1099>.
- [112] Kjell Kråkenes and Kjell Bløtekjaer. Sagnac interferometer for underwater sound detection: noise properties. *Opt. Lett.*, 14(20):1152–1154, Oct 1989. doi: 10.1364/OL.14.001152. URL <http://ol.osa.org/abstract.cfm?URI=ol-14-20-1152>.
- [113] Y. Zhao, D. Wu, R. Lv, and J. Li. Magnetic field measurement based on the sagnac interferometer with a ferrofluid-filled high-birefringence photonic crystal fiber. *IEEE Transactions on Instrumentation and Measurement*, 65(6):1503–1507, June 2016. ISSN 0018-9456. doi: 10.1109/TIM.2016.2519767.
- [114] Ke-Xun Sun, M M. Fejer, Eric Gustafson, and Robert Byer. Sagnac interferometer for gravitational-wave detection. *Physical review letters*, 76:3053–3056, 05 1996. doi: 10.1103/PhysRevLett.76.3053.

- [115] Vittorio M N Passaro, Antonello Cuccovillo, Lorenzo Vaiani, Martino De Carlo, and Carlo Edoardo Campanella. Gyroscope technology and applications: A review in the industrial perspective. *Sensors (Basel)*, 17(10), Oct 2017. ISSN 1424-8220 (Electronic); 1424-8220 (Linking). doi: 10.3390/s17102284.
- [116] RB Hurst, GE Stedman, KU Schreiber, RJ Thirkettle, RD Graham, N Rabeendran, and J-PR Wells. Experiments with an 834 m 2 ring laser interferometer. *Journal of Applied Physics*, 105(11):113115, 2009.
- [117] Ram Yahalom, Behzad Moslehi, Levy Oblea, Vahid Sotoudeh, and JC Ha. Low-cost, compact fiber-optic gyroscope for super-stable line-of-sight stabilization. In *IEEE/ION Position, Location and Navigation Symposium*, pages 180–186. IEEE, 2010.
- [118] Shailesh Srivastava, Shreesha Rao D S, and Hari Nandakumar. Novel optical gyroscope: proof of principle demonstration and future scope. *Sci Rep*, 6: 34634, 2016. ISSN 2045-2322 (Electronic); 2045-2322 (Linking). doi: 10.1038/srep34634.
- [119] Richard Howl, Roger Penrose, and Ivette Fuentes. Exploring the unification of quantum theory and general relativity with a bose–einstein condensate. *New Journal of Physics*, 21(4):043047, 2019.
- [120] J. B. Fixler, G. T. Foster, J. M. McGuirk, and M. A. Kasevich. Atom interferometer measurement of the newtonian constant of gravity. *Science*, 315 (5808):74–77, 2007. ISSN 0036-8075. doi: 10.1126/science.1135459. URL <https://science.sciencemag.org/content/315/5808/74>.
- [121] B Culshaw and I P Giles. Fibre optic gyroscopes. *Journal of Physics E: Scientific Instruments*, 16(1):5–15, jan 1983. doi: 10.1088/0022-3735/16/1/001. URL <https://doi.org/10.1088%2F0022-3735%2F16%2F1%2F001>.

-
- [122] Sara Restuccia, Marko Toroš, Graham M Gibson, Hendrik Ulbricht, Daniele Faccio, and Miles J Padgett. Photon bunching in a rotating reference frame. *Physical Review Letters*, 123(11):110401, 2019.
- [123] Ashley Lyons, George C Knee, Eliot Bolduc, Thomas Roger, Jonathan Leach, Erik M Gauger, and Daniele Faccio. Attosecond-resolution hong-ou-mandel interferometry. *Science advances*, 4(5):eaap9416, 2018.
- [124] Evert Jan Post. Sagnac effect. *Reviews of Modern Physics*, 39(2):475, 1967.